UiO : Department of Mathematics
University of Oslo

Numerical Investigation of Turbulent Flow in Helically Coiled Pipes

Flow Instability in the Internal Carotid Artery

Kei Yamamoto

Master's Thesis, Spring 2022

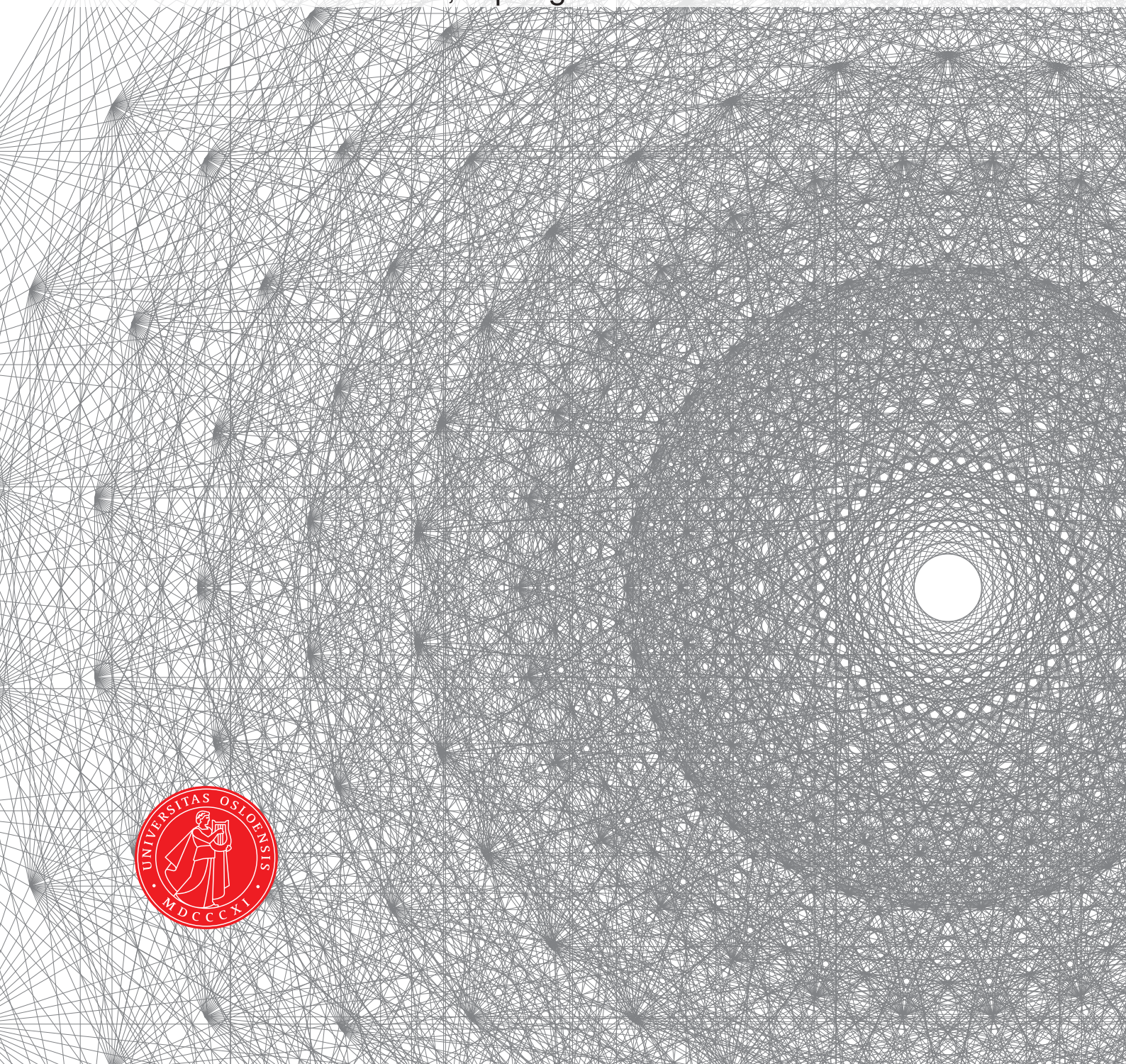

This master's thesis is submitted under the master's programme *Fluid Mechanics*, with programme option *Biomechanics and medical mechanics*, at the Department of Mathematics, University of Oslo. The scope of the thesis is 60 credits.

The front page depicts a section of the root system of the exceptional Lie group E_8, projected into the plane. Lie groups were invented by the Norwegian mathematician Sophus Lie (1842–1899) to express symmetries in differential equations and today they play a central role in various parts of mathematics.

Abstract

Fluid flow in helically coiled pipes is not fully understood. Although many efforts have been devoted to investigating the complex characteristics of the flow in helically coiled pipes, much is unknown for especially high Reynolds numbers, i.e., turbulence.

In this thesis, turbulent flow in helically coiled pipes is numerically investigated. First, direct numerical simulation of turbulent flow in a straight pipe is carried out for numerical validation. Then, we examine turbulent flow in helically coiled pipes using the fully turbulent flow from a straight pipe. An increase in the turbulent kinetic energy is observed at the first curve of helically coiled pipes. However, stabilization of the turbulent flow is observed towards the outlet, which is observed numerically for the first time. Due to the curved path and the centrifugal force, two counter-rotating vortices referred to as Dean vortices are observed. These vortices rapidly intensify the dissipation by creating smaller eddies in the flow and hence contribute to stabilizing the flow. We found that the higher curvature and lower torsion are associated with faster stabilization by modifying the geometry.

Lastly, numerical simulations of blood flow in the internal carotid artery (ICA), which shares geometrical characteristics with helically coiled pipes, are conducted with patient-specific geometries. Recent studies proposed the correlation between flow instability and the initiation of cerebral aneurysms in the ICA. Therefore, we aim to contribute to understanding the formation of flow instability in the ICA by applying the gained knowledge from helically coiled pipes. In some of the patients, 'turbulent-like' flow is found. A patient with stable flow has a higher curvature and lower torsion in the carotid siphon, which agrees with the results of helically coiled pipes. Dean vortices are observed for the first time and may be associated with flow instability in the ICA.

Acknowledgements

First and foremost, I would like to express my sincerest gratitudes to my supervisors Professor Mikael Mortensen, Dr. Kristian Valen-Sendstad, and Henrik Aasen Kjeldsberg for their guidance throughout these past two years. Mikael taught me the complex yet wonderful world of computational fluid dynamics. Kristian provided me many opportunities to learn the computational physiology and allowed me to pursue my own ideas. Henrik has been always helpful when I had technical difficulties. I have been fortunate to be able to learn under my supervisors. Also, I would like to thank Simula Research Laboratory, especially people at the Department of Computational Physiology, for giving me wonderful environment to learn wide aspects of computational physiology. Simula has definitely widen my eyes and cultivated my interests in the research of physiology. Special thanks go to the Department of Mathematics, University of Oslo for accepting me from Japan. Due to Covid-19, I was not sure if I could come to Norway in the first place, but I had learned a lot through my time at UiO.

I would also like to acknowledge funding from Scandinavia-Japan Sasakawa Foundation for the travel grants in the last two years.

The computations were performed on resources provided by Sigma2 - the National Infrastructure for High Performance Computing and Data Storage in Norway.

Last but definitely not least, I could not have completed this thesis without supports from my family in Japan and my partner, Ratee. I am grateful for their understanding and encouragement that I will never forget.

Kei Yamamoto
Oslo, May, 2022

Contents

List of Figures

List of Tables

Chapter 1

Introduction and Motivation

Fluid flows in helically coiled pipes have historically gained attention due to their occurrence in the human body, such as the cardiovascular and the respiratory system, and in engineering applications, such as heat exchangers and chemical reactors. Nonetheless, the complex physics of the flow in helically coiled pipes is not fully understood. Earlier works on the flow in curved or helically coiled pipes were analytical [3, 14, 22, 33, 84, 86] and experimental [2, 7, 11, 19, 20]. Numerical analysis [47, 85] was limited to low Reynolds numbers, i.e., laminar flow, and small curvature due to the lack of powerful computational tools.

In recent years, *computational fluid dynamics* (CFD) has emerged as a powerful tool to investigate the motions of fluid flow. CFD may reduce the cost and time necessary for experiments. It is easier to acquire the data from the entire flow field with CFD than through experiments. One of the things that CFD can give insight to is turbulence, which has been of great interest within fluid mechanics for the past decades. Turbulence is a state of fluid motion identified by apparently random and three-dimensional vorticity. Unlike the steady flow, turbulence is chaotic and unpredictable, making both the setting and measurements of the experiments very challenging. As computers have become more powerful, several numerical techniques have been developed for simulating turbulence, such as *Reynolds averaged Navier-Stokes* (RANS) [59] modelling, *Large-eddy simulation* (LES) [66], and *Direct Numerical Simulation* (DNS) [57]. RANS is the most computationally inexpensive approach where averaged motion of turbulence is resolved. The idea of LES is to ignore the smallest eddies by utilizing spatial filtering. LES is more accurate but computationally expensive than RANS. DNS is a type of simulation where the entire range of spatial and temporal scales of turbulence is resolved. Thus, DNS naturally requires enormous computational resources. A number of mesh points (N^3) necessary to perform DNS are known to exponentially grow as a function of Reynolds number (Re), $N^3 \geq Re^{9/4}$ [25]. For this reason, the application of DNS to very high Reynolds numbers or complex geometries is still a challenging problem in fluid mechanics.

In 1987, Kim et al. [40] applied DNS for the first time to simulate the fully developed turbulent flow between two parallel plates. The first DNS of turbulent flow in a straight pipe was carried out by Eggels et al. [17] in 1994. In recent years, Noorani et al. [55] used DNS to study the turbulent flow in

curved pipes. Wang et al. [78] investigated the turbulent flow in pipes with 90-degree bend using DNS. Although the basic idea of DNS is simple, the results obtained from DNS have proven to be extremely valuable in an attempt to understand turbulence in different geometries. Furthermore, results from previous studies [18, 40, 53] have been shared as DNS data set and are actively used for validations.

On the other hand, turbulent flow in helically coiled pipes has not yet been thoroughly studied using DNS. Hüttl and Friedrich [32] are the only ones to ever apply DNS to the turbulent flow in helically coiled pipes. They simulated turbulent flows in straight, curved, and helically coiled pipes. It was found that the flow in a helically coiled pipe was less turbulent than that of a straight pipe but was more turbulent than that of a curved pipe. This result indicates both the stabilization and destabilization effects of helically coiled pipes. These effects are also observed experimentally [28, 67]. Nevertheless, the mechanisms of stabilization and destabilization of flow in helically coiled pipes are unknown. Several other numerical studies of turbulent flow in helically coiled pipes were recently reported [12, 13, 28]. However, the focus of their study was on flow instability that triggers the transition from laminar flow to turbulence. As far as we know, there have been no numerical studies that addressed the transition from turbulence to laminar flow in helically coiled pipes. Therefore, we will investigate turbulent flow in helically coiled pipes with focus on the stabilization and destabilization of the flow.

Investigation of the flow in helically coiled pipes may also be applied to understand the flow structures in blood vessels as they are typically curved and twisted in three dimensions. CFD has been used in biomechanical applications to investigate the correlation between blood flow and the initiation and development of cardiovascular diseases in recent years. One example is cerebral aneurysms, bulges in the artery often located in the vicinity of the brain, and are thought to be present in $\approx 3\%$ of adults [76]. It is well known that the blood flow and the dynamics of blood flow (*hemodynamic*) are strongly affected by the vascular geometry (*morphology*) [36]. In addition, mechanical forces, such as wall shear stress, from blood flows are thought to have profound effects on the initiation of the cerebral aneurysms [56, 63]. Advanced medical imaging techniques enable measurements of the morphology to be easier and more accurate. Yet, direct measurements of the flow field and hemodynamics are still very challenging. Hence, CFD combined with patient-specific geometries has been utilized to study the physics of blood flow [62, 68]. Recent patient-specific CFD studies demonstrated a potential link between 'turbulent-like' flow and the initiation of the aneurysms [39, 74]. However, it is difficult to isolate the effects of specific geometrical parameters in patient-specific geometries as there are several parameters affecting flow patterns. Cerebral aneurysms are commonly formed at the bifurcation, especially in the internal carotid artery, which shares some geometrical characteristics with helically coiled pipes. Therefore, the gained knowledge from turbulent flow in helically coiled pipes may be used to understand flow instability in the ICA.

To summarize, the objective of this thesis is to investigate turbulent flow in helically coiled pipes using numerical simulations. Particularly, we will examine

the stabilization and destabilization effects of helically coiled pipes that are experimentally observed [28, 67] but not numerically investigated. Simulations of turbulent flow in a helically coiled pipe may also shed light on the initiation of cerebral aneurysms. To this end, we will take the following steps.

- First, turbulent flow in a straight pipe will be simulated using direct numerical simulations. The results will be compared against the published DNS data [18] for numerical validation purposes. In addition, turbulent flow obtained in a straight pipe will be used as an inlet velocity profile in a helically coiled pipe.
- Second, turbulent flow in helically coiled pipes will be simulated using data obtained from straight pipes. Five simulations based on different geometry will be shown and we will discuss the stabilization effects in the helically coiled pipe.
- Finally, numerical simulations of blood flow in patient-specific geometries of the internal carotid artery will be performed. We will analyze flow strictures in the internal carotid artery linking the flow in helically coiled pipes.

Chapter 2

Theory and Numerical Scheme

2.1 Turbulence

Turbulence has attracted people's attention for a long time and is a universal phenomenon that appears in many fields of science. In addition, turbulence appears in everyday life, from atmospheric circulation to when birds are flying. However, it is hard to define turbulence in a way that can cover all the characteristics it has. Therefore, it is common to list those characteristics when defining turbulence. Here are some of the essential properties that we know.

- Turbulence is irregular or random.
- Turbulence occurs at high Reynolds numbers.
- Turbulence is rotational and three-dimensional.
- Turbulence is a flow property and not a fluid property.

Figure 2.1 shows an example of the transition from laminar flow to by using a grid. Turbulence has a much more complex structure compared to laminar flow.

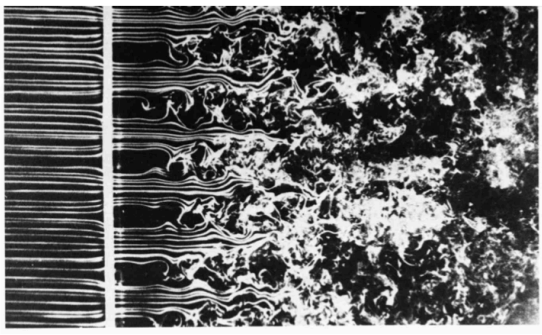

Figure 2.1: Transition from laminar (left) to turbulent (right) flow by a grid. Adapted from *An Album of Fluid Motion* (p.89) by van Dyke, M., & White, F. M. [16]

One of the most critical yet often overlooked characteristics of turbulence is that it is always a three-dimensional phenomenon and can never be two-dimensional. Turbulence involves the appearance of eddies of multi-scale and the energy cascade. During the process of energy cascade from larger eddies to smaller eddies, vortex stretching is observed due to the conservation of angular momentum. This lengthening of vortices can only happen in three-dimensional space. Therefore, even though it is possible to create "two-dimensional turbulence" numerically, such a simulation inhibits the vortex stretching.

2.1.1 Reynolds averaged Navier-Stokes (RANS) equations

Although it is impossible to predict the precise velocity or pressure at any point in time and space in turbulence, coherent structures may be observed. Mathematically, the existence of the coherent structure can be interpreted as having average values. In such a scenario, we can decompose the instantaneous velocity and pressure into two parts as described in the equation (2.1), averaged and fluctuating value.

$$\begin{aligned} \boldsymbol{u}(\boldsymbol{x},t) &= \overline{\boldsymbol{u}}(\boldsymbol{x},t) + \boldsymbol{u}'(\boldsymbol{x},t) \\ p(\boldsymbol{x},t) &= \bar{p}(\boldsymbol{x},t) + p'(\boldsymbol{x},t) \end{aligned} \tag{2.1}$$

Here overline denotes the average, and the prime denotes the fluctuating part. When the velocity and pressure may be decomposed into the mean and the fluctuating part, it is beneficial to derive equations that can predict the mean motion of the turbulence. We can do so by taking the average over the Navier-Stokes equations. The resulting equations are called Reynolds averaged Navier-Stokes (RANS) equations and are written as follows [79].

$$\begin{aligned} \frac{\partial \overline{\boldsymbol{u}}}{\partial t} + (\overline{\boldsymbol{u}} \cdot \nabla)\overline{\boldsymbol{u}} &= -\frac{1}{\rho}\nabla \bar{p} + \nu \nabla^2 \overline{\boldsymbol{u}} - \frac{\partial \overline{u_i' u_j'}}{\partial x_j} + \overline{\boldsymbol{f}} \\ \nabla \cdot \overline{\boldsymbol{u}} &= 0 \end{aligned} \tag{2.2}$$

where $\boldsymbol{u}$ is the velocity, p is the pressure, and $\boldsymbol{f}$ is the external force. Here $\overline{u_i' u_j'}$ is called Reynolds shear stress. This term introduces difficulty in analyzing turbulence as fluctuating velocity is often much more complex to obtain compared to the mean velocity.

As we will deal with turbulent flow in a circular pipe later, it is convenient to express RANS equations in terms of cylindrical coordinates. Here, we pay special attention to the case of pipe flow so that the mean flow is independent of the axial coordinate z and axisymmetric. This means that we assume $\overline{u}_\theta = 0$ and $\overline{u}_r = 0$. With these assumptions, the general RANS equations are reduced to

$$\frac{1}{\rho}\frac{\partial \overline{p}}{\partial z} = -\frac{1}{r}\frac{\mathrm{d}}{\mathrm{d}z}\left(r\overline{u_r' u_z'}\right) + \nu\left(\frac{\mathrm{d}^2 \overline{u}_z}{\mathrm{d}r^2} + \frac{1}{r}\frac{\mathrm{d}\overline{u}_z}{\mathrm{d}r}\right) \tag{2.3}$$

The equation (2.3) indicates that $\overline{u_r' u_z'}$ is the only Reynolds Stress in turbulent pipe flow.

2.1.2 Reynolds number related to turbulence

When dealing with the Reynolds number in the context of turbulence, several Reynolds numbers are used in the literature which may confuse the reader. Thus, the definition of the Reynolds number used in this thesis is given here. The first one is the bulk Reynolds number (Re_b) and it reads as follows.

$$Re_b = \frac{U_b D}{\nu} \tag{2.4}$$

where U_b is the mean bulk velocity, D is the diameter of the pipe, and ν is the kinematic viscosity. Bulk velocity is the average velocity over the cross-sectional area. In the case of straight pipe, it can be computed as

$$U_b \pi R^2 = 2\pi \int_0^R r u_z(r) \mathrm{d}r \tag{2.5}$$

where u_z is the streamwise velocity, r is the radial direction, and R is the radius of pipe. Secondly, Friction Reynolds number (Kármán number) is introduced as follows.

$$Re_\tau = \frac{u_\tau R}{\nu} \tag{2.6}$$

where u_τ is a so-called friction velocity defined as

$$u_\tau = \sqrt{\nu \frac{\partial \bar{u}}{\partial y}_{y=0}} \tag{2.7}$$

where $y = 0$ indicates that the velocity gradient is measured at the wall.

2.1.3 Q-criterion

Visualization of turbulence can be challenging. As turbulence consists of many vortices, one common practice is visualizing the vortex structures through Q-criterion. Q-criterion can extract the region where the vorticity magnitude is greater than the magnitude of the rate of strain [34].

$$Q \equiv \frac{1}{2}\left(u_{i,i}^2 - u_{i,j}u_{j,i}\right) = -\frac{1}{2}u_{i,j}u_{j,i} = \frac{1}{2}\left(\|\boldsymbol{\Omega}\|^2 - \|\boldsymbol{S}\|^2\right) > 0 \tag{2.8}$$

Here, $\boldsymbol{\Omega}$ and $\boldsymbol{S}$ are the symmetric and antisymmetric components of the velocity gradient.

2.2 Differential geometry of curves

As will be shown later, our focus on this thesis lies in the correlation between the geometry (*morphology* in the context of physiology) and the resulting flow patterns. We, therefore, introduce the necessary background knowledge in geometry with special attention to curves in the field of differential geometry.

2.2.1 Curvature and torsion of a helix

A circular helix is a type of smooth curve in three-dimensional space with the following mathematical definition.

$$\gamma(\theta) = (x, y, z) = (a\cos\theta, a\sin\theta, b\theta),\ \theta \in \mathbb{R} \tag{2.9}$$

where z is its axial direction, a is a constant representing the radius of the helix, and b is a constant where $2\pi b$ represents the pitch of the helix. An example is given as Figure 2.2.

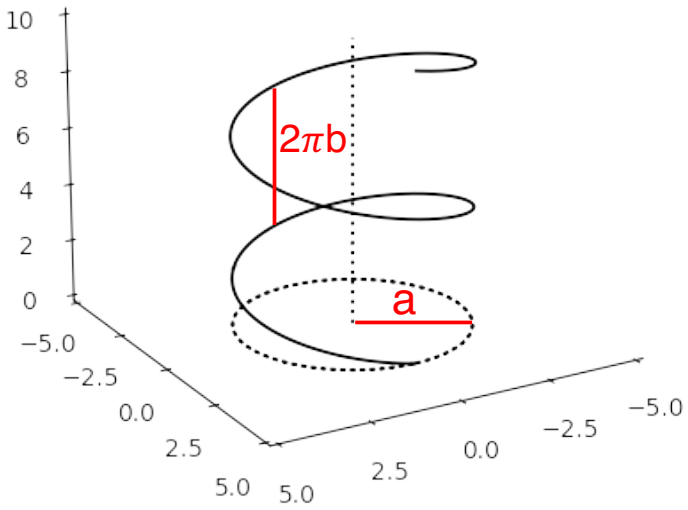

Figure 2.2: An example of a helix where a represents the radius of the helix and $2\pi b$ represents the pitch of the helix.

Curvature and torsion are the two scalar functions that together determine the shape of a curve in $\mathbb{R}^3$. It turns out that circular helixes are the only curves with constant curvature and torsion. Suppose that $\gamma(t)$ is a curve in $\mathbb{R}^3$, then its curvature is defined as ;

$$\kappa = \frac{\|\gamma'(t) \times \gamma''(t)\|}{\|\gamma'(t)\|^3} \tag{2.10}$$

Curvature measures the derivation of the curve from a straight line. Torsion on the other hand measures the derivation of the curve from lying on the same

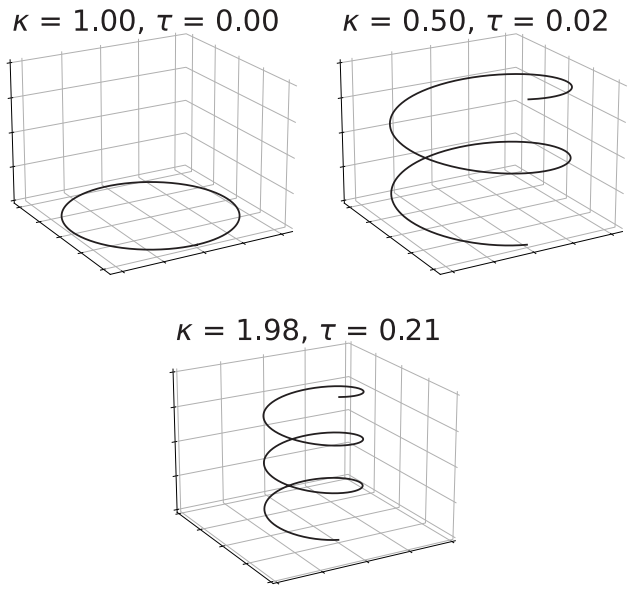

Figure 2.3: Examples of curves with (a) no torsion, (b) low, and (c) high curvature (κ) and torsion (τ). Curvature and torsion respectively represent the derivation of the curve from a straight line and lying on the same plane. Higher curvature and torsion are associated with the sharp bend of the helix.

plane where its mathematical definition reads as follows;

$$\tau = \frac{(\gamma'(t) \times \gamma''(t)) \cdot \gamma'''(t)}{\|\gamma'(t) \times \gamma''(t)\|^2} \tag{2.11}$$

In case of helices, we can compute the curvature and torsion as;

$$\kappa = \frac{|a|}{a^2 + b^2} \tag{2.12}$$

$$\tau = \frac{b}{a^2 + b^2} \tag{2.13}$$

Figure 2.3 shows three example of curves, where (a) has no torsion ($\tau = 0$), (b) and (c) respectively have low and high curvature and torsion.

2.3 Numerical scheme

To simulate fluid flow in different geometries, we will use a finite element Navier-Stokes solver called *Oasis* [52]. *Oasis* is built upon FEniCS [48] which is the computing platform for solving partial differential equations. In *Oasis*, we are solving the incompressible Navier-Stokes equations where the equation takes the following form.

$$\begin{aligned} \frac{\partial \boldsymbol{u}}{\partial t} + (\boldsymbol{u} \cdot \nabla)\boldsymbol{u} &= \nu \nabla^2 \boldsymbol{u} - \nabla p + \boldsymbol{f} \\ \nabla \cdot \boldsymbol{u} &= 0 \end{aligned} \tag{2.14}$$

where $\boldsymbol{u}$ is the velocity field, p is the pressure, ν is the kinematic viscosity, and $\boldsymbol{f}$ is the external force. The constant fluid density is incorporated into the pressure. *Oasis* has two major numerical schemes in it. One is the coupled solver where two equations are solved directly by assembling a large matrix. It has high accuracy and is also robust, but the computational cost is very expensive as it assembles all the governing equations into a linearized system of equations. The other scheme solves the equations in a segregated manner by splitting them into smaller equations. This segregated solver has lower accuracy than coupled solver due to the splitting of the equations but is more computationally efficient. In this thesis, we especially focus on the unsteady three dimensional flow, and thus segregated solver is better suited because of its computational efficiency.

In *Oasis*, a fractional step method is employed as a segregated solver. Discretization in time is performed using a finite difference scheme, while discretization in space is performed using finite elements. The generic fractional step algorithm with second order accuracy in time can be written as [65]

$$\frac{u_k^* - u_k^{n-1}}{\Delta t} + B_k^{n-1/2} = -\nabla_k p^* + \nu \nabla^2 u_k^{n-1/2} + f_k^{n-1/2} \qquad \text{for } k = 1, \ldots, d \tag{2.15}$$

$$\nabla^2 \phi = -\frac{1}{\Delta t} \nabla \cdot \mathbf{u}^\star \tag{2.16}$$

$$\frac{u_k^n - u_k}{\Delta t} = -\nabla_k \phi \qquad \text{for } k = 1, \ldots, d \tag{2.17}$$

where subscripts k and n denote spatial coordinates and temporal steps respectively. u^* and p^* are the tentative velocity and pressure whereas $\phi = p^{1/2} - p^*$ is a correction of the pressure. The non-linear convective term ($B_k^{n-1/2}$) is linearized by Adams-Bashforth projection,

$$B_k^{n-1/2} = \left(u_k^{n-1/2} \cdot \nabla\right) u_k^{n-1/2} \approx \left(\frac{3}{2} u_k^{n-1} - \frac{1}{2} u_k^{n-2}\right) \cdot \nabla u_k^{n-1/2} \tag{2.18}$$

and a Crank–Nicolson discretization is chosen for the term $u_k^{n-1/2} = 0.5(u_k^* + u_k^{n-1})$ to keep the second order accuracy in time. With all the dicretizations presented, the equation (2.15) is solved for all the tentative velocity components and the equation (2.16) for a pressure correction. In general, this process

can be repeated a desired number of times before solving the equation (2.17), which ensures the conservation of mass. In our simulations, this procedure is performed once. This scheme is selected based on the efficiency and long-term stability [65]. A shortcoming of this fractional step method is that an artificial boundary condition for the pressure is introduced as a result of splitting. This usually causes errors in the pressure at the boundary known as the numerical boundary layer. Based on the review paper by Guermond et al. [26], we have conducted the numerical tests to address the numerical boundary layer using different numerical schemes. The results are presented in appendix A as it is not directly associated with the scope of this thesis. Finally, we summarize the whole procedure of the fractional step as shown in Algorithm 1. Although we are still left with the spatial discretization, the reader may refer to the paper by Mortensen and Valen-Sendstad [52] for the variational formulations.

Algorithm 1 Fractional step method. Rewritten from Mortensen and Valen-Sendstad [52]

set initial conditions
$t = 0$;
while $t < T$ **do**
  $t = t + \Delta t$;
  while $error < max\_error$ and $iter < max\_iter$ **do**
    $\phi = p^* = p^{n-1/2}$
    solve eq. (2.15) for u_k^*, $k = 0, ..., d$
    solve eq. (2.16) for $p^{n-1/2}$
  end while
  $\phi = p^{n-1/2} - \phi$
  solve eq. (2.17) for u_k^n, $k = 0, ..., d$
  update to next time step
end while

Chapter 3

Method and Computational Details

In this chapter, we will present the methods and computational details for all the simulations done in this thesis. *Oasis* is used with linear basis functions for the velocity and the pressure. All the computations were parallelized through Message Passing Interface (MPI) on Saga Supercomputer maintained by NRIS - Norwegian research infrastructure.

3.1 Method for simulating turbulent flow in a straight pipe

3.1.1 Governing equations and computational domain

We considered the pressure-driven incompressible flow of a Newtonian fluid in a smooth pipe at $Re_b = U_b D/\nu = 5300$. The governing equations are written in dimensionless form

$$\nabla \cdot \mathbf{u} = 0 \tag{3.1}$$

$$\frac{\partial \mathbf{u}}{\partial t} + (\mathbf{u} \cdot \nabla)\mathbf{u} = -\nabla p + \frac{1}{Re_b}\nabla^2 \mathbf{u} \tag{3.2}$$

Re_b of 5300 is equivalent to a friction Reynolds number (Re_τ) of 180. Technically, *Oasis* solves the Navier-Stokes equations in dimensional form and the kinematic viscosity needs to be given. However, as our results will be all presented in dimensionless form, the value of the kinematic viscosity does not affect the results. The pressure gradient was applied to the axial direction only and is equal to $4u_\tau^2/D$, which can be derived from considering the momentum equation for a fully developed pipe flow as follows.

$$0 = -\frac{\partial P}{\partial z} + \frac{1}{r}\frac{\partial}{\partial r} r \left[-\langle u_z u_r \rangle + \nu \frac{\partial \overline{u_z}}{\partial r} \right] \tag{3.3}$$

Here z is the streamwise direction, r is the radial direction, $\langle u_z u_r \rangle$ is the Reynolds shear stress. Since P does not depend on r, we can multiply the equation (3.3) by r and integrate from the wall ($r = R$) to an arbitrary point r to get

$$u_\tau^2 = \left(\frac{r}{R}\right) \left[-\langle u_z v_r \rangle + \nu \frac{\partial \overline{u_z}}{\partial r} \right] - \frac{1}{2} \frac{\left(R^2 - r^2\right)}{R} \frac{dP}{dz} \tag{3.4}$$

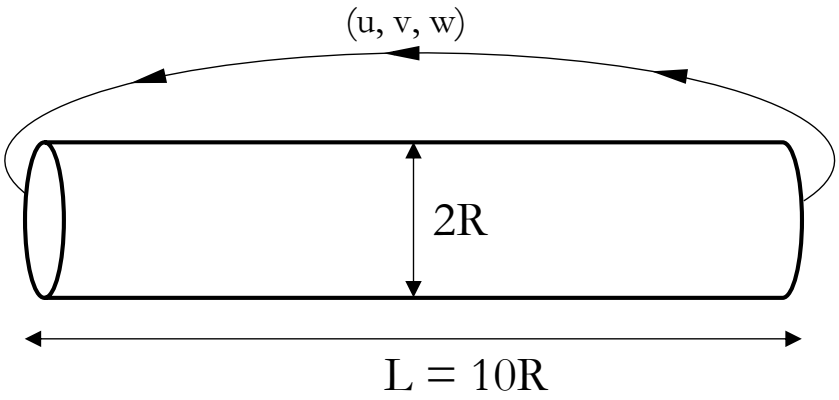

Figure 3.1: Schematic of pipe geometry and illustration of periodic boundary conditions. Here R is the pipe radius and L is the pipe length.

Integration to the centerline ($r = 0$) yields the relation between the pipe radius, the wall shear stress and the imposed pressure gradient as:

$$u_\tau^2 = -\frac{R}{2}\frac{dP}{dz} \rightarrow \frac{dP}{dz} = -\frac{2u_\tau^2}{R} = -\frac{4u_\tau^2}{D} \tag{3.5}$$

The computational domain is depicted in Figure 3.1. The radius of the pipe is denoted by R and the length of the pipe is L with $L = 10R$, which was chosen to capture the very large motion near the wall region. This pipe length is the same length used by other DNS studies [17, 21]. In *Oasis*, the Navier-Stokes equations are described in the Cartesian coordinate system. In this way, we avoided the singularity that might arise at the centreline with a cylindrical coordinate system.

Linear stability analysis shows [15] that the transition to turbulence from laminar flow could never happen for all Reynolds numbers if the circular pipe geometry is axisymmetric with no geometrical features that can generate angular velocities. For our simulations, small perturbations were initially added to the base laminar flow to trigger turbulence quickly. It is presumed that the magnitude of the perturbations needed to initiate the transition is proportional to Re^{-1} [29] but the actual value depends on the mesh. Thus, several simulations were conducted to find an appropriate magnitude of the perturbations.

To create turbulence efficiently in terms of computational cost, we employed the periodic boundary condition to the inlet and the outlet of the pipe. In this fashion, we can save computational costs since it can minimize the length of the pipe. However, it should be noted that the inlet and outlet of the pipe must have the identical mesh to achieve the periodic boundary condition, which is the limitation of FEniCS, not the requirement for periodic boundary conditions in general. Regarding the wall, no-slip boundary conditions have been applied.

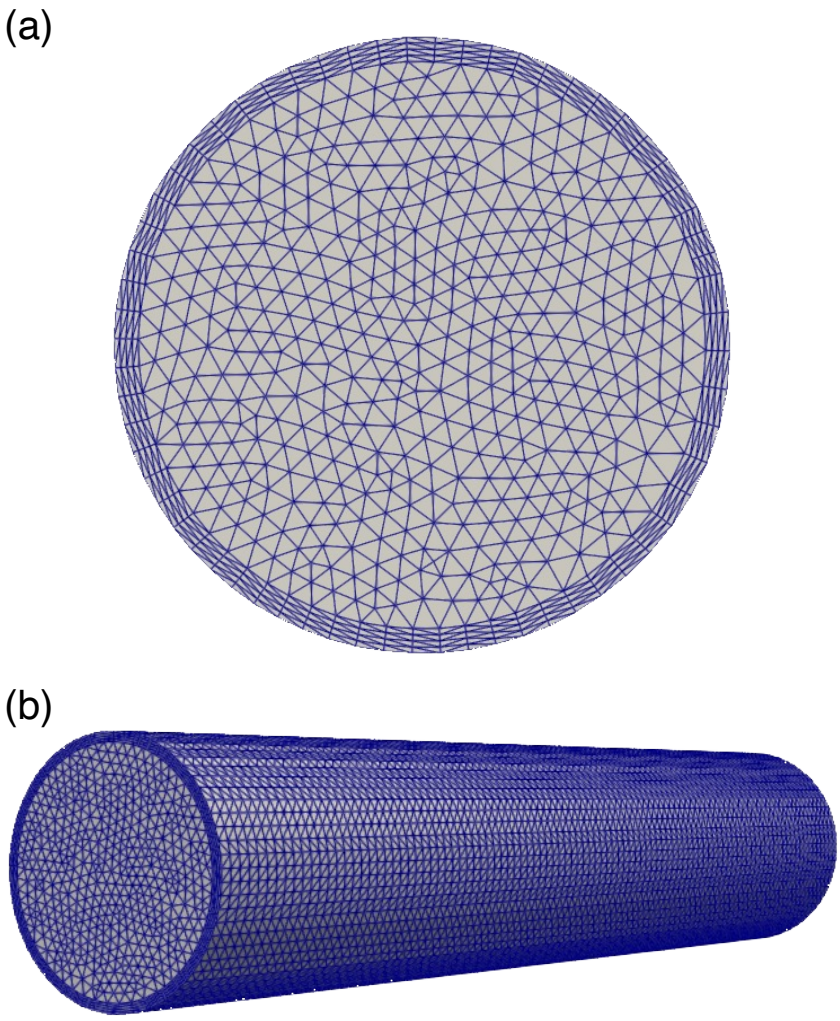

Figure 3.2: An example of the computational domain for the straight pipe. (a) shows the cross-section of the pipe with boundary layer mesh near the wall region and (b) is the entire domain made by extruding (a) in the axial direction.

The computation domain is generated by Gmsh [23], which is an open-source 3D finite element mesh generator. The example of the mesh is shown in Figure 3.2 and has two important features that are critical for the simulation. The first feature is that it has the so-called boundary layer mesh. Boundary layer mesh is a region with dense element distribution in the normal direction along the wall. This is essential in case the flow of interest involves a strong gradient near the wall, such as turbulence [27]. The other one is that all the cross-sections of the pipe have identical meshes. This is to achieve the periodic boundary condition. We first made a 2D circle mesh and extruded it in the axial direction to create the pipe.

3.1.2 Mesh refinement study and computational time setting

The goal of simulating turbulent flow in a pipe is to produce data sets that are as close as the DNS with moderate computational costs. To do so, we have conducted a mesh convergence test to determine the desirable mesh configuration.

In total, we have prepared three meshes (M1, M2, and M3). Cross-sectional view of the mesh is shown in Figure 3.3. They are respectively coarse (M1), intermediate (M2), and fine (M3) mesh. We will compute the mean velocity, turbulent intensity, and Reynolds shear stress for each mesh. These values will be compared against DNS results acquired by El Khoury et al. [18] to assess the sensitivity of the solution against the mesh configurations. In particular, we changed the number of cells of the whole domain and the property of the boundary layer mesh. The distance to the first node from the wall was also controlled to investigate the effect of different boundary layer mesh. A close view of the boundary layer mesh is shown in Figure 3.4. It can be seen that the boundary becomes smoother as the number of nodes consisting of the boundary is increased.

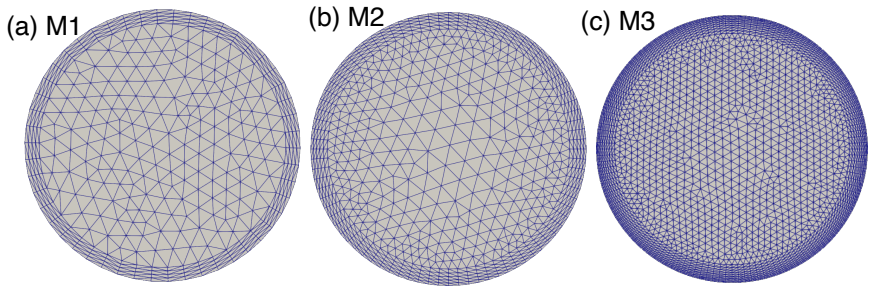

Figure 3.3: Cross-sectional view of the mesh showing the increase of the number of cells.

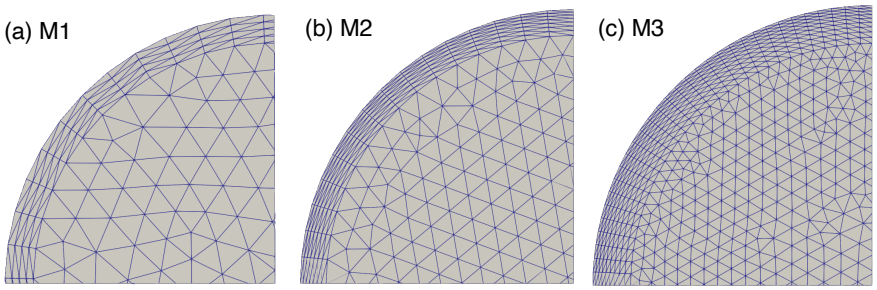

Figure 3.4: Quarter-section of the cross-sectional view of the mesh is shown to highlight the difference of boundary layer mesh. As the mesh resolution is increased, the boundary becomes smoother.

	# of cells	$h_{min,max}$	h_{avg}	y_1^+
M1	236,400	(0.133, 0.209)	0.161	4.73
M2	462,000	(0.112, 0.193)	0.130	3.61
M3	1,260,600	(0.105, 0.135)	0.113	1.80

Table 3.1: Summary of the mesh configurations. Number of cells, minimum, maximum, and the average of characteristic edge length, and the distance to the first node (y_1^+) from the wall normalized by the kinematic viscosity are shown.

Table 3.1 shows the summary of mesh properties. Here, y_1^+ represents the distance to the first node from the wall normalized by kinematic viscosity ν and friction velocity u_τ. The M1 mesh has the least number of cells and the mesh is coarser near the centerline region. The M2 mesh can be regarded as the improvement of M1 mesh as it has a larger number of cells and y_1^+ is smaller than that of M1. The M3 has the most number of cells and y_1^+ is the shortest of all and thus should produce the closest results to DNS case.

The initial velocity field was generated by parabolic flow with small perturbations that were created using a stream function constructed with random numbers. The computational time step was fixed at $\Delta t = 0.01$ and the sampling interval was $5\Delta t$ for all the simulations. We set $T = 2 \times 10^5 \Delta t$ for M1, M2 and $T = 6 \times 10^5 \Delta t$ for M3. Sampling was conducted during the last $5 \times 10^4 \Delta t$ which is equivalent to $\approx 190 R/\overline{U}_b$ where $\overline{U}_b$ is the mean bulk velocity. As the pipe length is $10R$, this is enough to allow a particle to travel through the pipe 19 times at the bulk velocity. The reason why the total computational time was different is that the time for the transition to occur became larger for the M3. We will discuss this later in the discussion. Briefly, this is because the velocity gradient between neighboring cells becomes smaller while a higher velocity gradient is necessary to trigger the transition. Hence, the total time steps and the start of the sampling were adjusted based on how many time steps were necessary to trigger the transition of the flow. Since it is impossible to predict in advance when turbulence appears, we first conducted the simulations to estimate the time for the transition and then performed simulations again based on the previous results to sample the data. We have used 8 central processing units (CPUs) for the M1 and 16 CPUs for the M2 and M3 cases. The code used for this chapter can be accessed at https://github.com/mikaem/Oasis/blob/master/oasis/problems/NSfracStep/StraightPipe.py, which, among other things, describes parameters, constructions of boundary conditions, initialization of velocity field, and a method for collecting data.

3.2 Method for simulating turbulent flow in helically coiled pipes

The method for simulating turbulent flow in helically coiled pipes is presented. Since we will use simulation results from the straight pipe as an inlet velocity profile, the main difference from the straight pipe is the geometry and boundary conditions. Most of the other parameters were kept constant. Thus, we will mainly explain how the computational domain is generated as well as well how we modified it to produce additional models.

3.2.1 Computational domains

Figure 3.5 illustrates the geometry of helically coiled pipes. Helically coiled pipes were made based on the helix whose mathematical description follows the equation (2.9). Cylindrical flow extensions were added to the inlet and outlet of the pipe that enabling us to use the pre-computed turbulence in a straight pipe without any coordinate transformation. The radius of the pipe was the same as the straight pipe. As *Oasis* solves dimensional Navier-Stokes equations, the specification of the units is practically required. Here, as a convention, we employed the International System of Unit, but the choice of the units would not affect the results.

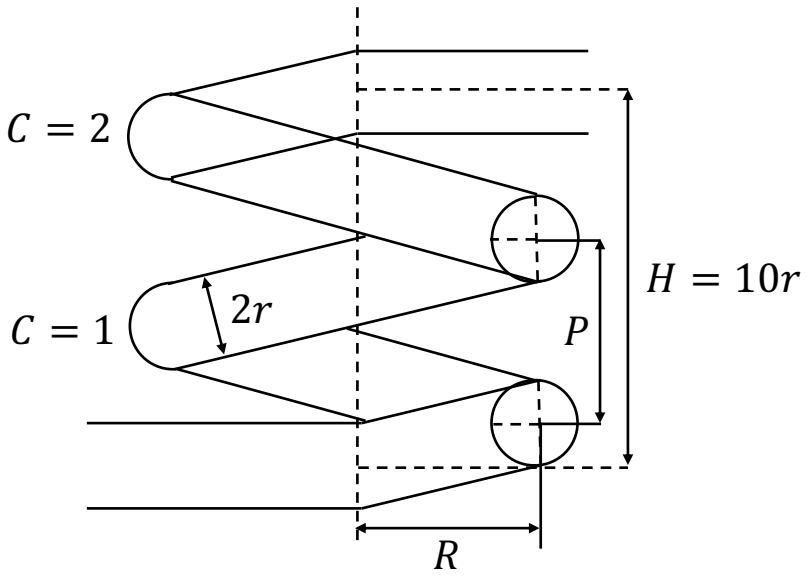

Figure 3.5: Schematic of helically coiled pipe with two coils (C=2). P represents the pitch of the coil and R represents the radius of the coil. H is the height of the coil and is fixed as $10r$ where r represents the radius of the pipe.

In total, we prepared 5 coiled pipes (i∼ v) and all meshes are shown in Figure 3.6. First, we made a default case (ii) where the number of coils (denoted as C) was 2 and the radius of the coil (denoted as R) was 3. Then, we either decreased or increased the number of coils (± C) and the radius of the coil (± R) to create additional four cases (i, iii, iv, v). The height of the pipe was kept constant. By decreasing the number of coils (- C, case i), the curvature was decreased while the torsion was increased. On the other hand, by increasing the number of coils (+C, case iii), the curvature was increased while the torsion was decreased. Decreasing the radius of the coil (-R, case iv) resulted in the increase of both curvature and torsion. Increasing the radius of the coil (+R, case v) resulted in the decrease of the both curvature and the torsion. Table 3.2 lists the summary of geometrical parameters and the details of mesh configuration. The number of cells and the length are also listed in the table 3.2. The length of the computational domain differs as we fixed the height of the coil. However, the number of cells per volume is all approximately set to 29000 to avoid numerical errors from spatial resolution.

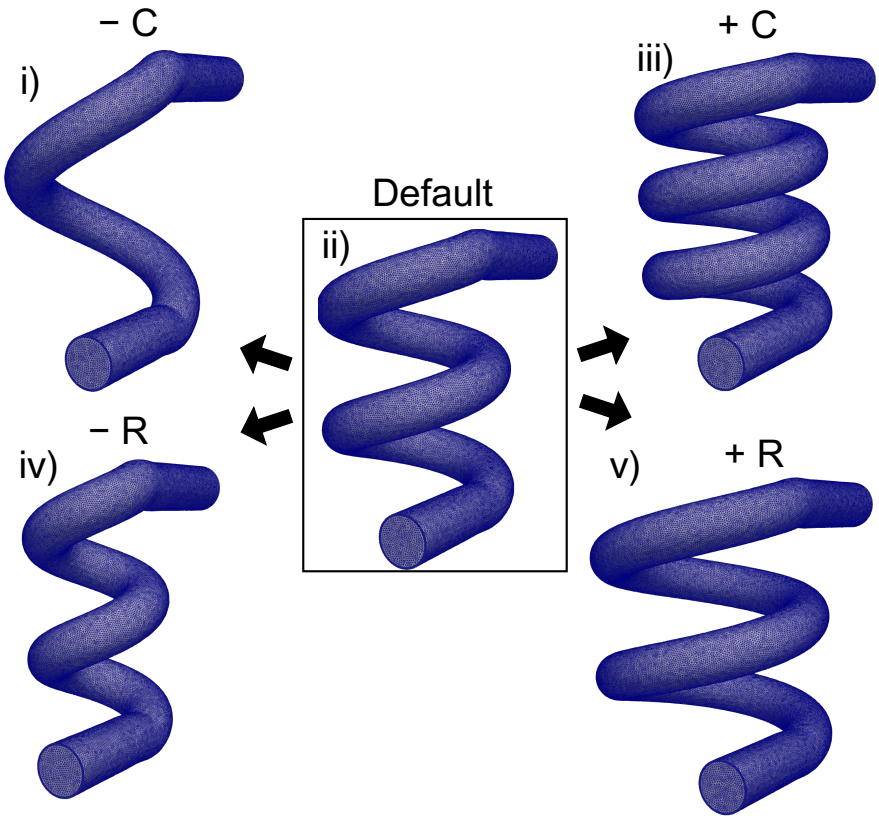

Figure 3.6: Volume mesh of helical pipes with different geometrical parameters. Here C and R represents the number of coils and the radius of coils, respectively. Based on the case ii), four additional models were created by changing the number of coils (±C) and the radius of the coil (±R).

case	C	R	P	κ	τ	N_c	L
i)	1	3	10	0.260	0.191	$2,99 \times 10^6$	32.114
ii)	2	3	5	0.311	0.105	$4,59 \times 10^6$	49.767
iii)	3	3	3.33	0.323	0.0572	$6,24 \times 10^6$	68.187
iv)	2	2	5	0.432	0.172	$3,49 \times 10^6$	38.820
v)	2	4	5	0.240	0.0478	$5,70 \times 10^6$	63.019

Table 3.2: Summary of the geometry and mesh configurations of coiled pipes. C represent the number of coils. The radius of the coil (R), pitch of the coil (P), curvature (κ), torsion (τ), length (L) are non-dimensionalized by the pipe radius r. Curvature and torsion are computed by equation (2.12) and (2.13). The number of cells (N_c) are also shown. Case i), ii), and iii) have the same radius of the coil while case ii), iv), and v) have the same number of coils.

In previous studies that used numerical [32] and experimental [28] method to investigate turbulent flow in helically coiled pipes, curvature (κ) was fixed to be 0.1. Here, we cover the range of the curvature from $\kappa = 0.24$ to $\kappa = 0.43$, thus higher range of curvature is covered. Torsion (τ) ranges from 0.0478 to 0.172 covering from small to large values.

Meshes were generated by using Gmsh [23] and The Vascular Modeling Toolkit (VMTK) [58]. We first made surface meshes by Gmsh and used them as inputs for VMTK for volume meshing. It would have been ideal to use only Gmsh for a simpler procedure but the boundary layer meshing was not possible with Gmsh at the time of writing. This is due to the complexity of the geometry, unlike the straight pipe where the extrusion was done for only one direction. For all the cases, four boundary layers were employed.

3.2.2 Boundary conditions and computational time setting

The simulation was started by the fully developed turbulent flow that was acquired from simulations with straight pipes at $Re_\tau = 180$. This is equivalent to the $Re = 5300$ at the inlet based on the bulk velocity and the pipe diameter. Due to the limitation of FEniCS, the inlet of the coiled pipe had to be identical to the cross-section of the straight pipe. Therefore, we have created five straight pipes corresponding to each coiled pipe and acquired the velocity field at the outlet of the straight pipe. At the wall, no slip condition was applied and the Dirichlet boundary condition for the pressure ($p = 0$) was realized at the outlet.

The same time step as straight pipes $\Delta t = 0.01$ was used. Total time steps were set to $8 \times 10^4 \Delta t$ and the sampling of the statistics was started after $4 \times 10^4 \Delta t$ with the sampling interval being $5\Delta t$. Either 16 CPUs or 32 CPUs were used depending on the number of cells. A python script used to run the simulation can be found at https://github.com/keiyamamo/Oasis/blob/master/oasis/problems/NSfracStep/CoiledPipe.py where problem specific parameters, initial conditions, and the boundary conditions are described.

3.3 Method for simulating blood flow in the internal carotid artery

Here, we will present the method for simulating blood in the internal carotid artery. Our cohort consists of ten healthy cases (P0086, P0134, P0157, P0163, P0207, P0220, P0228, P0250, P0251, P0252) from the Aneurisk database [49] where surface models are constructed from the 3D rotational angiography. Although we have conducted the simulations for all ten cases, five representative cases were selected for this thesis. We intentionally selected healthy patients. Our aim was to investigate the flow instability that might be associated with the initiation of the cerebral aneurysms. If we had chosen the patients with aneurysms, it could have been difficult to exclude the possibility of the flow instability as a consequence of cerebral aneurysms.

3.3.1 Mesh generation

Mesh generations from the surface models are done in an automated manner through the python script that is built upon VMTK [58] and each step will be explained in this subsection.

First, the surface model needs to be smoothed as the high frequency feature in the surface model may locally result in a poor quality mesh. Such a mesh can lead to the inaccuracy and divergence of the numerical solution when performing CFD study. There are multiple methods available for smoothing (e.g., laplace smoothing, taubin smoothing) but we have performed smoothing based on the Voronoi diagram. Briefly, the Voronoi diagram is a way to represent the three dimensional surface by points inside the domain and the inscribed sphere that are associated with the points. In general, points that are located near the surface have a smaller radius of the inscribed sphere while the points near the centerline have a larger radius of the inscribed sphere. The surface model can be smoothed by removing the points that have a small radius of the inscribed sphere. Here, we removed the sphere with less than 25% of the maximum radius in the model. As the Voronoi diagram is a mathematical way of representing the surface, it is an objective way of smoothing the surface. Note that the smoothing of the surface is to be done only to remove the high frequency features and the care needs to be taken to preserve the original surface as much as possible.

Following the smoothing of the surface mesh, the cylindrical extensions to the inlet and outlet need to be added. Adding flow extensions has several purposes. For the inlet, the flow must be developed before it enters the ICA as the Womersley boundary condition, which will be explained in the next subsection, is applied to the inlet. For the outlet, it is crucial to have a flow extension to avoid numerical instability often caused by incoming velocity referred to as backflow. This problem may happen as only the boundary condition for the pressure is prescribed at the outlet [6]. It is important to remind that the adding flow extension increases the computational cost as the number of cells increases, and hence the length of the flow extensions should be as short as possible. Figure 3.7 shows an example of the surface model after the surface is smoothed and the flow extension is added.

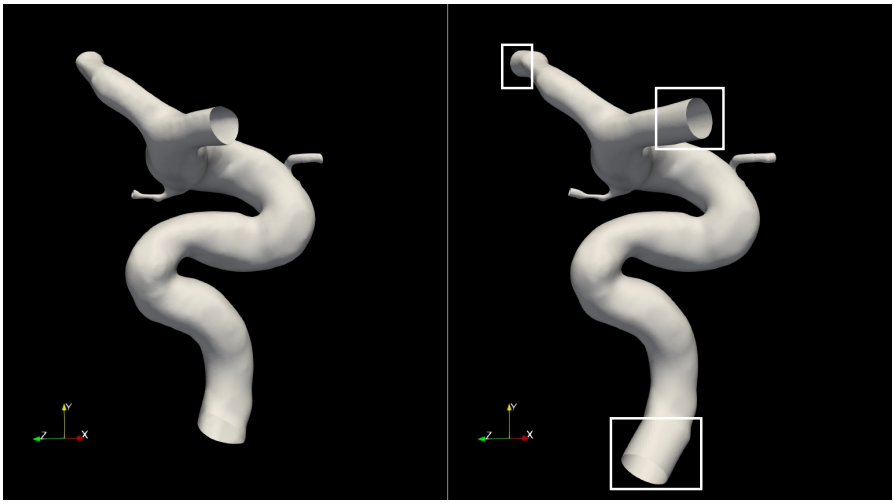

Figure 3.7: Example of surface model (P0086) after the surface is smoothed and the flow extensions are added to the inlet and outlets. Left is the original model; Right figure is the modified model.

After the surface model is improved, the surface meshing is to be performed which will then be used to perform the volume meshing. We have three ways of performing the surface meshing within our framework depending on the way of computing the edge length of each cell. The first and the simplest way is to impose the constant edge length for all the cells. This method can be useful if the geometry is relatively simple and the flow patterns are expected to remain the same. However, when the geometry is complex and the flow is assumed to experience the transition it is necessary to have a denser mesh in the vicinity of the complex geometries. One way to accomplish such a meshing is to compute the edge length based on the distance to the centerline. It is well known that the flow can become unstable in the narrow region where the surface is close to the centerline and thus higher resolution of the mesh is desired. The other way is to compute the edge length based on the surface curvature. When the surface has higher curvature it can also lead to unstable flow and a higher resolution of the mesh is also required. In our case, we performed surface meshing based on the distance to the centerline.

Finally, the volume meshing is performed based on the surface mesh. Generating boundary layer mesh is possible with VMTK [58] and is preferable for our simulations as the flow of interest is transient. Four boundary layers were created and the total number of the cells ranges from approximately three million to eight million depending on the patient-specific geometry. Based on the previous studies, it is known that this meshing resolution is more than adequate to detect the flow instability [38, 72]. The volume meshing algorithm of VMTK is relied on TetGen [64]. Figure 3.8 shows an example of a volume mesh with an enlarged view of the inlet with four boundary layers. Table 3.3 lists the mean curvature and torsion, the number of cells, and the minimum and the maximum Reynolds number of five selected ICA.

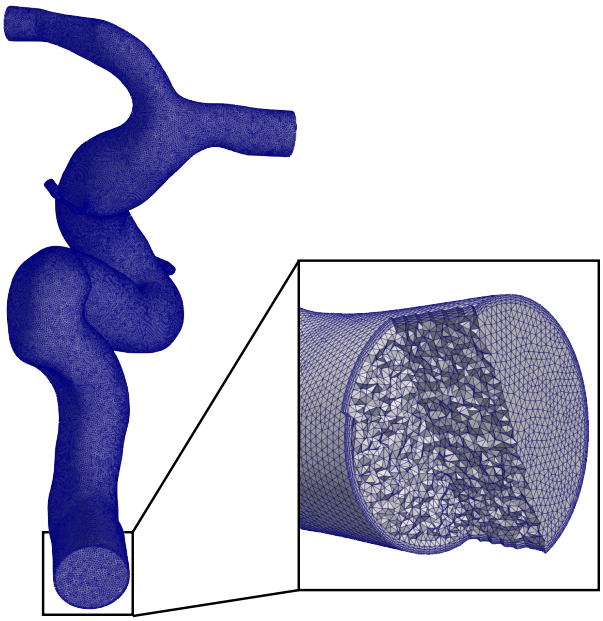

Figure 3.8: Example of volume mesh (P0086) with an enlarged view at the inlet with boundary layer. Part of the volume mesh is clipped to show the inside of the domain.

case	κ [mm^{-1}]	τ [mm^{-1}]	Number of elements [-]	Re_{inlet} [-]
P0207	0.189	-0.0142	4.42×10^6	115 $\sim$ 582
P0220	0.194	0.343	5.81×10^6	141 $\sim$ 712
P0228	0.212	0.0545	3.75×10^6	150 $\sim$ 758
P0250	0.134	-0.130	6.87×10^6	167 $\sim$ 845
P0252	0.178	-0.0904	2.84×10^6	162 $\sim$ 820

Table 3.3: Mean curvature (κ), torsion (τ), the number of the elements, and the minimum and maximum Reynolds number at the inlet of the patient-specific geometry of the ICA are listed.

3.3.2 Boundary conditions and computational time setting

To simulate the flow in a patient-specific geometry of the ICA, boundary conditions are required for both inlet and outlet. For the inlet boundary condition, we have used Womersley flow which is a pulsatile blood flow named after John R. Womersley [81]. The form of Womersly flow depends on several parameters, such as fluid density and pulsatile frequency. In this thesis, we used the waveform from Hoi et al. [30] to specifically adjust the Womersly flow so that it is similar to the flow in ICA of older adults. Figure 3.9 illustrates the waveform we used.

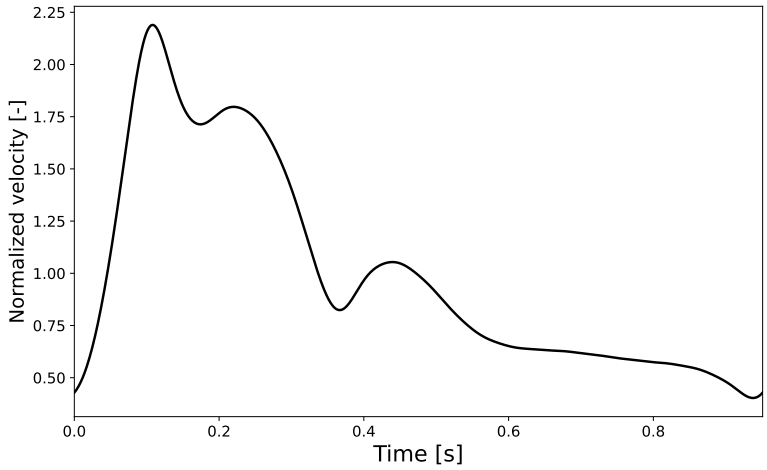

Figure 3.9: Normalized velocity waveform taken from Hoi et al. [30]. The waveform represents the velocity profile in the ICA of older adults during one cardiac cycle.

We used the following approximation of the mean flow rate as proposed by Valen-Sendstad et al. [75] where Q is the flow rate and A is the cross-sectional area of the inlet.

$$Q = 0.27A \tag{3.6}$$

At the outlets, the boundary condition for the pressure was applied and was iteratively adjusted during the simulation as the inlet boundary condition was time-dependent. Since we have bifurcation and several outlets depending on the patient-specific geometry, the pressure condition for each outlet needs to be computed to correctly achieve the flow division. To this end, we used the so-called dual-pressure boundary condition developed by Gin et al. [24]. At the dth outlet, pressure P_d is corrected using a power-low of the form

$$P_{d,\text{new}} = \beta P_{d,\text{old}} \cdot M_{\text{err}}^{E} \tag{3.7}$$

where M_{err} is the mass flow error described as

$$M_{\text{err}} = \frac{R_{\text{desired}}}{R_{\text{actual}}} \tag{3.8}$$

where R is the flow ratio at the bifurcation. E is an exponent that controls the magnitude and direction of the pressure with the following definition.

$$E = \begin{cases} 1 + \dfrac{|R_{\text{desired}} - R|}{R_{\text{desired}}}, & \text{for } P_{d,\text{ old}} < 0 \\ -\left(1 + \dfrac{|R_{\text{desired}} - R|}{R_{\text{desired}}}\right), & \text{for } P_{d,\text{ old}} > 0 \end{cases} \tag{3.9}$$

β in the equation (3.7) is a relaxation coefficient used to accelerate the convergence when R is far from R_{desired}. We prescribed a no-slip boundary condition for the boundary at the walls.

One cardiac cycle is known to be 0.951 s on average [30], and we set the time step to be $\Delta t = 9.51 \cdot 10^{-5}$ ms, which is $1 \times 10^4 \Delta t$ per one cardiac cycle. The simulation was run for two cardiac cycle but only the results from second cycle was collected to disregard the non-physiological effects from the first cycle. The kinematic viscosity was set to $\nu = 3.3081 \cdot 10^{-6} \text{m}^2\text{s}^{-1}$ to mimic the blood flow.

Chapter 4

Results and Discussion

4.1 Direct numerical simulations of turbulent flow in a straight pipe

The result of direct numerical simulations of turbulent pipe flow is presented. Our results are compared against DNS results done by El Khoury et al. [18] for numerical validation purposes.

4.1.1 Instantaneous velocity and vorticity

Figure 4.1 represents the instantaneous velocity magnitude sliced along the axial direction for all cases. In all cases, random behavior of flows can be observed. The coarse mesh (M1) has relatively high velocity along the wall compared to the intermediate (M2) and the fine (M3) mesh. This indicates the importance of having dense meshes near the boundary.

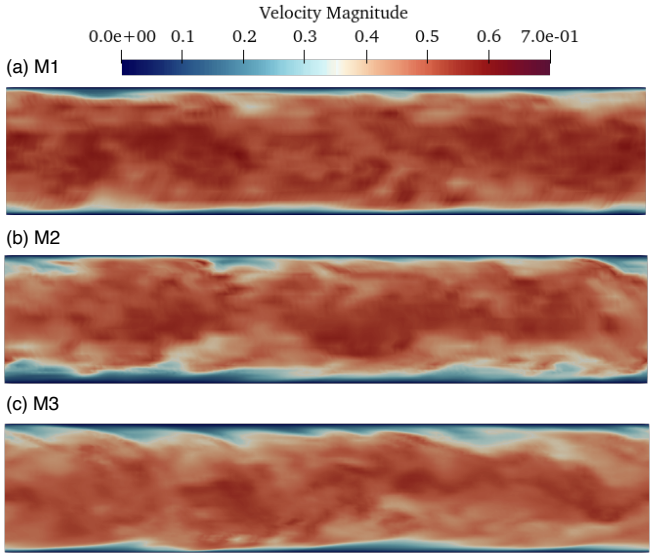

Figure 4.1: Instantaneous velocity sliced along the axial direction obtained from the (a) coarse (M1), (b) intermediate (M2), and (c) fine (M3) mesh.

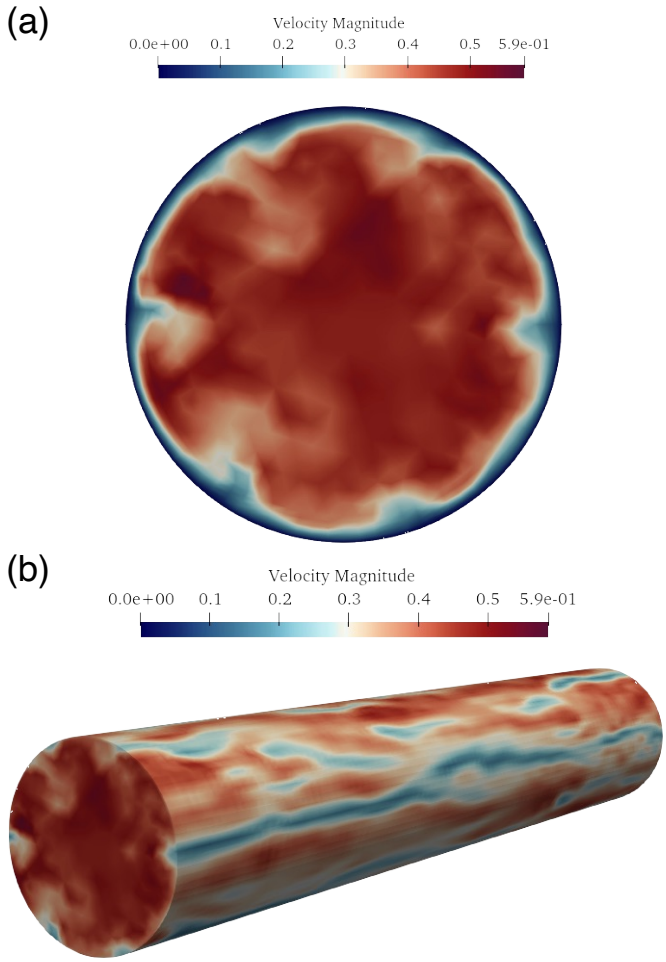

Figure 4.2: Instantaneous velocity magnitude taken from the M2 case. (a) represents cross-sectional view at $z = 0.5L$ where z is the axial coordinate and L is the total length of the pipe. (b) shows flow field on the surface at $r = 0.9R$ where r is the radial coordinate and R is the radius of the pipe. Long wavy flow structures can be observed near the wall.

Next, the general flow features based on the simulation results from the intermediate mesh resolution (M2) will be presented. Although there was slight difference of the velocity field between each mesh configuration, all cases shared the similarity. Figure 4.2 shows the instantaneous flow field where (a) is a cross-sectional view of velocity magnitude and (b) shows flow field of near wall region $r = 0.9R$. Figure 4.2 (a) indicates the variations of the velocity magnitude near the wall region. Figure 4.2 (b) shows that the flow exhibits a turbulent structure near the wall and a large wavy fluid structure can be observed. This demonstrates the importance of having long pipe length to capture the large motion near the wall.

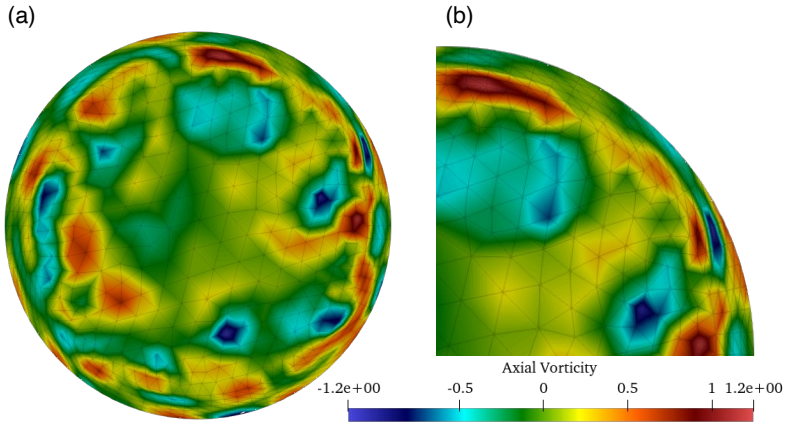

Figure 4.3: (a) Cross-sectional view of axial vorticity and (b) enlarged view of the upper right quarter of the (a) where small pairs of positive and negative vorticity are apparent manifesting the conservation of momentum.

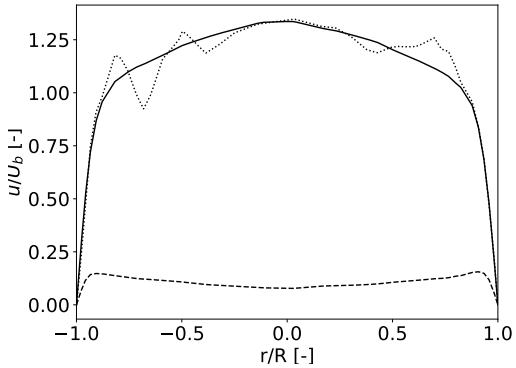

Figure 4.4: Velocity plot over the horizontal line of cross-section of the pipe. The straight curve represents the mean velocity (——). The dotted and dashed plot is an instantaneous velocity (·····) and the root-mean-square of the fluctuating velocity component(- - -), respectively. Velocity is normalized by the bulk velocity U_b and the radial coordinate is normalized by the pipe radius R.

Instantaneous axial vorticity is shown in Figure 4.3. There are strong vorticities near the wall compared to near the centerline region. Pairs of vortices with positive and negative values manifesting the conservation of momentum can also be observed. Near the centerline, no strong vorticity was observed. Figure 4.4 shows the plot of mean, instantaneous, and the root-mean-square (r.m.s) of fluctuating velocity over the horizontal line of a cross-section of the pipe. The mean velocity follows the parabolic profile with symmetry that is similar to the laminar flow. The instantaneous and the r.m.s of fluctuating velocity indicate the strong variation of velocity near the wall region.

4.1.2 Statistical results

Statistical results from our simulations will be shown as well as the results from El Khoury et al. [18]. In this subsection, an overline denotes time averaging, superscript + refers to normalized quantities by friction velocity u_τ for velocity, and by viscous wall unit ν/u_τ for distance. Ideally, we would quantitatively compare the results with El Khoury et al., but such a comparison is difficult. This is because their results are all scaled with parameters based on their simulation results, not the prescribed parameters. Therefore, only qualitative comparison is possible against DNS while quantitative comparison among our simulations is still possible.

Figure 4.5 shows the comparison of mean axial velocity for all the meshes against DNS of El Khoury et al. [18]. The mean axial velocity was plotted against $y^+ = (1-r)^+$, which is a dimensionless distance from the wall. In general, our simulations predicated the axial mean velocity well near the wall region as the boundary layer mesh was used. On the other hand, all the cases over-predicted the mean velocity at $(1-r)^+ > 10$. When it comes to the difference between each case, there is a large improvement in accuracy from the coarse (M1) to the intermediate (M2) while the M2 and the fine (M3) mesh predicted the mean axial velocity well compared to El Khoury et al. No clear difference between M2 and M3 was observed.

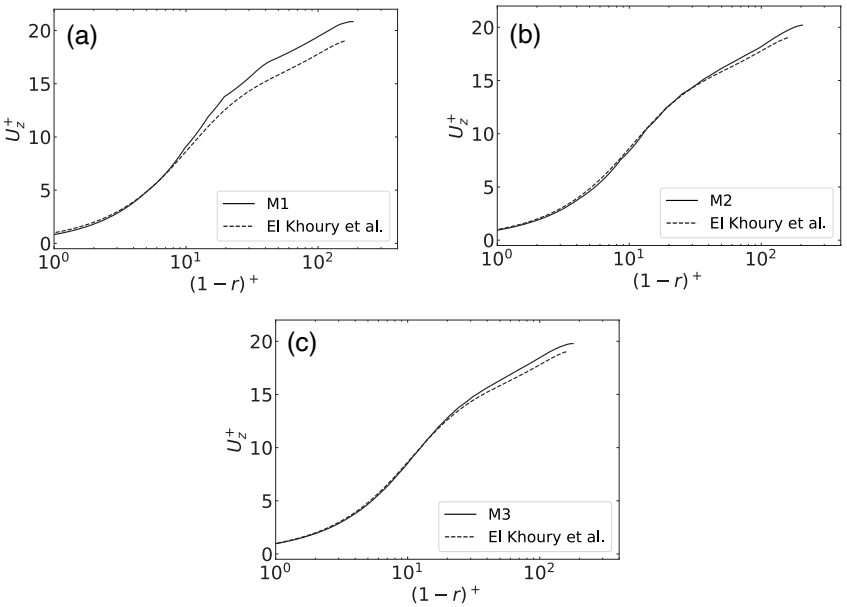

Figure 4.5: Mean axial velocity U_z^+ as a function of distance from the wall where (a), (b), and (c) show the results for the meshes M1, M2, and M3, respectively. Dashed black curves (- - -) are the DNS results obtained by El Khoury et al. [18].

The r.m.s of the fluctuating velocities (also called turbulent intensity) and Reynolds shear stress are shown in Figure 4.6. Figure 4.6 (a) shows the axial component of turbulent intensity and all the simulations over-predicted the value compared to El Khoury et al. [18]. However, the discrepancy was weakened as the number of cells increased. Especially, the improvement from the M1 to M2 is clear. Figure 4.6 (b) and (c) respectively show radial and azimuthal components of the turbulent intensity. Contrary to the axial component, radial and azimuthal components were generally under-predicted. Finally, the only non-vanishing Reynolds shear stress $\langle u_z u_r \rangle^+$ is shown in Figure 4.6 (d). As the Reynolds shear stress is the product of the radial and azimuthal components of the fluctuating velocity, the under-prediction of the M1 and M2 and the over-prediction of the M3 at the peak can be understood from examining Figure 4.6 (b) and (c). This over-prediction of the axial turbulent intensity and the under-prediction of the radial and azimuthal turbulent intensity is also reported by Wu and Moin [82] with coarse DNS or Large-eddy-simulation calculations. Although the general improvements in the accuracy can be observed with finer mesh resolution, the results indicate that the higher order quantities converged slower to the DNS than the mean axial velocity.

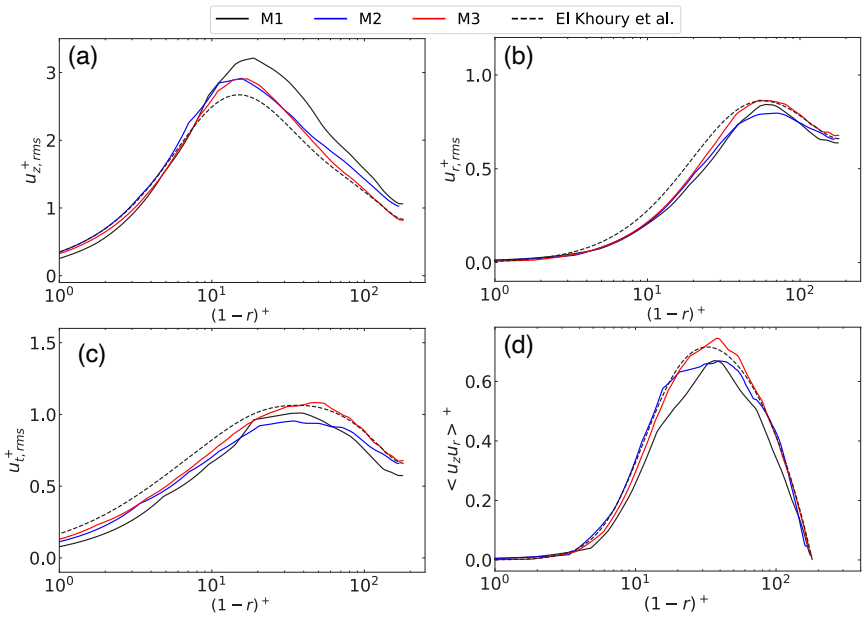

Figure 4.6: Turbulent intensities and Reynolds shear stress scaled by u_τ and u_τ^2, respectively. Turbulent intensities are shown in the (a) axial direction (b) radial direction (c) azimuthal direction. (d) shows the only non-vanishing Reynolds shear stress $< u_z u_r >^+$. Each line in the plot represents M1(——), M2(——), M3(——), DNS by El Khoury et al. (- - -). In general, the convergence towards the DNS can be observed as the mesh resolution is increased.

4.1.3 Effects of under-resolution on statistics

Although our simulations showed agreements with DNS data, it is clear that the simulation was under-resolved, meaning motions of the smallest eddies were not captured. To investigate the effect of under-resolution, it is beneficial to introduce the equation for turbulent kinetic energy. Such an equation can be derived by manipulating the instantaneous Navier-Stokes equations and the Reynolds averaged Navier-Stokes equations. The derivation is omitted here (attributed to Appendix B), but the equation for the turbulent kinetic energy reads

$$\begin{aligned}\frac{\partial k}{\partial t} + \bar{u}_j \frac{\partial k}{\partial x_j} = &- \frac{\partial}{\partial x_j}\left(\frac{1}{\rho}\overline{p' u_i'}\delta_{ij} + \frac{1}{2}\overline{u_i' u_i' u_j'} - 2\nu\overline{s_{ij}' u_i'}\right) \\ &- 2\nu\overline{s_{ij}' s_{ij}'} - \overline{u_i' u_j'}\frac{\partial \bar{u}_i}{\partial x_j}\end{aligned} \tag{4.1}$$

where the first term on the right hand side of the equation represents the production of the turbulent kinetic energy, i.e., kinetic energy is removed from the mean motion and added to the fluctuations.

$$P = \overline{u_i' u_j'}\frac{\partial \bar{u}_i}{\partial x_j} \tag{4.2}$$

The forth term of the right hand side of the equation appear as rate of dissipation of turbulence kinetic energy per unit mass due to viscous stresses, which act to reduce the turbulent kinetic energy.

$$\varepsilon = 2\nu\overline{s_{ij}' s_{ij}'} \tag{4.3}$$

where

$$s_{ij}' = \frac{1}{2}\left(\frac{\partial u_i'}{\partial x_j} + \frac{\partial u_j'}{\partial x_i}\right) \tag{4.4}$$

From the equation (4.2), the production of the turbulent kinetic energy depends on the gradient of the mean velocity. The rate of dissipation, on the other hand, depends on the gradient of the fluctuating components of the velocity, as can be seen from the equation (4.3) and (4.4). Using under-resolution is that the smallest scale of the velocity is not resolved, whereas the smallest eddies have a higher dissipation rate and fluctuating velocity. Thus, under-resolution led to under-prediction of the total dissipation of the flow and fluctuating components of the velocity compared to DNS. Over-prediction of the mean axial velocity near the centerline of the pipe observed in Figure 4.5 is a consequence of under-prediction of the dissipation. This over-prediction of the mean velocity can explain the larger over-prediction of the axial component of turbulent intensity near the centerline in Figure 4.6 (a) as the production of the turbulent kinetic energy depends on the mean velocity. We also observed the under-prediction of the turbulent intensity in radial and azimuthal directions. This indicates that too little turbulent kinetic energy was transferred from the axial to the radial and azimuthal components. The kinetic energy was introduced to the axial direction by the pressure gradient and should be distributed to the radial azimuthal directions.

4.1.4 Effects of using higher order basis functions for the velocity

To achieve mesh refinement, we simply increased the number of elements while polynomial orders used as basis functions were kept constant. Mesh refinement can also be accomplished by using higher order polynomials at the cost of computational time while the meshing remains unchanged. However, as our domain consists of circles, the number of nodes that create the boundary circle has a crucial effect on the flow field. This is because a smaller number of nodes consisting of the boundary may introduce the surface roughness and hence perturbations in the velocity field. To demonstrate the difference between using a larger number of elements and the higher order of basis functions, we have computed the mean axial velocity by using second-order polynomials (P2) for the velocity and first-order polynomials (P1) for the pressure.

Figure 4.7 shows the comparison of mean axial velocity for the coarse (M1) case with linear and quadratic basis functions, and the intermediate (M2) case with linear basis functions. Using quadratic basis functions improved the accuracy of predicting the mean velocity compared to linear basis functions with the same number of elements. However, the result with quadratic basis functions from the M1 case had poorer accuracy than those with linear basis functions from the M2 case. This confirms that the number of nodes that consists of the boundary circle has a larger impact on the accuracy than the order of basis functions. This is not the case when the boundary of the domain is made of straight lines as the number of nodes is not related to the surface roughness.

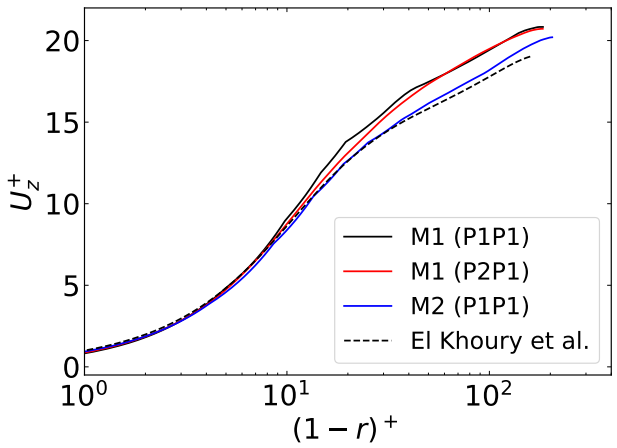

Figure 4.7: Axial mean velocity as a function of distance from the wall. The black and red curve represents the coarse mesh (M1) results with linear (P1P1) and quadratic (P2P1) basis functions, respectively. The blue curve represents the intermediate mesh (M2) result with linear basis functions indicating the higher accuracy with a larger number of cells than using higher order basis functions.

We also computed the Reynolds shear stress using quadratic basis functions to investigate how the results converge to the DNS. In this case, the fine mesh (M3) was used. The results are shown in Figure 4.8. Although using quadratic basis functions for M3 case (1.26 M cells) should be equivalent to using $1.26 \times 8 \approx 10$M cells for the velocity with linear basis functions, the obvious improvement from using linear basis functions was not observed. This implies the difficulty of acquiring high accuracy for the higher order quantities with lower order basis functions.

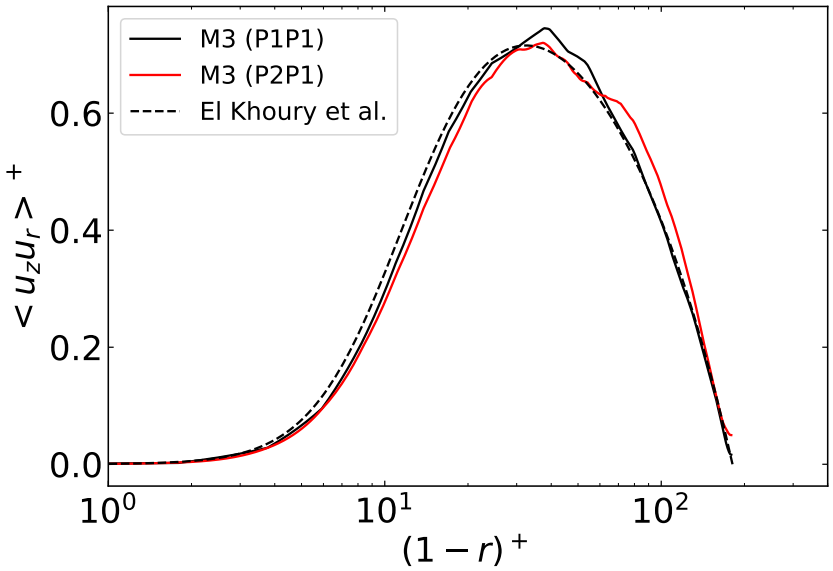

Figure 4.8: Reynolds shear stress as a function of distance from the wall for the fine mesh (M3). The black and red curve represents the results with linear (P1P1) and quadratic (P2P1) basis functions, respectively. The result highlights the difficulty of acquiring the high accuracy for the Reynolds shear stress even with the fine mesh (M3) with quadratic basis functions for the velocity.

4.1.5 Computational cost and the accuracy of the results

The objective of this section was to find the proper mesh configuration that can reproduce the results from DNS with moderate computational cost. Based on the results from the mesh refinement test, convergence towards the DNS results was observed. Therefore, a higher mesh resolution is desired to generate turbulent flow, but that requires larger computational costs. It is worth mentioning that the total computational time steps needed for the fine mesh (M3) was three times larger than the coarse (M1) and the intermediate (M2) mesh. For the M3 case, longer time steps were necessary for the transition to occur and the flow to become statistically steady. Figure 4.9 shows an instantaneous velocity field at $t = 100000\Delta t$ for all the cases. The only difference between the M1, M2, and M3 was the mesh resolution, and the other parameters were kept constant. It is

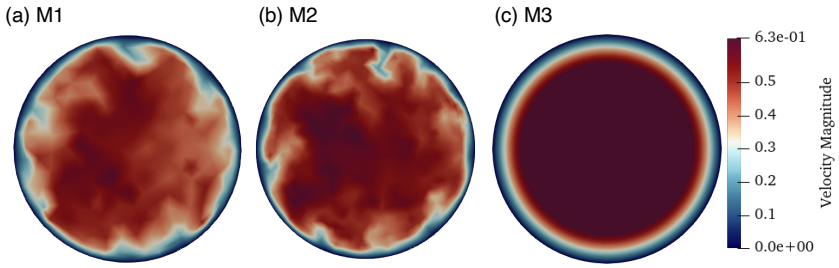

Figure 4.9: Cross-sectional view of instantaneous velocity field at $t = 100000\Delta t$. Turbulent flow was already developed in the coarse (M1) and the intermediate (M2) mesh while laminar flow was still observed in the fine mesh (M3). This led to the increase of total computational time for the M3 case.

clear from the Figure 4.9 that the turbulent structure was already observed for the M1 and the M2, while the M3 still had laminar flow. This led to an increase in total computational time steps for the M3 case. Although increasing the number of CPUs could speed up the time for one computational time step, the M2 case showed good agreement with the DNS, and no significant difference in the accuracy of statistics was observed from the M3 case. Therefore, we concluded that the M2 case is the most appropriate mesh configuration to be used as it had small discrepancy from DNS data with moderate computational costs.

4.1.6 Limitations and summary

There are several limitations of our simulations. The first limitation is the pipe length. Chin et al. [10] recently reported the minimum pipe length necessary for the convergence of turbulence statistics. They concluded that, respectively, pipe length $\approx 6R$ for the mean velocity and $\approx 13R$ for the turbulent intensity are necessary for the convergence of statistics at $Re_\tau = 170$. In our case, we carried out simulation with $L = 10R$ for $Re_\tau = 180$. Thus, our pipe length was sufficient for the mean velocity but not the turbulence intensity. This explains the slower convergence of the turbulent intensity of our simulations in addition to the under-resolution. Secondly, the spatial refinement was conducted but not the time refinement. We understand that the increasing time resolution could improve the accuracy. However, we prioritized generating data sets with reasonable computational time as we did not observe any numerical instability with the employed time step.

To summarize, we have demonstrated that *Oasis* is capable of simulating turbulent flow in a straight pipe at $Re_\tau = 180$ with high accuracy on parallel clusters. We have computed the mean velocity, turbulent intensity, and the Reynolds shear stress for all the mesh configurations. The convergence towards the DNS results by El Khoury et al. [18] was observed. The effects of using under-resolved simulation are the over-prediction of the axial mean velocity and the turbulent intensities near the centerline of the pipe. We also found that using higher-order basis functions for the velocity has a smaller effect on

the accuracy when the number of the cells is relatively small. This is because the surface roughness impacts the solution. As we did not observe the large difference in the solutions between the intermediate (M2) and the fine (M3) mesh, the M2 case was chosen to be used for an inlet velocity profile of helically coiled pipes. In this way, we can reduce the total computational cost while securing the adequate accuracy of the solutions.

4.2 Numerical simulations of turbulent flow in helically coiled pipes

The results of numerical simulations of flow in helically coiled pipes are presented. Turbulent flow generated and validated in the previous section has been utilized as an inlet velocity profile to study the coupled effect of curvature and torsion on the stability of the flow.

4.2.1 Instantaneous velocity and vortex structures

Figure 4.10 shows the volume rendering of velocity magnitude after the flow was developed for all the cases. The results indicate the stabilization of turbulent flow towards the outlet for all cases. Changing the number of coils (i, ii, iii) did not lead significant changes in the velocity. Although increasing the number of coils (iii) resulted in more stable flow near the outlet, pipe length was the longest in this case. Changing the radius resulted in difference in the velocity. Decreasing the radius (iv) led to the partial increase in the velocity at the first inner curve while increasing the radius (v) showed comprehensible stabilization towards the outlet. For all cases, a long wavy structure with a relatively lower velocity magnitude can be observed after a few turns of the coil. Along the inner wall, lower velocity magnitude was also observed.

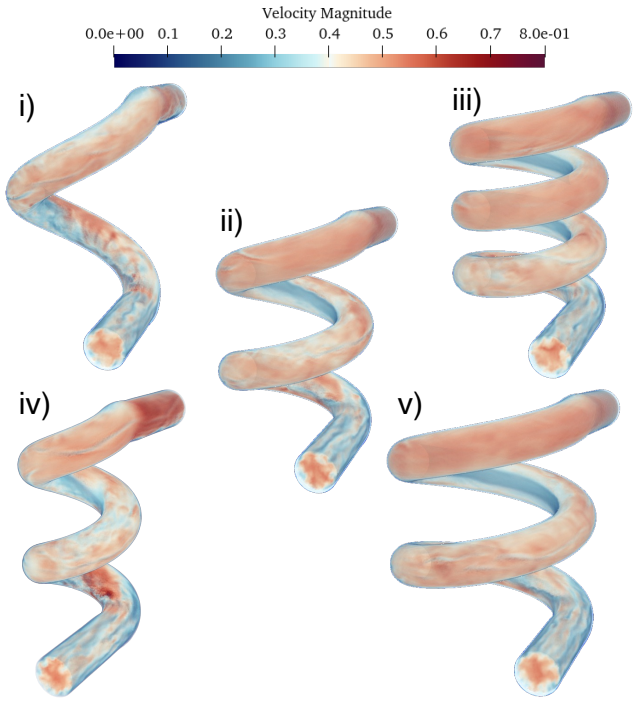

Figure 4.10: Volume rendering of the instantaneous velocity magnitude after the flow was developed. Stabilization of the flow towards the outlet can be observed. Changing the radius (iv, v) showed larger difference than changing the number of coils (i, iii). Height was kept constant.

Figure 4.11 shows iso-surfaces of the Q-criterion $Q = 0.5$ based on the instantaneous velocity after the flow was developed. With the selected criteria $Q = 0.5$, this figures shows the local destabilization and the global stabilization of the flow. An increase in the vortex structures at the first curve can be observed for all cases, which indicates the local destabilization. After the first turn, flows were generally stabilized as there were fewer vortex structures. However, vortex structures were still observed near the upper and lower walls. This visualization indicates the stronger stabilization along the inner and outer wall compared to the upper or lower wall. As the centrifugal force originating from the curvature affects the flow, the stronger stabilization along the inner and the outer wall is understandable. Qualitatively, changes in the number of coils (i, ii, iii) did not lead to the difference in the vortex structures. On the other hand, changes in the radius of the coil (ii, iv, v) showed the difference in the density of vortex structures. In the case of the decreased coil radius (iv), where the curvature and torsion are the highest, vortex structures were spatially spread in the coil. In the case of the increased coil radius (v), vortex structures were narrower and confined to the smaller region of the pipe.

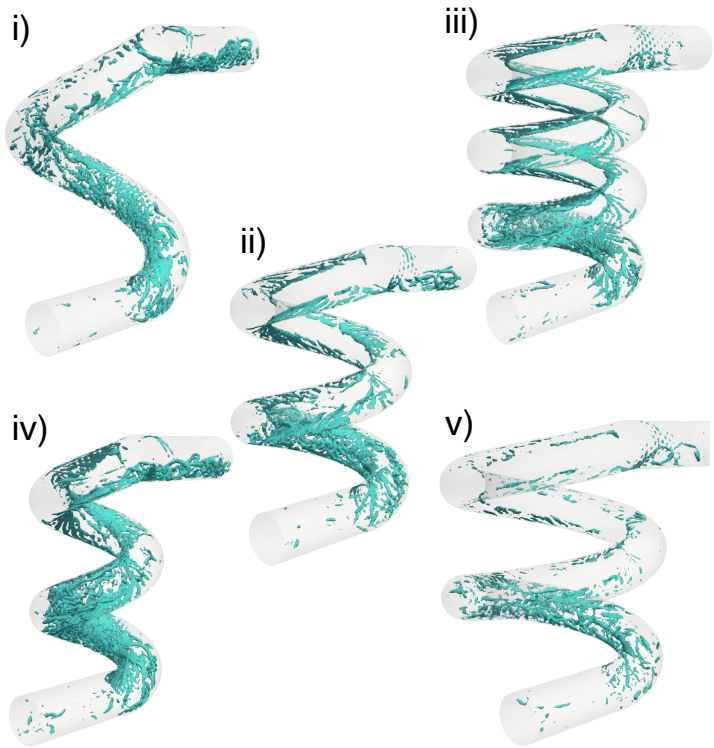

Figure 4.11: Iso-surface of Q-criterion = 0.5 based on the instantaneous velocity is shown to examine vortex structures. A local increase in the vortex structure can be observed at the first curve. Towards the outlet, there are fewer vortex structures indicating the stabilization of the flow, especially along the inner and outer wall.

4.2.2 Mean velocity

We will now consider the time-averaged flow field. First, we start analyzing the velocity distribution on the cross-section where the flow was almost stabilized. This means that we chose the location near the outlet. The mean velocity distribution is plotted in Figure 4.12 and the default case (ii) is chosen as a representative case. Here, $r/R = -1$ is at the inner (horizontal) or lower (vertical) wall and $r/R = 1$ at the outer (horizontal) or upper (vertical) wall. From the plot with horizontal cut (——), it can be seen that the velocity magnitude is low at the inner wall and increases almost linearly towards the outer wall. On the other hand, the plot with a vertical cut (- - -) shows a large velocity magnitude near the lower and upper wall with an almost constant velocity profile near the centerline of the pipe. This may explain the vortex structures observed along the lower or upper wall.

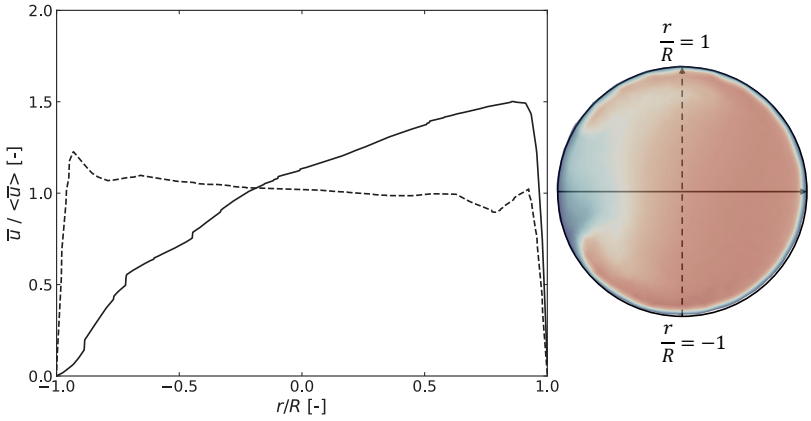

Figure 4.12: Mean velocity magnitude along the horizontal cut (——) with $r/R = -1$ being at the inner wall and $r/R = 1$ at the outer wall, and along the vertical cut (- - -) with $r/R = -1$ at the lower wall and $r/R = 1$ at the upper wall. The plot is made from the cross-sectional slice corresponds near the outlet. The default case (ii) is selected as a representative case. Higher velocity is colored with red.

To further analyze the transition of the flow inside the coil, Figure 4.13 shows the cross-sectional view of the mean velocity cut perpendicular to the centerline. This figure qualitatively shows how fast the flow was stabilized in each case. Each figure showing the mean velocity is positioned in a way that the left side of the figure is ensured to be the inner wall and the right side of the figure is the outer wall. Based on the difference in the mean velocity on the two consecutive cross-sections, the magnitude of the secondary flow may be estimated. For example, when both the curvature and the torsion were decreased (v) from the default case (ii), the mean velocity showed the convergence to the specific shape after the first turn (slice 3 or higher). On the other hand, when both the curvature and the torsion were increased (iv), the mean velocity constantly changed over all slices.

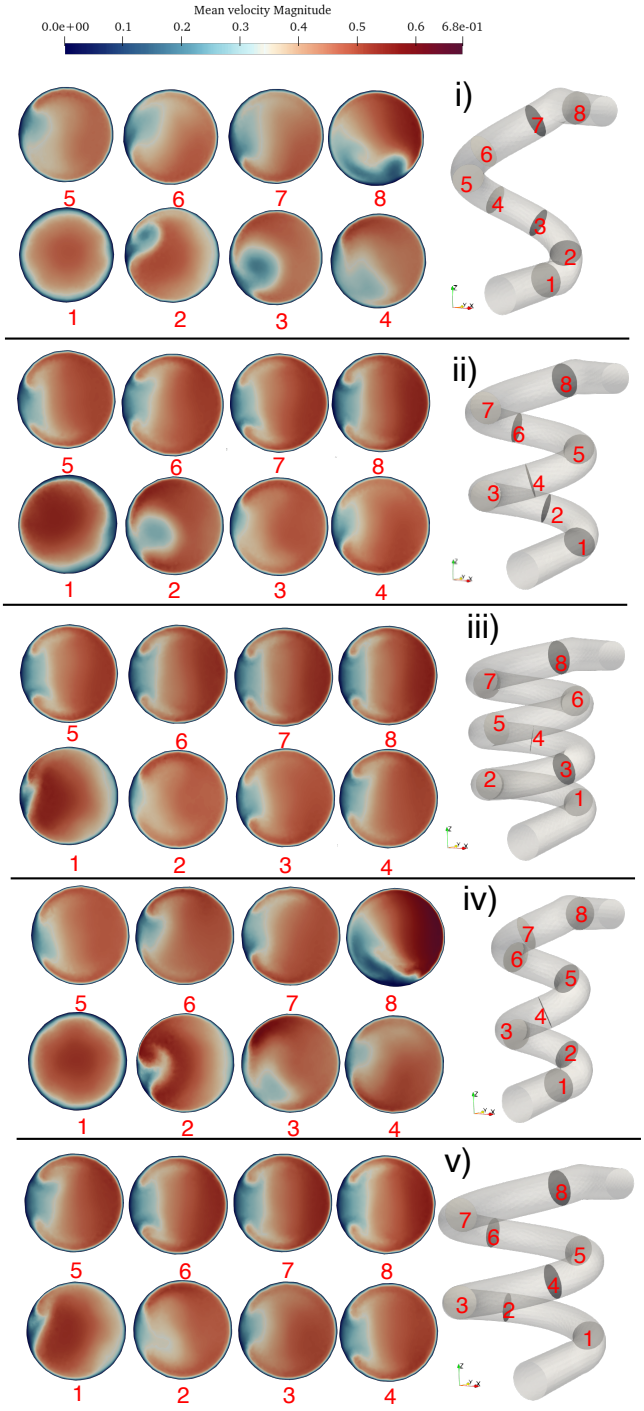

Figure 4.13: Cross-sectional view of the mean velocity cut perpendicular to the centerline of the coiled pipes. The left side of the figure is the inner wall and the right side is the outer wall. From the changes in the mean velocity between two consecutive slices, the magnitude of the flow on the cross-section (the secondary flow) may be estimated. Case iv) exhibits strong secondary flow until the outlet while case v) shows convergence of the flow.

4.2.3 Mean pressure

Figure 4.14 shows the time-averaged pressure distribution on the cross-section of the coil. Here, the increased number of coils (iii) was selected as a representative. Plots on the right side show the pressure cut along the vertical line of the cross-section with $r = -1$ and $r = 1$ at the inner and outer wall, respectively. The pressure was low at the inner wall and almost linearly increased towards the outer wall. At the inlet (slice1) and the outlet (slice 7), the pressure gradient is relatively low compared to the inside coil. Although the absolute value of the pressure changed towards the outlet, the magnitude of the pressure gradient was similar inside the coil. As the pressure gradient acts as a force, this means that the turbulent flow in helically coiled pipes constantly experiences the force from the outer to the inner wall. At the same time, the centrifugal force also acts to push the fluid towards the outer wall. This imbalance between those two forces creates the secondary flow on the cross-section of the coil.

Although the results from other cases are not shown here, the pressure distribution shared some characteristics. However, the difference in the magnitude of the pressure gradient was observed when the radius of the coil was changed. Increasing and decreasing the radius of the coil, respectively resulted in a smaller and larger pressure gradient. Changing the number of coils did not lead to the noticeable difference in the pressure gradient. Pressure gradient was almost constant along the vertical direction.

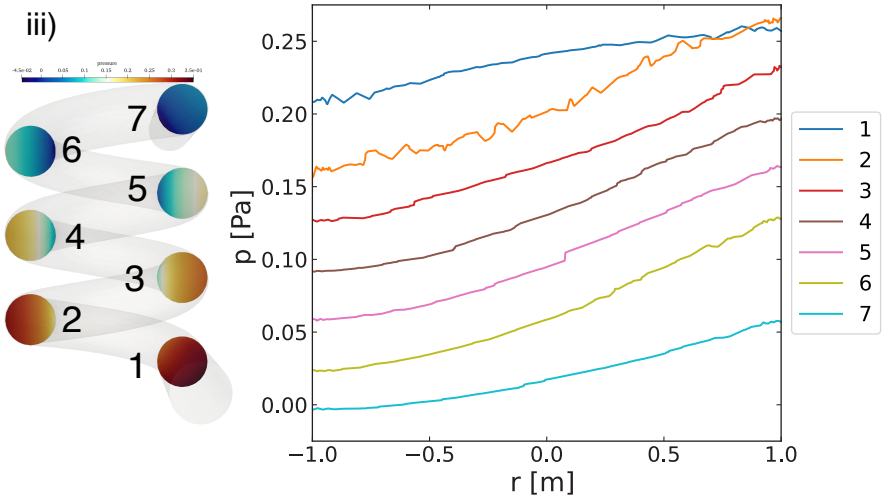

Figure 4.14: Left : Cross-sectional view of time-averaged pressure distributions. Higher pressure is colored with red. The increased number of coils (iii) was selected. Right : Plots show the pressure distribution along the horizontal cut of each slice with $r = -1$ and $r = 1$ at the inner and outer wall, respectively. The numbering in the plots corresponds to the numbering in the left figure. Near the inlet (1) and outlet (7), pressure gradient was relatively low. Inside the coil ($2 \sim 6$), pressure gradient was developed with lower and higher pressure at the inner and outer wall, respectively. Pressure was almost constant along the vertical direction.

To investigate the dominant factor determining the magnitude of the pressure gradient, Figure 4.15 is prepared. Pressure gradient ($\Delta p = p_{max} - p_{min}$) across the vertical cut from all slices were averaged for all five cases and plotted against the curvature and torsion of each coil. Although the results are from only five cases, higher curvature (κ) seems to be associated with a higher pressure difference. The correlation between torsion (τ) and the pressure gradient is unclear. As the centrifugal force is a function of the curvature, it is understandable that curvature is a dominant factor determining the pressure gradient of the helically coiled pipes.

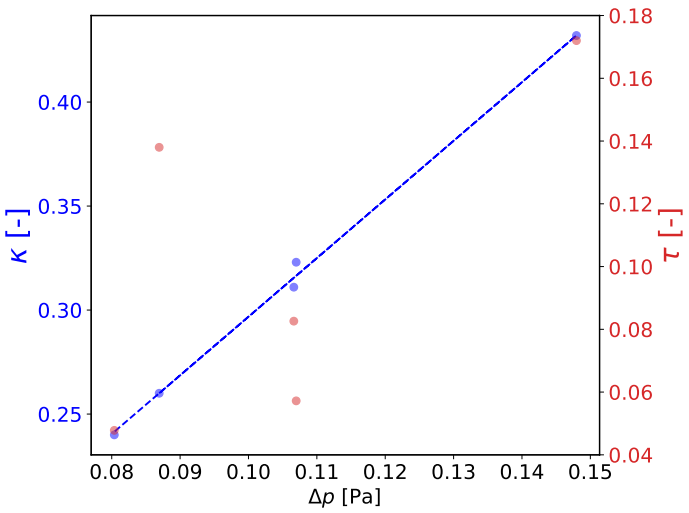

Figure 4.15: Scatter plot of the pressure difference along the horizontal cut of cross-section of coils. The left and right y-axis represents the curvature (κ) and the torsion (τ), respectively. The pressure difference is averaged over slices in each coil. The blue dashed line is added to highlight the correlation between the pressure difference and the curvature.

4.2.4 Cross-sectional analysis of the turbulent kinetic energy

To quantitatively assess the instability of the flow and the speed of the transition of the flow, we have computed the turbulent kinetic energy (TKE). TKE is defined as follows where u_i' is the fluctuating components of the instantaneous velocity, and overline denotes the time averaging.

$$k = \frac{1}{2}\left(\overline{(u_x')^2} + \overline{(u_y')^2} + \overline{(u_z')^2}\right) \tag{4.5}$$

First, we will present the results from the default case (ii) and cases with decreased (i) or increased (iii) number of coils. Figure 4.16 shows cross-sectional view of the TKE. The plot shown on the middle and right represents the TKE along the horizontal and vertical cut, respectively. The x-axis in the plot is defined in the same way as in Figure 4.12. This result again confirms the destabilization at the first turn of the coil (slice 2) and stabilization of the flow towards the outlet.

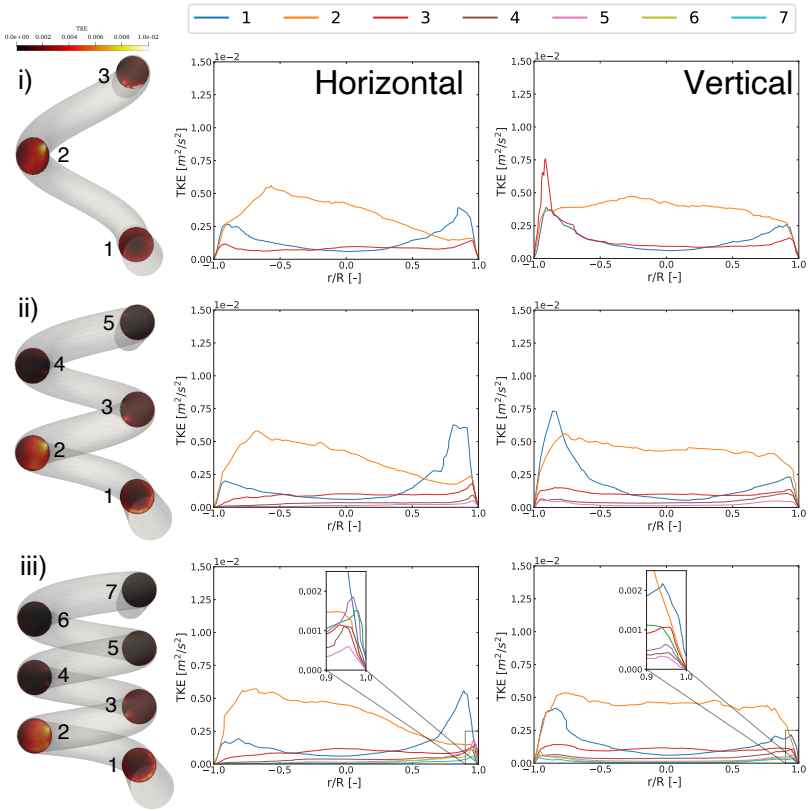

Figure 4.16: Left : Cross-sectional view of the TKE with different number of coils. Higher TKE is colored with a brighter red. Two plots on the right side show the TKE along the horizontal (left) and the vertical (right) cut. $r/R = -1$ is the inner (horizontal) or lower (vertical) wall and $r/R = 1$ is the outer (horizontal) or upper (vertical) wall. Numbering in the plots corresponds to the numbering in the left figure. This figure indicates the shift of the maximum TKE location inside the coil.

Although there is a strong shift in the TKE distribution from the inlet to the outlet, changing the number of the coils (i, ii, iii) did not lead to the significant difference in the distribution and the evolution of the TKE. Thus, we will focus on examining the shift of TKE distribution inside the coil.

First, we start analyzing the TKE along the horizontal cut (middle plot). All plots near the inlet (slice 1) showed the largest value near the outer wall ($r \approx 0.9$) and also the local peak near the inner wall ($r \approx -0.9$). The maximum TKE was larger at the outer wall possibly due to the centrifugal force. Near the inlet, small curvature induced the centrifugal force, which pushed the fluid with higher velocity towards the outer wall. This might have introduced some disturbance to the velocity. Plots from the first turn (slice 2) showed an increase in the TKE compared to the inlet for most of regions except the outer wall. The maximum value was located at around $r = -0.75$ for all cases. This means that the most turbulent region shifted from the outer to the inner wall during the

first turn. Plots from the second turn or above (slice 3 or above) are similar with a small peak near the outer wall. This indicates another shift of the maximum TKE from the inner to the outer wall with a decrease in the overall value. At the outlet, the TKE was decreased and flattened for all cases.

Plots along the vertical cut (right plot) also exhibited the transition of the TKE distribution in the coil. Plots from the inlet (slice 1) had two large peaks at lower ($r = -0.9$) and upper ($r = 0.9$) wall with upper wall being the maximum. This is again considered to be caused by the centrifugal force as the coil is curved upwards. Similar to the plots along the horizontal cut, an increase of the TKE was observed in the first turn (slice 2). All cases had almost uniform TKE distribution. Then, plots from the second turn or higher (slices 3 or higher) generally showed a similar TKE distribution between each case with two large peaks near the lower and upper wall. The decreased number of coils (i) has a high TKE at the outlet along the lower wall, but this is due to the surface roughness introduced by the flow extension at the outlet.

Next, the results from changing the radius of the coil are shown in Figure 4.17. Contrary to changing the number of the coils, large difference in the TKE distribution can be observed. Especially in the first turn (slice 2), the decreased (iv) and increased (v) radius of the coil showed very different TKE distribution. However, at the outlet (slice 5), both cases exhibited the large reduction in the value even though the decreased radius of the coil (iv) has shorter length of the coil. This indicates the fast stabilization of the decreased radius of coil (iv).

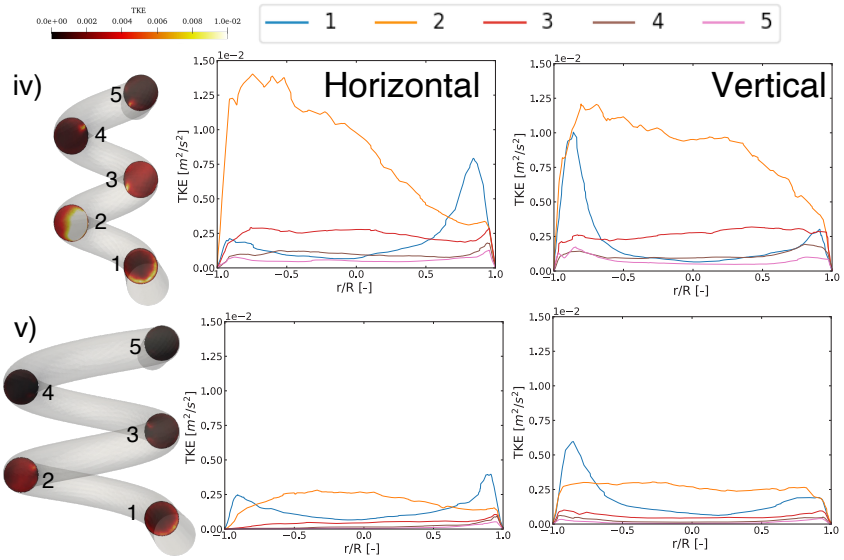

Figure 4.17: Left : Cross-sectional view of the TKE for the decreased (iv) and increased (v) radius of the coil. See Figure 4.16 for the explanation of the plot. Plots on the right indicates large difference in the TKE distribution when the radius of the coil was changed. However, stabilization of the flow was still observed in both cases.

4.2.5 Turbulent kinetic energy along the centerline

Although we observed the global stabilization and the local destabilization of turbulent flow, cross-sectional analysis is not sufficient to measure the speed of transition towards the outlet. Therefore, we have measured the TKE as a function of the distance from the inlet. However, as cross-sectional analysis revealed, the TKE differed significantly depending on the point on the cross-section. Therefore, we measured the surface average TKE from a number of slices cut perpendicular to the centerline. In this way, we can estimate the averaged changes of the TKE along the centerline. As a comparison, we also conducted the simulation of a straight pipe with length $L = 45r$ where r is the pipe radius. Fully developed turbulent flow was used as an inlet velocity and the pressure was set to 0 at the outlet.

First, Figure 4.16 shows the TKE where the number of coils was changed. TKE is normalized by its value at the inlet. Arc length used as the x-axis is the distance of the centerline point from the inlet. Although an increase in the TKE near the outlet was observed from all cases, this is due to the surface roughness introduced by the flow extensions. To recap, we increased the number of coils from case i) to iii), which resulted in the increase in the curvature and the decrease in the torsion. It is known that higher curvature and torsion are respectively suppress and enhance turbulence [28, 55]. However, the effects of simultaneously changing curvature and torsion were unknown. As the case iii), which had the highest curvature and the lowest torsion, stabilized faster than the other two cases, this result shows the agreement with the previous studies even when these two parameters were modified simultaneously.

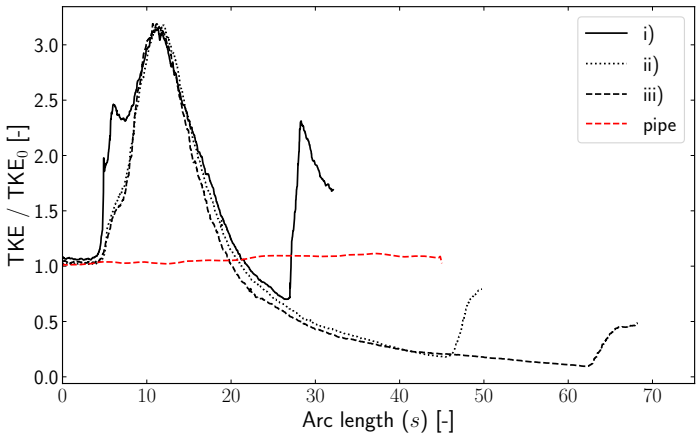

Figure 4.18: TKE as a function of the distance from the inlet with different number of coils. The decreased (i) and the increased (iii) number of coils respectively stabilized the flow slower and faster compared to the default case (ii). The results confirm the suppression of turbulence by the higher curvature and the lower torsion as the most stable case (iii) has the highest curvature and the lowest torsion.

Next, the TKE with different radius of the coil is shown in Figure 4.19. In this case, the maximum TKE differed significantly between three cases. Case iv) showed the highest TKE but the stabilization after the maximum was also the fastest. Case v) had the lowest TKE but the stabilization was relatively slow judging from the smoothness of the curve. Since the case iv) had the highest curvature and the torsion while the case v) had the lowest, the increase in the TKE might be associated with the higher torsion while the faster stabilization could be explained by the higher curvature. Yet, it is difficult to determine the separate the effect of each parameter.

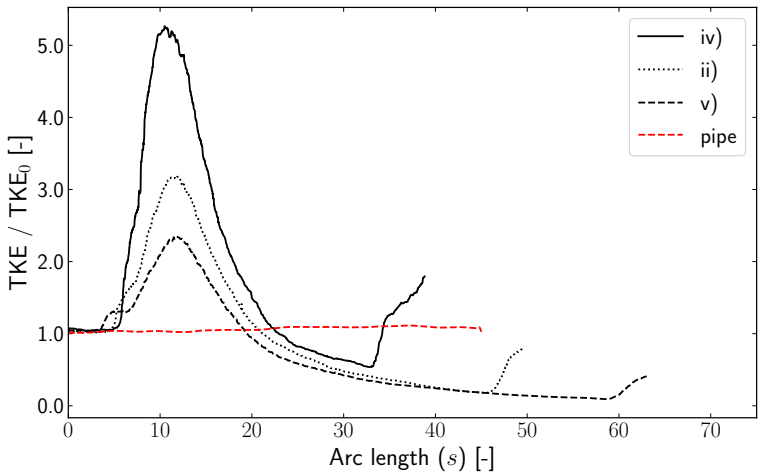

Figure 4.19: Surface averaged TKE with different radius of the coil. Increasing the radius (iv) resulted in the sharp transition of the flow while decreasing (v) led to the smoother stabilization. This result may show faster stabilization with the higher curvature and the enhancement of turbulence by the higher torsion. Case iv) had the highest curvature and the torsion.

To sum up, as a result of changing the number of coils (i, iii), we observed that higher curvature and lower torsion are correlated with the faster stabilization of the flow. The results from changing the radius of the coil (iv, v) showed the increase in the TKE by the higher torsion and the faster stabilization by the higher curvature. Curvature alone is known to suppress the turbulence [32, 55] and torsion alone is known to enhance the turbulence [28]. However, our simulations showed the complex evolution of turbulence when these two parameters are changed simultaneously. This highlights the coupled effect of curvature and torsion and both parameters need to be carefully taken into account when analyzing the flow in helically coiled pipes or similar geometry, e.g, blood vessels.

4.2.6 Dean vortices as a stabilization factor

Dean vortices were observed in all the cases based on the mean velocity. Though the location of the Dean vortices and structures are different in each case, they were observed after the first turn of the coil. Here we will focus on the two cases, the decreased number of coils (i) and radius of the coil (iv), to illustrate the development of Dean vortices. Figure 4.20 shows the mean secondary flow on the two selected cross-sections from the two cases. The secondary flow is measured by removing components of the velocity vectors normal to the cross-sectional surface. We employed line integral convolution technique [8] to create the figure shown on the top side of Figure 4.20. Open-source scientific visualization tool Paraview [1] was used. Before (slice 2) and after (slice 4) the maximum TKE location are selected to show the difference of vortices. As can be seen, Dean vortices consisting of two counter-rotating vortices were observed before the maximum TKE (slice 2). Typically, cores of the Dean vortices are located near the centerline of the curved pipe [14]. However, the centers of the two vortices were moved towards the inner wall in helically coiled pipes. A single vortex rotating clockwise was observed after the maximum TKE (slice4). The formation of the Dean vortices before the maximum TKE suggests the correlation between enhanced flow instability and the Dean vortices.

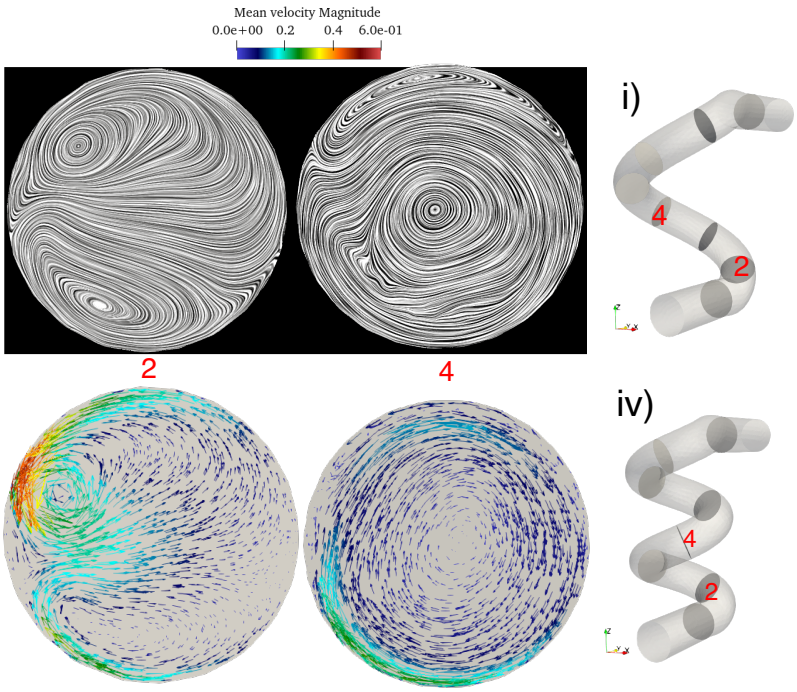

Figure 4.20: Visualization of Dean vortices using the line integral convolution (top) and the vector plot of the mean secondary flow (bottom). Slice 2 and slice 4 were located before and after the maximum TKE, respectively. This suggests the correlation between the increased TKE and the presence of the Dean vortices.

Dean vortices are known to introduce instability to the flow [46] in the case of laminar flow as a consequence of induced rotations. This is one of the reasons why helically coiled pipes are used as heat exchangers. The increase of heat and mass transfer can be achieved without internal installations [42]. In our simulations, all of the Dean vortices were observed in the first turn, which is also the location of maximum TKE. Thus, even in the case of turbulent flow, Dean vortices may further introduce the fluctuations to the velocity.

Figure 4.21 is a representative visualization of streamlines of the mean velocity indicating how Dean vortices were formed. There were rotations of the flow near the inner wall. When the fluid entered the curve, those with higher velocity were pushed and impinged to the outer wall. Consequently, they moved along the outer, upper, and inner walls with rotating motions due to the impingement. During this rotation, the axial velocity is weakened while the radial and azimuthal velocities are strengthened. At the same time, a pressure gradient from the outer to the inner wall was developed. Therefore, the imbalance between the centrifugal and the pressure gradient evolved, and strong rotations were created near the inner wall. This visualization may explain the transition of the maximum TKE location from the outer to the inner wall observed from the cross-sectional analysis.

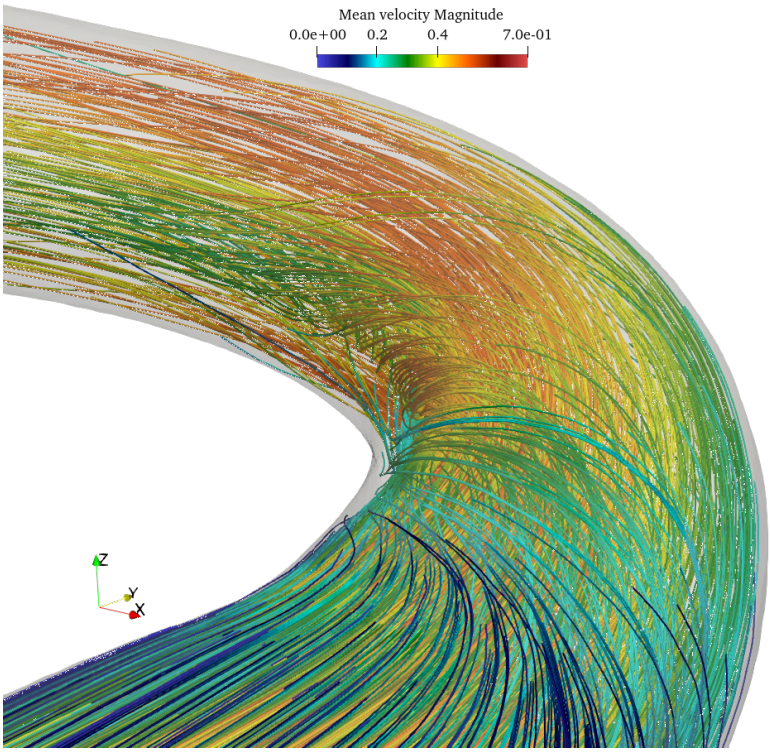

Figure 4.21: Streamlines of the mean velocity near the first turn of the helically coiled pipe. Along the inner wall, strong rotations can be observed indicating the formation of the Dean vortices. The rotations are considered to be formed by the centrifugal force and the adverse pressure gradient.

We also observed the global stabilization of the turbulent flow through the helically coiled pipe. Kuhnen et al. [44] conducted a numerical simulation that showed stabilization of turbulent flow in a pipe. In the numerical simulation, they increased the perturbations of fully developed turbulent flow and observed relaminarization of the flow. They described *"when increasing the turbulent fluctuations well beyond their usual levels ($k > 2.5$), surprisingly the highly turbulent flow almost immediately collapses and returns to laminar"*. They also conducted two experiments to further investigate this effect. In the first experiment, four counter-rotating rotors are placed in the cross-section of the pipe and quickly stir a fully turbulent pipe flow ($Re = 3,500$). In the second experiment, turbulent flow ($Re = 3,100$) is disturbed by injecting fluid through 25 small holes in the pipe wall. They wrote *"Each injected jet creates a pair of counter-rotating vortices, intensifying the eddying motion beyond the levels of ordinary turbulence."*. In both experiments, the quick disappearance of turbulent flow similar to the numerical simulation was observed. Figure 4.22 shows the result from the first experiment. In the case of helically coiled pipes, Dean vortices that arise originally from the centrifugal force can be considered to act the same way as rotors or vortices generated by the jet did in their experiments. In other words, Dean vortices introduced the local destabilization that eventually led to the stabilization of the turbulence. The surface averaged TKE was amplified by 2.34 (case v) up to 5.26 (case iv) times. According to Kuhnen et al.'s criteria ($k > 2.5$), this might have been enough perturbations to stabilize the turbulent flow. As the bulk of dissipation happens within the smallest eddies, Dean vortices inside the coils may break up the larger eddies into smaller eddies which results in the decrease of the TKE by promoting the dissipation.

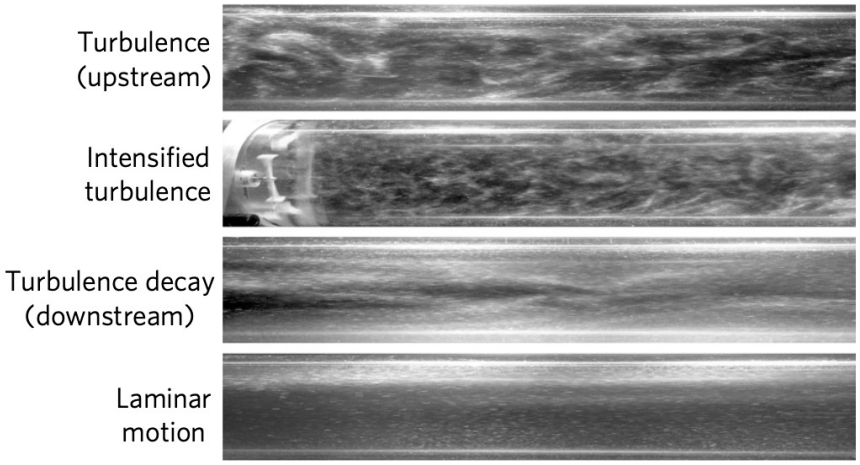

Figure 4.22: Relaminarization of turbulence adapted from Kuhnen etl al. [44] with the following caption. "Fully turbulent flow (top panel) at Re = 3,100 is perturbed by vigorously stirring the fluid with four rotors. The more strongly turbulent flow (second panel) eventually relaminarizes as it proceeds downstream (third and fourth panel). "

The vortices at the location of maximum TKE were visualized based on the instantaneous velocity. Figure 4.23 shows the vortex structures at two different time step. Contrary to the Dean vortices observed before the maximum TKE, several smaller vortices were observed changing their size and location. As the TKE was quickly decreased after its maximum, these small vortices might be dissipated and led to the decrease of the TKE. Therefore, the process of the local destabilization and the global stabilization can be summarized as follows.

1. When the flow entered helically coiled pipes, Dean vortices were first formed. This is a direct consequence of the imbalance between the centrifugal force, the adverse pressure gradient.

2. Dean vortices intensified the rotations and the dissipation, and thus the increase of the TKE was locally observed.

3. Smaller eddies introduced by the Dean vortices dissipated and the TKE quickly decreased.

4. As a result, fluctuating components of the velocity were reduced and the turbulent flow was stabilized.

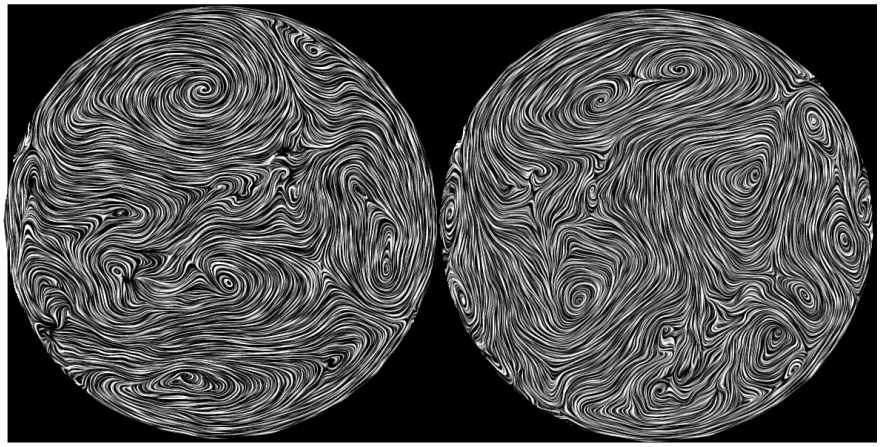

Figure 4.23: Visualization of vortices on the cross-section where the TKE was maximum for all the cases. The default case (ii) is used as a representative case, and two different time step was randomly picked, showing the presence of several small vortices. A sharp decrease of the TKE after its maximum indicates the strong dissipation by small vortices.

4.2.7 Limitations and summary

Our simulations have limitations, and we will address some in this subsection. First, we have used the turbulent flow in a straight pipe as an inlet velocity profile. The validation process showed that the mean axial velocity and its fluctuations were over-estimated while radial and azimuthal velocity fluctuations were under-estimated. Therefore, our results of turbulent flow in helically coiled pipes are also not fully resolved. Although our simulations could be expanded to resolve all the spatial and temporal resolutions, computational time would

be enormous as the DNS of a straight pipe also needs to be carried out with our method. For this reason, large-eddy simulations might be an adequate next step to further understanding the flow in helically coiled pipes.

Second, since we used the data set from the straight pipe as an inlet velocity profile, the straight section was added to the coiled pipes to make mapping velocity easier. However, a higher curvature was introduced near the inlet and outlet as a result. Although this should not affect the observed stabilization of the turbulent flow, it would have been ideal if the transition from straight to curved part was smoother than our case. Generally speaking, this could be pointed out as a shortcoming of the FEniCS as the meshing is not part of the FEniCS except for some simple geometry like a rectangle or circle. On the other hand, commercial software such as ANSYS [4] are equipped with the CAD meshing tool and have higher flexibility when it comes to creating 3D meshes. We have used Gmsh [23] and VMTK [58], both of which do not currently export the mesh file that is compatible with FEniCS. Therefore, we had to spend some time developing code to convert the mesh file one to another.

Third, we have created five meshes in total while the height was fixed. This method of changing the geometry resulted in variations in pipe length. We admit that keeping the pipe length would have made the comparison easier. However, given that Hüttl and Friedrich [32] employed one curvature ($\kappa = 0.1$) and two torsion ($\tau = 0.11, 0.165$), our results with curvature ($\kappa = 0.240 \sim 0.432$) and torsion ($\tau = 0.0478 \sim 0.172$) cover the wide ranges of parameters that might help expand the investigations of flow in the helically coiled pipe.

Finally, we have conducted the simulations with only one Reynolds number. We would need another set of simulations and validations of turbulent pipe flow if we were to perform the simulations at a higher Reynolds number. Simply this requires even more computational time. It is not clear from our simulations if similar phenomena would be observed at a higher Reynolds number.

To summarize, numerical simulations of turbulent flow in helically coiled pipes have been conducted. To the best of our knowledge, this is the first numerical study that addressed the stabilization of turbulent flow in helically coiled pipes. We also observed the local destabilization of the flow. Dean vortices were formed near the location of maximum TKE. Our simulations suggested that the Dean vortices may create smaller vortices, enhance the dissipation and thus stabilize the turbulent flow. By changing the number of coils, we observed that the combination of the higher curvature and the lower torsion stabilized the flow quickly, which agrees with the previous studies [28, 32, 55]. On the other hand, changing the radius of the coil showed a significant increase in the TKE with the highest curvature and torsion, indicating the destabilization by the higher torsion.

4.3 Numerical simulations of blood flow in the internal carotid artery

In the previous section, we investigated turbulent flow in helically coiled pipes that have some common geometrical characteristics as internal carotid arteries (ICA). In this section, we will present the results of the numerical simulation of blood flow in patient-specific ICA. The objective of this chapter is to investigate flow instability in the ICA. In previous studies that examined the initiation or rupture of cerebral aneurysms, hemodynamic indices, such as wall shear stress (WSS), are often focused on [36, 51, 77] as they act directly on the vascular wall. Therefore, we have also computed such hemodynamic indices. Yet, we will only focus on the the flow structures in the ICA in this thesis (see Appendix C for the computed hemodynamics indices). This is largely motivated by the previous work by Bergersen (2016) and Kjeldsberg (2018) in their master thesis, both of which studied the hemodynamic indices at the apex of bifurcation. They performed objective manipulations of the geometrical parameters, such as peak curvature, area variation, and bend angle. As these parameters are statistically shown to be correlated with the presence of the aneurysms, WSS should also change if it is the cause of the aneurysms. However, they found no correlation between time-averaged WSS and these parameters, concluding WSS could not explain the aneurysm formation. Instead, they found flow instabilities to exhibit a noticeable difference when the geometries were modified. Therefore, we speculate that flow instabilities might be correlated with the initiation of aneurysms and aim to contribute to understanding flow structures in the ICA.

4.3.1 Instantaneous velocity and vortex structures

Figure 4.24 shows velocity magnitudes measured over one cardiac cycle at selected probe points. The numbering shown on the right side of each plot corresponds to the number indicated inside patient-specific geometries. The lowest number is located near the inlet, and the number increases towards the outlet. It is clear from the plots that flow patterns can vary significantly between cases. P0207 shows slight velocity fluctuations throughout the entire domain, while all the other cases show quite significant fluctuations of the velocity magnitude downstream of the ICA. Flow instability can be observed at the peak of the acceleration phase (called *systole*), was amplified right after that, and disappeared during the de-acceleration phase (called *diastole*). Generally, when flow instabilities were observed, it was formed in the carotid siphon, an S-shaped part of ICA, and persisted even after the bifurcation. By simulating the turbulent flow in helically coiled pipes, we observed the increase in the velocity fluctuations at the first curve. This may explain why flow instabilities tend to be formed in the carotid siphon, as they are typically characterized by a series of bends and twists [61]. It is also worth mentioning that the probes were located along the centerline of the ICA. However, our simulations in the helically coiled pipes suggested that the peak of the TKE was usually located either along the inner or outer wall. Therefore, even stronger flow instabilities might be present along the vessel walls.

Figure 4.25 shows iso-surface of Q-criterion $Q = 0.5$ at the peak of cardiac cycle. The general trend is that the vortex structures are formed at the carotid

siphon. For example, P0250 explicitly reveals the presence of vortex structures after the curve. One common characteristic of all cases is that vortex structures are observed near the bifurcation. Since the most of the cerebral aneurysms ($> 80\%$) are formed at the bifurcation [80], the presence of flow instabilities near the bifurcation might be stimuli for the aneurysm initiation.

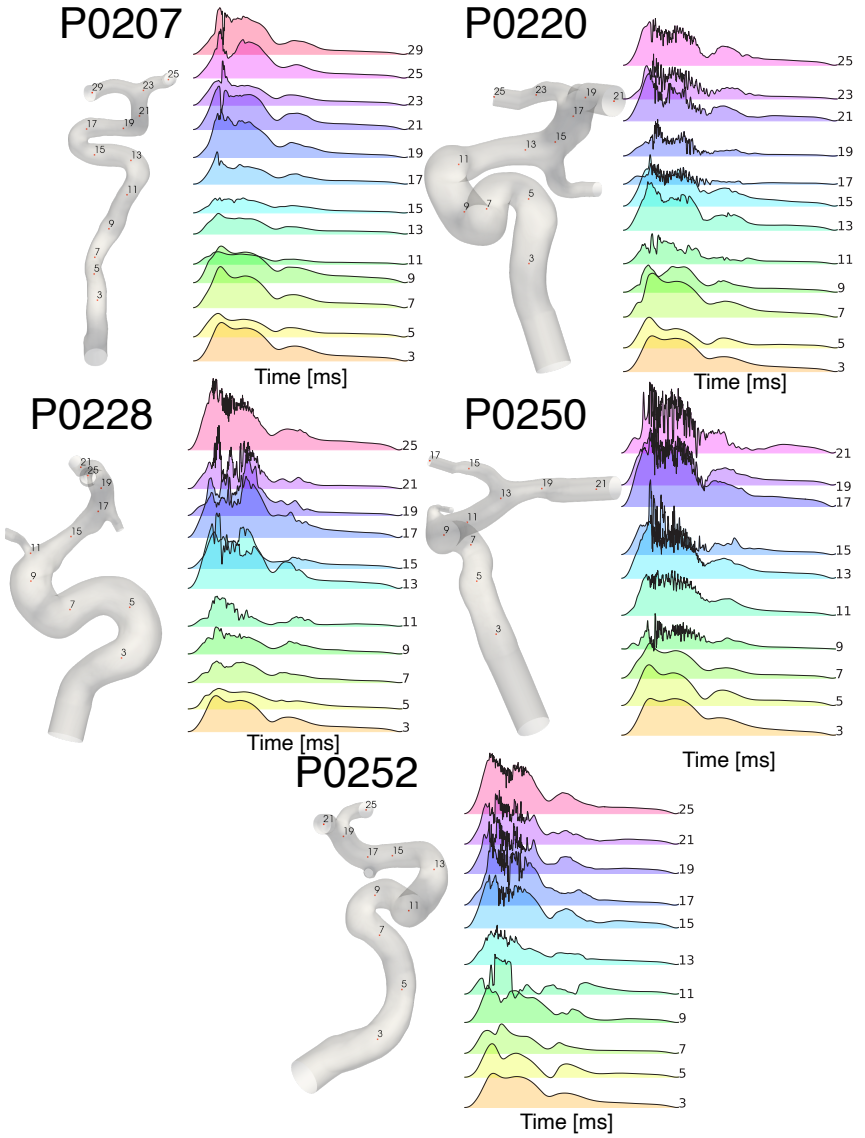

Figure 4.24: Velocity magnitude over one cardiac cycle was measured at probe points. Velocity magnitude was normalized by the cycle-average. The lowest number shown on the right side of the plot corresponds to the inlet. P0207 exhibited a stable velocity profile, while the other cases manifested strong fluctuations of the velocity at the peak of the cardiac cycle.

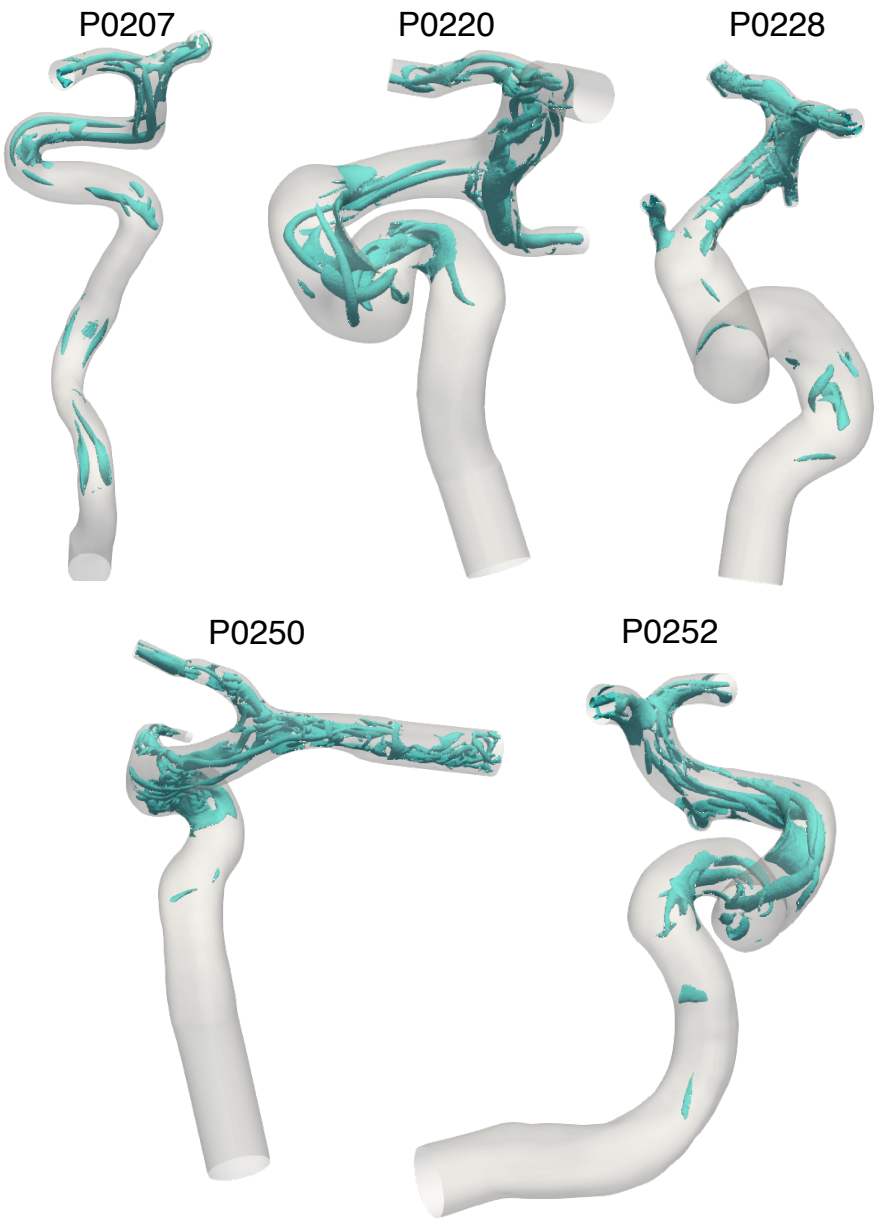

Figure 4.25: Iso-surface of Q-criterion $Q = 0.5$ representing vortex structures. Time was selected at the peak of the cardiac cycle. For cases P0220, P250, and P0252, vortex structures first appeared in the carotid siphon, an S-shaped bend in the ICA. P0207 exhibited the vortex structure at the first curve of the carotid siphon, but it disappeared quickly and was re-introduced at the second curve. For case P0228, vortex structure was observed right before the bifurcation, where a strong area reduction existed.

4.3.2 Curvature, torsion, and flow instability

We have investigated the correlation between curvature, torsion, and flow instability in helically coiled pipes. Changing the number of coils revealed that the combination of the highest curvature and the lowest torsion stabilized the flow the fastest. On the other hand, by changing the radius of coils, it was observed that the combination of the highest curvature and the highest torsion produced the most turbulent flow but also stabilized the flow quickly. This highlighted the coupled effects of the curvature and torsion on flow instability. Although our results were inconclusive, we showed the significant changes of the flow pattern when both the curvature and torsion were modified at the same time. When it comes to the ICA, curvature is often of great interest as the ICA is characterized as having several bends. For example, a statistical study by Lauric et al. [45] showed the correlations between the sidewall aneurysms and the higher curvature. Klis et al. [41] also found the statistical link between the ICA aneurysm and higher curvature. However, there have been few studies about the torsion of the ICA. This is due to the fact that the torsion is harder to measure with high accuracy than the curvature. As we saw in the equation (2.12) and (2.13), curvature requires the second derivative of the curve while torsion requires the third, which makes the measurement of the torsion challenging. Yet, the effect of the torsion can not be neglected. To investigate the coupled effects of curvature and torsion, torsion parameter β may be utilized. Hayamizu et al. [28] experimentally studied the critical Reynolds number in helically coiled pipes using the torsion parameter $\beta = \tau/(2\kappa)^{1/2}$. They found that the flow became unstable as the torsion parameter increased. Since their focus was the transition from laminar flow to turbulence, we did not use this parameter for our simulations of turbulent flow in helically coiled pipes. However, in the case of the ICA, this torsion parameter might be beneficial to account for the effect of the torsion.

Figure 4.26 shows the curvature (κ), the torsion (τ), and the torsion parameter (β) of the centerline of the each patient. Abscissas (s) here represents the distance from the inlet. We used the VMTK script, vmtkcenterlinegeometry, to compute the curvature and torsion. Note that Laplace filtering was applied to smooth the outputs as VMTK uses a simple finite difference scheme along the line to compute the derivatives, resulting in the noise. Both curvature and torsion constantly change along the centerline with wave-like form, representing the bends. P0207 case shows very high curvature $\kappa = 0.467$ mm^{-1} at abscissas $s = 52.4$ mm, which is inside the carotid siphon. The torsion at the same location is $\tau = -0.00465$ mm^{-1}, which is a relatively low value compared to the mean $\tau = -0.0142$ mm^{-1}. Although the Reynolds number employed for P0207 was the lowest among the five cases, this combination of the high curvature and the low torsion might be associated with the flow stability in the P0207. Such a combination can also be observed for P0220 at $s \approx 20$, but this is not inside the carotid siphon. Although the torsion parameter was computed as shown in Figure 4.26 (c), the correlation with flow instability is unclear even though several peaks can be observed in some cases. The investigation with larger cohort might be necessary to examine the effects of the torsion parameter. As the curvature and torsion are not constant in the ICA, and other factors may affect the flow patterns, the results from the helically coiled pipe may not

be directly applicable. Still, the analyses of the curvature and torsion may shed light on the formation of flow instability.

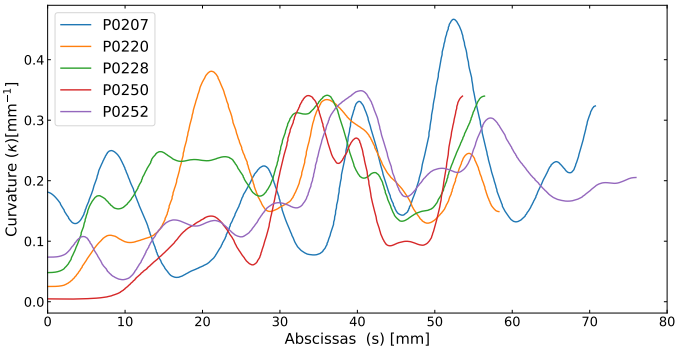

(a) Curvature

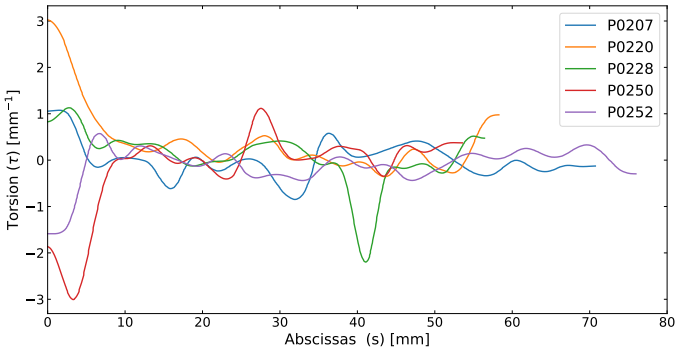

(b) Torsion

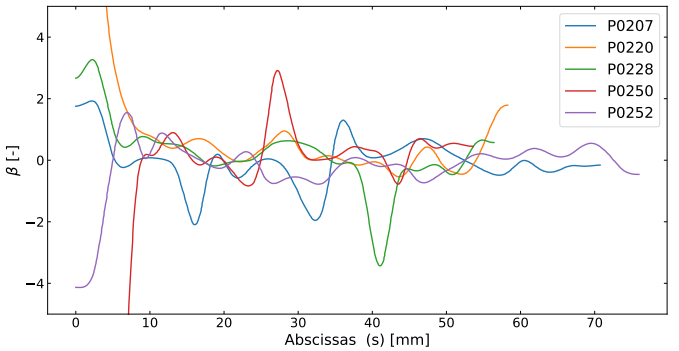

(c) Torsion parameter

Figure 4.26: (a) Curvature, (b) torsion, and (c) torsion parameter of the centerline for each patient. Abscissas represents the distance from the inlet. The centerline is taken from the inlet to the bifurcation, neglecting the branches.

4.3.3 Dean vortices near the bifurcation

Dean vortices have been experimentally found in the pulsatile flow in 90° bends pipe at high Reynolds number [35]. However, whether Dean vortices could be formed in the ICA is unclear. Typically Dean number is used to determine the formation of the Dean vortices [69], but such an analysis is restricted to the simple geometry and can not be applied to the ICA. As the Dean number is the production of the Reynolds number and the square root of the curvature, either a higher Reynolds number or higher curvature is required for the Dean vortices to appear. An experimental study by Takeuchi and Karino [70] reported *"the flow proximal to the terminal bifurcation of the ICA ... was highly disturbed by the presence of a strong helicoidal flow, which was generated first within the carotid siphon and then reinforced at the last bend (the fifth bend) of the carotid siphon."*, but the presence of Dean vortices has not been described or visualized. Given the mean diameter of the ICA is 4.77 ± 0.78mm [43], visualizations of the secondary flow on the cross-section might have been difficult for the experiments. Here, we chose P0207, P0250 as representative cases and examined if Dean vortices were formed near the bifurcation. Note P0207 showed little fluctuations of the velocity while P0250 showed strong fluctuations. Figure 4.27 and 4.28 show the secondary flow on the four selected cross-sections of the ICA at the peak systole. Although our visualization is a qualitative analysis and highly dependent on the subjective choice of visualization parameters, the formation of the Dean vortices was observed in the carotid siphon (slice 2, 3) for P0207 and near the bifurcation (slice 4) for P0250.

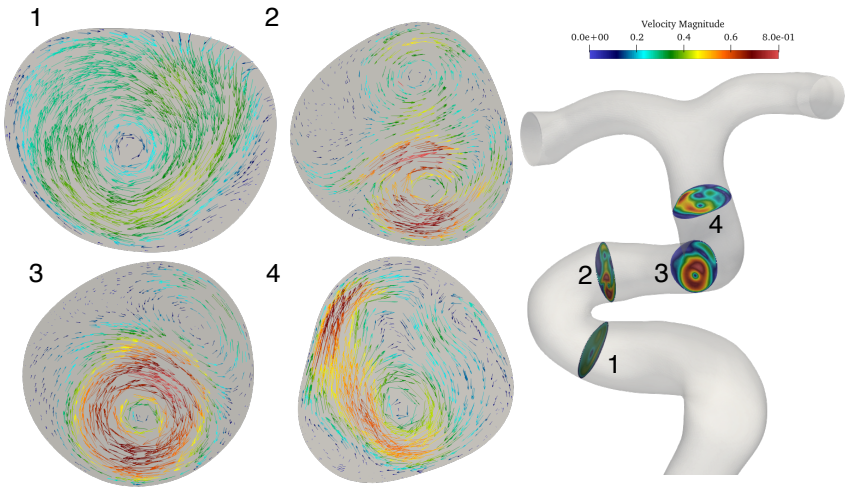

Figure 4.27: P0207 : Formation of single vortex is observed slice 1. Dean vortices are observed inside the carotid siphon (slice 2, 3), an S-shaped bend.

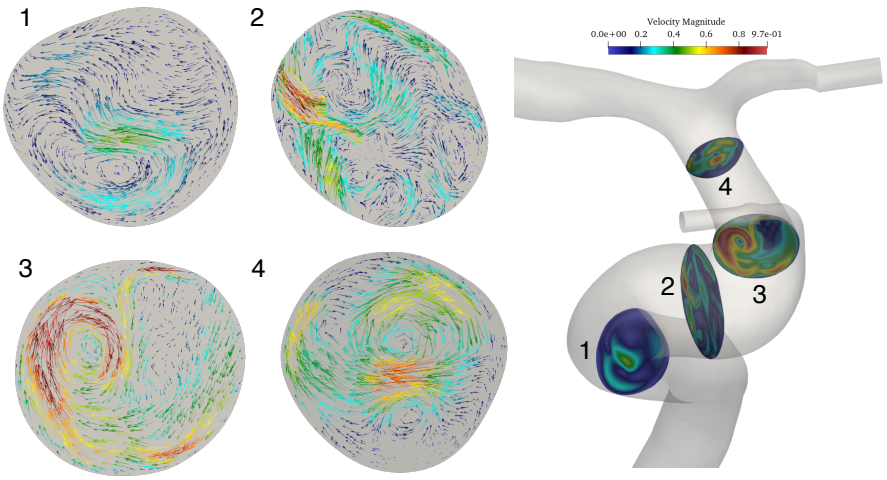

Figure 4.28: P0250 : Single vortex was observed on lower side of 1. Flow in the carotid siphon (slice 2) is highly disturbed. Single vortex is observed on the left side of slice 3 and formation of Dean-type vortices may be observed near the bifurcation (slice4).

Although our results from simulating turbulent flow in helically coiled pipes suggested the enhancement of the dissipation by the Dean vortices and the stabilization of the flow. A local increase in the turbulent kinetic energy was also observed. Whether Dean vortices inside ICA may stabilize or destabilize the flow can not be determined from our simulations. Still, the location of Dean vortices may impact the flow instability at the bifurcation. For example, the P0207 case showed the formation of Dean vortices from slice 2, which is relatively far from the bifurcation, while Dean vortices were first observed from slice 4 in P0250, which is closer to the bifurcation. Because flow instability was almost exclusively formed at the carotid siphon, the formation of the Dean vortices inside the carotid siphon may be able to suppress the fluctuations of the flow before distinct flow instability was developed. On the contrary, if the secondary flow is disturbed and no Dean vortices are generated in the carotid siphon, the formation of the Dean vortices may happen near the bifurcation. This can further increase the flow instability as the vessel near the bifurcation is less curved compared to the carotid siphon.

The temporal evolution of the Dean vortices was also investigated. Figure 4.29 shows the formation of Dean vortices at a different time step. The location of the cross-section was chosen near the bifurcation from P0250. Before the peak systole, a single vortex was observed (I), and Dean vortices were formed right after that (II). Before the second peak, one of the Dean vortices became small (III) and re-amplified at another location (IV). After that, a single vortex was observed (V, VI). Although this oscillatory behavior of vortices is likely to be caused by the pulsatile base flow, oscillations of the Dean vortices were observed in turbulent flow through 90° bend pipes [9, 31]. This low-frequency oscillatory phenomenon is termed as *swirl switching* or *vortex core switching* and is known to cause fatigue in piping systems. The effects of this swirl switching

can not be determined from our simulations, but the induced low-frequency flow may be associated with the flow instability at the apex of bifurcation.

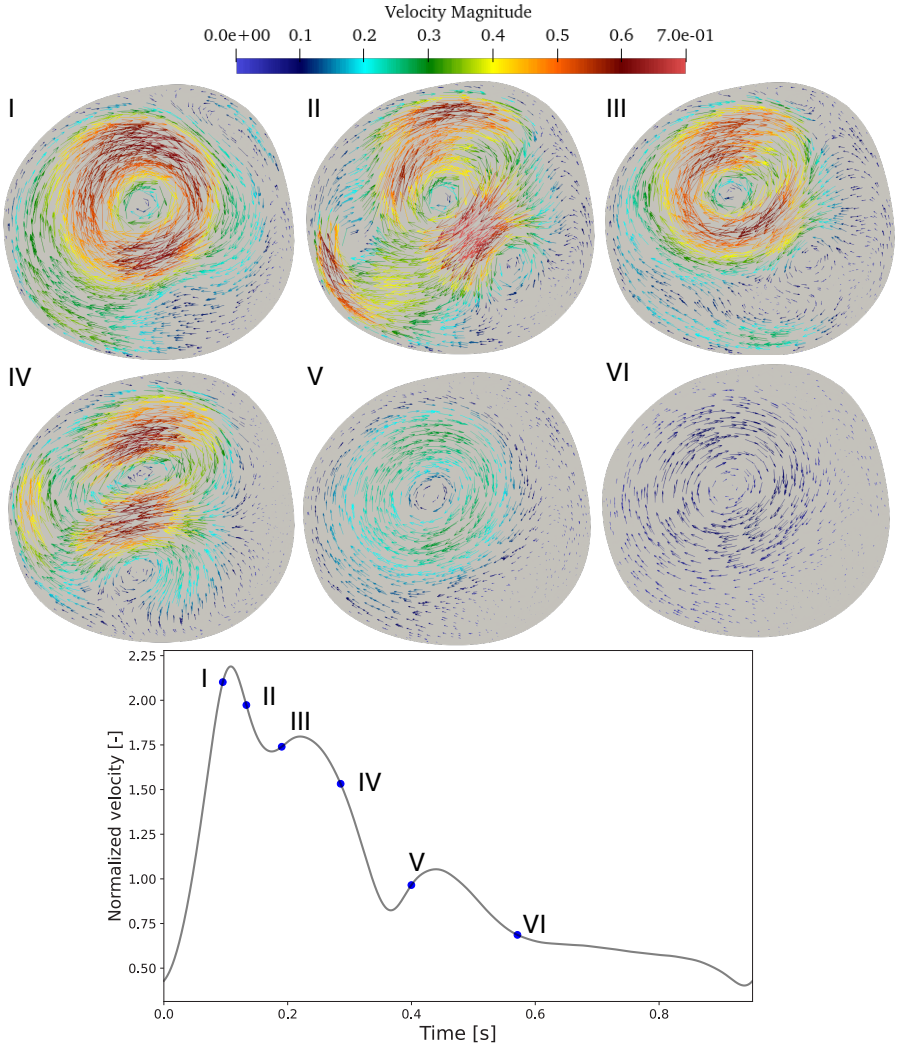

Figure 4.29: Temporal evolution of the Dean vortices near the bifurcation of P0250, which exhibited flow instability. Roman numeral indicates the time of each slice and corresponds to the plot below. Right after the two peaks (II, IV), the formation of Dean vortices was observed that might be associated with enhanced flow instability.

4.3.4 Limitations and summary

Here, we will address the assumptions we made and the limitations of this study. Although blood is a non-Newtonian fluid, we assumed blood to be a Newtonian fluid. As blood viscosity decreases with shear stress (known as *shear thinning*), the assumption of Newtonian fluid may overestimate the WSS [83]. However, Khan et al. [37] showed that the effects of non-Newtonian

rheology is of 'second-order' and negligible when high temporal and spatial resolution are employed. As our simulations can be classified as high-resolution, we assume the effects of non-Newtonian rheology would be negligible. We also made assumption of rigid walls. Although Fluid-structure interaction (FSI) have been recently used [5, 71] and such an analysis is definitely a prospective step, FSI solvers are still computationally much more expensive than fluid solver such as *Oasis*. In addition, measurements of wall thickness is in general still challenging and thus using FSI solver with a patient-specific geometry is both numerically and clinically difficult. Lastly, we used the waveform from Hoi et al. [30] for the inlet boundary condition. Patient-specific flow rates might change the results but is rarely available.

Our study is qualitative and not quantitative. The detection of the Dean vortices was done by the visualization technique. Depending on the choice of parameters, the results might be different. In addition, the number of patient-specific geometry was limited. A larger cohort study is necessary to further assess the correlation between flow instability and the initiation of cerebral aneurysms.

To summarize, numerical simulations of blood flow in the patient-specific geometry of the ICA have been conducted. In some of the cases, we detected the 'turbulent-like' flow developed in the carotid siphon, which contains several acute bends. In addition, Dean vortices were observed in some of the patients. Although the result is inconclusive, the formation of the Dean vortices might have negligible effects on the flow instability of the ICA.

Chapter 5

Conclusion and Future work

5.1 Conclusion

The main objective of this thesis was to investigate the turbulent flow in helically coiled pipes. Of particular interest was the stabilization and destabilization effects of helically coiled pipes and how they may be associated with the flow patterns in the internal carotid artery. As a first step, we performed validation of *Oasis* against published DNS [18] by simulating turbulent flow at $Re_\tau = 180$ in a straight pipe. Our mesh refinement test showed convergence towards DNS data by increasing the spatial resolution. At the same time, we have managed to acquire our data set of turbulent flow. These data sets were used to simulate the turbulent flow in helically coiled pipes. Numerical simulations of turbulent flow in helically coiled pipes with five different geometries were subsequently carried out. The results showed the local destabilization and the global stabilization both of which may be associated with the presence of Dean vortices. To the author's knowledge, this is the first numerical report on the stabilization of turbulent flow in helically coiled pipes. Modifying the number of coils did not lead to significant changes in the flow field, while modifying the radius of coils resulted in a large difference in turbulence. Although the effects of changing curvature and torsion were already investigated in separation [28, 32, 55], we examined the consequence of chaining two parameters simultaneously. When the curvature was increased and the torsion was decreased, the maximum TKE was constant but the faster stabilization of the flow was observed. On the other hand, when the curvature and the torsion were increased simultaneously, the maximum TKE increased, but also a faster stabilization of the flow was observed. This indicates the complex coupled effects of the curvature and torsion on the flow when both of them are modified at the same time.

Finally, we have performed numerical simulations of blood flow in the internal carotid artery (ICA) using ten healthy patient-specific geometries, although five cases were shown. In a patient with the highest curvature in the carotid siphon with relatively low torsion, we did not observe flow instability. Even though there are several factors affecting the flow patterns in the ICA, the combination of the high curvature and the low torsion may suppress flow instability in the ICA. This agrees with the results from helically coiled pipes. However, as curvature and torsion are not constant in the ICA, it is unclear how much the analysis of curvature and torsion could explain the flow patterns in the

ICA. We have measured the torsion parameter [28, 85], which accounts for both curvature and torsion, but a clear correlation with flow instability was not observed. To our best knowledge, Dean vortices inside the ICA were observed for the first time. The location of the Dean vortices may be associated with flow instability that appears near the bifurcation. During the cardiac cycle, the low-oscillatory behaviour of the Dean vortices were observed. Further analysis of the Dean vortices inside the ICA would be necessary to assess the effects of the Dean vortices on flow instability.

5.2 Future work

For the turbulent flow in helically coiled pipes, to the author's knowledge, there has been no study about swirl-switching phenomena in the helically coiled pipes. Hufnagel et al. [31] used proper orthogonal decomposition to detect several modes of the oscillations, and a similar approach could be applied to helically coiled pipes. We investigated the correlation between the Dean vortices and the flow instability in the ICA. To detect the Dean vortices, we relied on the visualization technique, but visualization is only qualitative analysis. We attempted frequency analysis using Fourier-transform but did not observe a frequency peak that might have been associated with the presence of the Dean vortices. Recently, Natarajan et al. [54] used spectrograms to visualize the frequency structures and such a method might be useful.

Appendices

Appendix A

Investigation of the numerical boundary layer

Oasis has been previously verified by Mortensen and Valen-Sendstad [52]. In their published work, two dimensional Taylor-Green flow is used to conduct the rate of convergence test and achieved the expected accuracy. For this reason, another set of verification test has not been conducted in this thesis since the solver chosen for the verification is the same one that will be used later in this thesis. However, we conducted series of numerical experiments to further address the difference of the solvers implemented in *Oasis*. The purpose of this study is to investigate the numerical boundary layer and the gained knowledge from this experiment may be subsequently used to improve *Oasis* in the future.

In the review paper on the projection methods written by Guermond et al. [26], they performed two numerical tests to assess the influence of the numerical boundary layer on the pressure error. They employed *method of manufactured solutions* (MMS), which is a robust way of verification of the codes [60]. The basic idea of MMS starts from choosing an analytical solution. Then, the analytical solution is used to construct the source term in the governing equation that can produce the analytical solution. In this fashion, the numerical solution can be compared against the known analytical solution to estimate the numerical error in the code.

The first numerical test was conducted with spectral approximation to investigate the numerical boundary layer with standard and rotational form of the pressure correction algorithm. The result is illustrated in Figure A.1. The analytical solution takes the following form.

$$\begin{aligned} \mathrm{u}(x,y,t) &= \pi \sin t \left(\sin 2\pi y \sin^2 \pi x, -\sin 2\pi x \sin^2 \pi y\right) \\ \mathrm{p}(x,y,t) &= \sin t \cos \pi x \sin \pi y. \end{aligned} \tag{A.1}$$

They observed the disappearance of the numerical boundary layer with rotational form but the large peaks of the error at the corners of the domain were still observed.

The next numerical test was conducted with P2/P1 finite elements to further assess the influence of the smoothness of the domain boundary on the accuracy

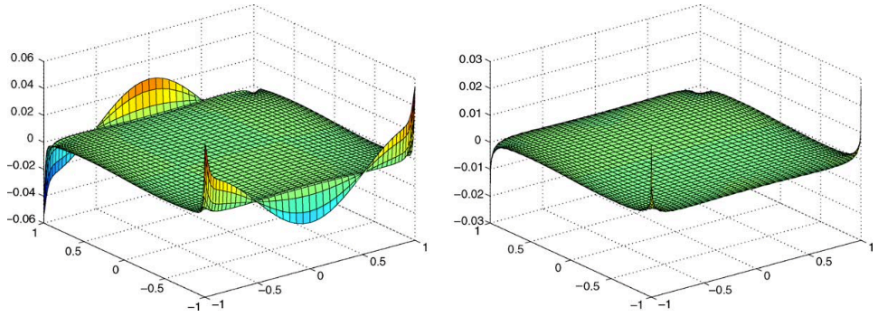

Fig. 1. Pressure error field at time $t = 1$ in a square: (left) standard form; (right) rotational form.

Figure A.1: Pressure error field with standard (left) and rotational (right) form of the pressure correction algorithm. Adapted from *An overview of projection methods for incompressible flows* by J.L. Guermond et al. [26]

of rotational pressure correction method. They used the following analytical solution

$$\begin{aligned} u &= (sin(\pi(x+t))sin(\pi(y+t)), cos(\pi(x+t))cos(\pi(y+t))) \\ p &= sin(\pi(x-y+t)) \end{aligned} \tag{A.2}$$

in the square domain $[0,1]^2$ and in the circular domain (x,y); $\sqrt{x^2+y^2} \leq 0.5$. Note the original equation in the review paper was missing π. The result is shown in Figure A.2. There are two large peaks of the error with square domain while there is no such peaks with circular domain.

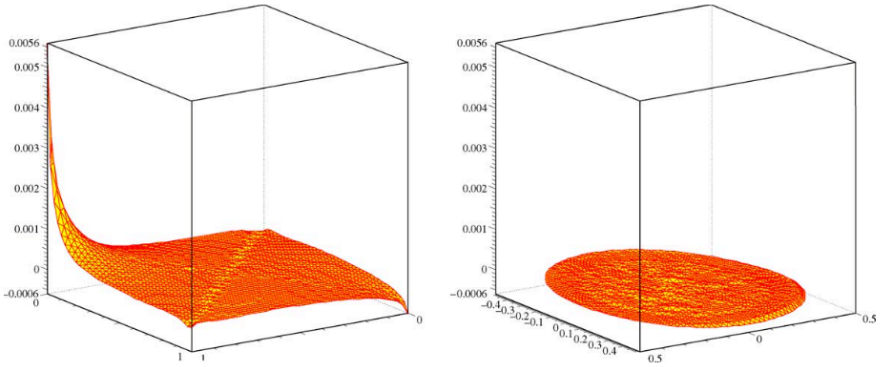

Fig. 3. Error field on pressure in a rectangular domain (left) and on a circular domain (right).

Figure A.2: Pressure error field with rotational form of the pressure correction algorithm in the square and circle domain. Adapted from *An overview of projection methods for incompressible flows* by J.L. Guermond et al. [26]

We conducted series of numerical tests by means of MMS. Our numerical tests also used P2/P1 finite element for the equation (A.2) and computed the pressure

error field with three schemes. First scheme is the non-incremental pressure correction scheme, the second is the incremental pressure correction scheme, and the last is the incremental pressure correction scheme in rotational form. Each scheme will be hereafter referred as Chorin, IPCS, BDFPC respectively following the naming from *Oasis*. The mesh-size was $h = 1/40$ and $\Delta t = 0.00625$ with $T = 1$ meaning total computational time step was 160.

Figure A.3 shows the pressure error field at $T = 1$. The results from both Chorin scheme and IPCS scheme (Figure A.3 (a) and (b)) show the numerical boundary layer, but the error is reduced with IPCS scheme. The result from BDFPC (rotational form) shown in Figure A.3 (c) shows the disappearance of the numerical boundary layer with two large peaks of errors at the corner of the domain, which is similar to the results presented by Guermond et al. in Figure A.2. It is likely that these two large peaks of the error come from the fact that the there are only one node point at the corner of the domain due to its meshing. Figure A.3 (d) shows the error in a circular domain with no obvious peaks of the error, which is also consistent to the results presented by Guermond et al. in Figure A.2.

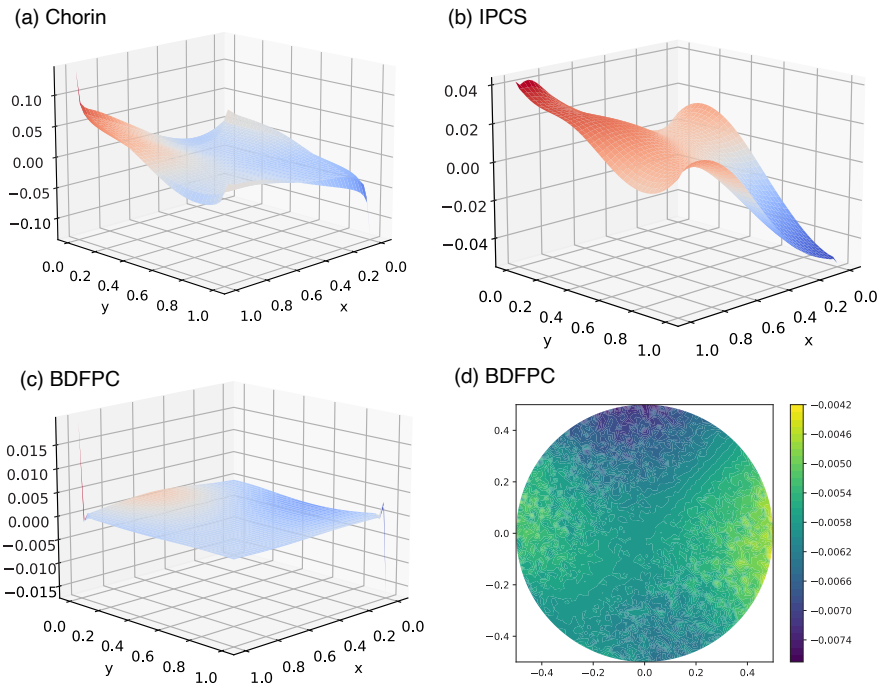

Figure A.3: Pressure error field with (a) Chorin scheme (b) IPCS scheme (c) BDFPC scheme in a rectangular domain (d) BDFPC scheme in a circular domain.

To summarize, several numerical schemes built inside *Oasis* have been tested against analytical solutions. Each scheme manifested the characteristics of its own that are mathematically proven and shown by Guermond et al. [26]. In this way, the implemented numerical scheme in *Oasis* are proven to be accurate.

Appendix B

Derivation of the turbulent kinetic energy equation

As the first step to derive the turbulence kinetic energy equation, we will make an attempt to derive the equation for fluctuating velocity $\boldsymbol{u}'$. This can be done by subtracting equation Reynolds averaged Navier-Stokes equations from instantaneous momentum equation.

$$\frac{\partial \boldsymbol{u}-\overline{\boldsymbol{u}}}{\partial t}+(\boldsymbol{u}\cdot\nabla)\boldsymbol{u}-(\overline{\boldsymbol{u}}\cdot\nabla)\overline{\boldsymbol{u}}=-\frac{1}{\rho}\nabla(p-\bar{p})+\nu\nabla^2(\boldsymbol{u}-\overline{\boldsymbol{u}})+\frac{\partial\overline{u_i'u_j'}}{\partial x_j}+\boldsymbol{f}-\overline{\boldsymbol{f}}$$

$$\Rightarrow \frac{\partial \boldsymbol{u}'}{\partial t}+(\boldsymbol{u}\cdot\nabla)\boldsymbol{u}-(\overline{\boldsymbol{u}}\cdot\nabla)\overline{\boldsymbol{u}}=-\frac{1}{\rho}\nabla p'+\nu\nabla^2\boldsymbol{u}'+\frac{\partial\overline{u_i'u_j'}}{\partial x_j}+\boldsymbol{f}' \tag{B.1}$$

The convection terms can be computed as

$$\begin{aligned}(\boldsymbol{u}\cdot\nabla)\boldsymbol{u}-(\overline{\boldsymbol{u}}\cdot\nabla)\overline{\boldsymbol{u}}&=\left((\overline{\boldsymbol{u}}+\boldsymbol{u}')\cdot\nabla\right)(\overline{\boldsymbol{u}}+\boldsymbol{u}')-(\overline{\boldsymbol{u}}\cdot\nabla)\overline{\boldsymbol{u}}\\&=(\overline{\boldsymbol{u}}\cdot\nabla)\boldsymbol{u}'+(\boldsymbol{u}'\cdot\nabla)(\overline{\boldsymbol{u}}+\boldsymbol{u}')\end{aligned} \tag{B.2}$$

Thus, inserting (B.2) into (B.1) gives

$$\frac{\partial \boldsymbol{u}'}{\partial t}+(\overline{\boldsymbol{u}}\cdot\nabla)\boldsymbol{u}'=-\frac{1}{\rho}\nabla p'+\nu\nabla^2\boldsymbol{u}'-(\boldsymbol{u}'\cdot\nabla)(\overline{\boldsymbol{u}}+\boldsymbol{u}')+\frac{\partial\overline{u_i'u_j'}}{\partial x_j}+\boldsymbol{f}' \tag{B.3}$$

We can also write equation (B.3) in terms of index notation.

$$\frac{\partial u_i'}{\partial t}+\bar{u}_j\frac{\partial u_i'}{\partial x_j}=-\frac{1}{\rho}\frac{\partial p'}{\partial x_i}+\nu\frac{\partial^2 u_i'}{\partial x_j\partial x_j}-u_j'\frac{\partial\bar{u}_i}{\partial x_j}-u_j'\frac{\partial u_i'}{\partial x_j}+\frac{\partial\overline{u_i'u_j'}}{\partial x_j}+f_i' \tag{B.4}$$

Here, recall that the turbulence kinetic energy is described as $k=0.5\overline{\boldsymbol{u}'\boldsymbol{u}'}=0.5\overline{u_i'u_i'}$ and the Reynolds stress is defined as $R_{ij}=\overline{u_i'u_j'}$. Thus it is easier to derive the Reynolds stress equation first and then take the trace of that to derive the turbulence kinetic energy. To do that, we will multiply the equation (B.4) by u_k' and then take the average of the entire equation. Here, we neglect the body force for the convenience.

$$\overline{u_k'\left(\frac{\partial u_i'}{\partial t}+\bar{u}_j\frac{\partial u_i'}{\partial x_j}=-\frac{1}{\rho}\frac{\partial p'}{\partial x_i}+\nu\frac{\partial^2 u_i'}{\partial x_j\partial x_j}-u_j'\frac{\partial\bar{u}_i}{\partial x_j}-u_j'\frac{\partial u_i'}{\partial x_j}+\frac{\partial\overline{u_i'u_j'}}{\partial x_j}\right)} \tag{B.5}$$

The last term on the right-hand side disappears and all the other terms can easily computed as

$$\overline{u'_k \frac{\partial u'_i}{\partial t}} + \bar{u}_j \overline{u'_k \frac{\partial u'_i}{\partial x_j}} = -\frac{1}{\rho} \overline{u'_k \frac{\partial p'}{\partial x_i}} + \overline{\nu u'_k \frac{\partial^2 u'_i}{\partial x_j \partial x_j}} - \overline{u'_k u'_j} \frac{\partial \bar{u}_i}{\partial x_j} - \overline{u'_k u'_j \frac{\partial u'_i}{\partial x_j}} \tag{B.6}$$

The indices i and k are interchangeable as they are free indices. Thus, we also have

$$\overline{u'_i \frac{\partial u'_k}{\partial t}} + \bar{u}_j \overline{u'_i \frac{\partial u'_k}{\partial x_j}} = -\frac{1}{\rho} \overline{u'_i \frac{\partial p'}{\partial x_k}} + \overline{\nu u'_i \frac{\partial^2 u'_k}{\partial x_j \partial x_j}} - \overline{u'_i u'_j} \frac{\partial \bar{u}_k}{\partial x_j} - \overline{u'_i u'_j \frac{\partial u'_k}{\partial x_j}} \tag{B.7}$$

Summing up the previous two equations and using the relationship,$\partial u'_i u'_k/\partial t = u'_i \partial u'_k/\partial t + u'_k \partial u'_i/\partial t$, we get

$$\begin{aligned} \frac{\partial \overline{u'_i u'_k}}{\partial t} + \bar{u}_j \frac{\partial \overline{u'_i u'_k}}{\partial x_j} = & -\frac{1}{\rho} \left(\overline{u'_i \frac{\partial p'}{\partial x_k}} + \overline{u'_k \frac{\partial p'}{\partial x_i}} \right) \\ & + \nu \left(\overline{u'_i \frac{\partial^2 u'_k}{\partial x_j \partial x_j}} + \overline{u'_k \frac{\partial^2 u'_i}{\partial x_j \partial x_j}} \right) \\ & - \overline{u'_i u'_j} \frac{\partial \bar{u}_k}{\partial x_j} - \overline{u'_k u'_j} \frac{\partial \bar{u}_i}{\partial x_j} \\ & - \overline{u'_i u'_j \frac{\partial u'_k}{\partial x_j} - u'_k u'_j \frac{\partial u'_i}{\partial x_j}} \end{aligned} \tag{B.8}$$

We can rearrange the first term of the right-hand side in the following way.

$$\begin{aligned} \overline{u'_i \frac{\partial p'}{\partial x_k}} + \overline{u'_k \frac{\partial p'}{\partial x_i}} &= \overline{p' \left(\frac{\partial u'_i}{\partial x_k} + \frac{\partial u'_k}{\partial x_i} \right)} + \frac{\partial}{\partial x_j} \left(\overline{p' u'_i} \delta_{kj} + \overline{p' u'_k} \delta_{ij} \right) \\ &= 2\overline{p' s'_{ik}} + \frac{\partial}{\partial x_j} \left(\overline{p' u'_i} \delta_{kj} + \overline{p' u'_k} \delta_{ij} \right) \end{aligned} \tag{B.9}$$

where

$$s'_{ij} = \frac{1}{2} \left(\frac{\partial u'_i}{\partial x_j} + \frac{\partial u'_j}{\partial x_i} \right) \tag{B.10}$$

The second term of the right-hand side can be rewritten as

$$u'_i \frac{\partial^2 u'_k}{\partial x_j \partial x_j} = \frac{\partial}{\partial x_j} \left(\frac{\partial u'_i u'_k}{\partial x_j} - u'_k \frac{\partial u'_i}{\partial x_j} \right) - \frac{\partial u'_i}{\partial x_j} \frac{\partial u'_k}{\partial x_j} \tag{B.11}$$

and

$$u'_k \frac{\partial^2 u'_i}{\partial x_j \partial x_j} = \frac{\partial}{\partial x_j} \left(u'_k \frac{\partial u'_i}{\partial x_j} \right) - \frac{\partial u'_i}{\partial x_j} \frac{\partial u'_k}{\partial x_j} \tag{B.12}$$

These two equations can be summed up to produce

$$u'_i \frac{\partial^2 u'_k}{\partial x_j \partial x_j} + u'_k \frac{\partial^2 u'_i}{\partial x_j \partial x_j} = \frac{\partial^2 u'_i u'_k}{\partial x_j \partial x_j} - 2 \frac{\partial u'_i}{\partial x_j} \frac{\partial u'_k}{\partial x_j} \tag{B.13}$$

Now, we are able to use all the simplifications above to rewrite equation (B.8) as follows.

$$\frac{\partial \overline{u_i' u_k'}}{\partial t} + \bar{u}_j \frac{\partial \overline{u_i' u_k'}}{\partial x_j} = -\frac{2\overline{p' s_{ik}'}}{\rho} - \frac{\partial}{\partial x_j}\left(\frac{1}{\rho}\left(\overline{p' u_i'}\delta_{kj} + \overline{p' u_k'}\delta_{ij}\right) + \overline{u_i' u_k' u_j'} - \nu \frac{\partial \overline{u_i' u_k'}}{\partial x_j}\right) - 2\nu \overline{\frac{\partial u_i'}{\partial x_j}\frac{\partial u_k'}{\partial x_j}} - \overline{u_i' u_j'}\frac{\partial \bar{u}_k}{\partial x_j} - \overline{u_k' u_j'}\frac{\partial \bar{u}_i}{\partial x_j} \tag{B.14}$$

This is the final form for the *Reynolds stress transport equation*. As it it stated before, an equation for the turbulent kinetic energy can be obtained by setting index k equals to i. Some terms will vanish due to continuity and symmetry.

$$\frac{\partial \overline{u_i' u_i'}}{\partial t} + \bar{u}_j \frac{\partial \overline{u_i' u_i'}}{\partial x_j} = -\frac{\partial}{\partial x_j}\left(\frac{2}{\rho}\overline{p' u_i'}\delta_{ij} + \overline{u_i' u_i' u_j'} - \nu \frac{\partial \overline{u_i' u_i'}}{\partial x_j}\right) - 2\nu \frac{\partial u_i'}{\partial x_j}\frac{\partial u_i'}{\partial x_j} - 2\overline{u_i' u_j'}\frac{\partial \bar{u}_i}{\partial x_j} \tag{B.15}$$

By inserting the definition of the turbulent kinetic energy, we get

$$\frac{\partial k}{\partial t} + \overline{u}_j \frac{\partial k}{\partial x_j} = -\frac{\partial}{\partial x_j}\left(\frac{1}{\rho}\overline{p' u_i'}\delta_{ij} + \frac{1}{2}\overline{u_i' u_i' u_j'} - 2\nu \overline{s_{ij}' u_i'}\right) - 2\nu \frac{\partial u_i'}{\partial x_j} s_{ij}' - \overline{u_i' u_j'}\frac{\partial \bar{u}_i}{\partial x_j} \tag{B.16}$$

The last term of the divergence terms(the first term of the rhs) can be rewritten as

$$\nu \frac{\partial^2 u_i' u_i'}{\partial x_j \partial x_j} = 4\nu \frac{\partial s_{ij}' u_i'}{\partial x_j} - 2\nu \frac{\partial u_i'}{\partial x_j}\frac{\partial u_j'}{\partial x_i} \tag{B.17}$$

Inserting this into (B.16) gives

$$\frac{\partial k}{\partial t} + \overline{u}_j \frac{\partial k}{\partial x_j} = -\frac{\partial}{\partial x_j}\left(\frac{1}{\rho}\overline{p' u_i'}\delta_{ij} + \frac{1}{2}\overline{u_i' u_i' u_j'} - 2\nu \overline{s_{ij}' u_i'}\right) - 2\nu \overline{\frac{\partial u_i'}{\partial x_j} s_{ij}'} - \overline{u_i' u_j'}\frac{\partial \bar{u}_i}{\partial x_j} \tag{B.18}$$

The velocity deformation tensor can be rearranged as

$$\frac{\partial u_i'}{\partial x_j} = s_{ij}' + \omega_{ij}' \tag{B.19}$$

where

$$\omega_{ij}' = \frac{1}{2}\left(\frac{\partial u_i'}{\partial x_j} - \frac{\partial u_j'}{\partial x_i}\right) \tag{B.20}$$

By combining previous two equations together, the second term of the rhs of equation (B.18) can be rewritten as

$$s_{ij}' \frac{\partial u_i'}{\partial x_j} = s_{ij}' s_{ij}' + s_{ij}' \omega_{ij}' = s_{ij}' s_{ij}' \tag{B.21}$$

here, we used the fact that the contraction of a symmetric tensor with an anti-symmetric is identically zero. Therefore, the final form of the turbulent kinetic energy can be written as

$$\begin{aligned}\frac{\partial k}{\partial t} + \bar{u}_j \frac{\partial k}{\partial x_j} = &- \frac{\partial}{\partial x_j}\left(\frac{1}{\rho}\overline{p' u_i'}\delta_{ij} + \frac{1}{2}\overline{u_i' u_i' u_j'} - 2\nu\overline{s_{ij}' u_i'}\right) \\ &- 2\nu\overline{s_{ij}' s_{ij}'} - \overline{u_i' u_j'}\frac{\partial \bar{u}_i}{\partial x_j}\end{aligned} \tag{B.22}$$

Appendix C

Hemodynamic indices and flow instability

We computed the time-averaged WSS (TAWSS) and the temporal WSS gradient (TWSSG) that are derived from the shear stress τ. The mathematical definitions for each indices are as follows.

$$\text{TAWSS} = \frac{1}{T}\int_0^T |\tau| \mathrm{d}t \tag{C.1}$$

$$\text{TWSSG} = \frac{1}{T}\int_0^T \left|\frac{\partial \tau}{\partial t}\right| \mathrm{d}t \tag{C.2}$$

Several hemodynamic indices have been used to investigate the cause of initiation of the aneurysms, but none of these indices have been proven to be sufficient to explain the initiation of the aneurysms. Although TAWSS is the most reported indices among the researchers, it is still unclear whether high TAWSS or low TAWSS is associated with the initiation of the aneurysms [50]. As you can see from Figure C.1, low or high TAWSS can be observed in several locations throughout the ICA. This wide-speared distribution of TAWSS can not explain why the majority of the aneurysms are located at the bifurcations. In addition, if we assume that flow instability plays an important role in the aneurysms imitation, TAWSS is not suited for measurements as it can not accommodate the temporal variation. Therefore, hemodynamic indices that can account for flow instability need to be identified.

One alternative would be TWSSG which measures the temporal changes in the direction and magnitude of WSS. Our simulations suggested the presence of high TWSSG at the apex of bifurcation. Given the fact that the high-frequency velocity fluctuations in the bifurcation were previously reported [73] and the higher presence of aneurysms at the bifurcation, the hypothesis of high TWSSG being the stimulus for aneurysm initiation seems plausible.

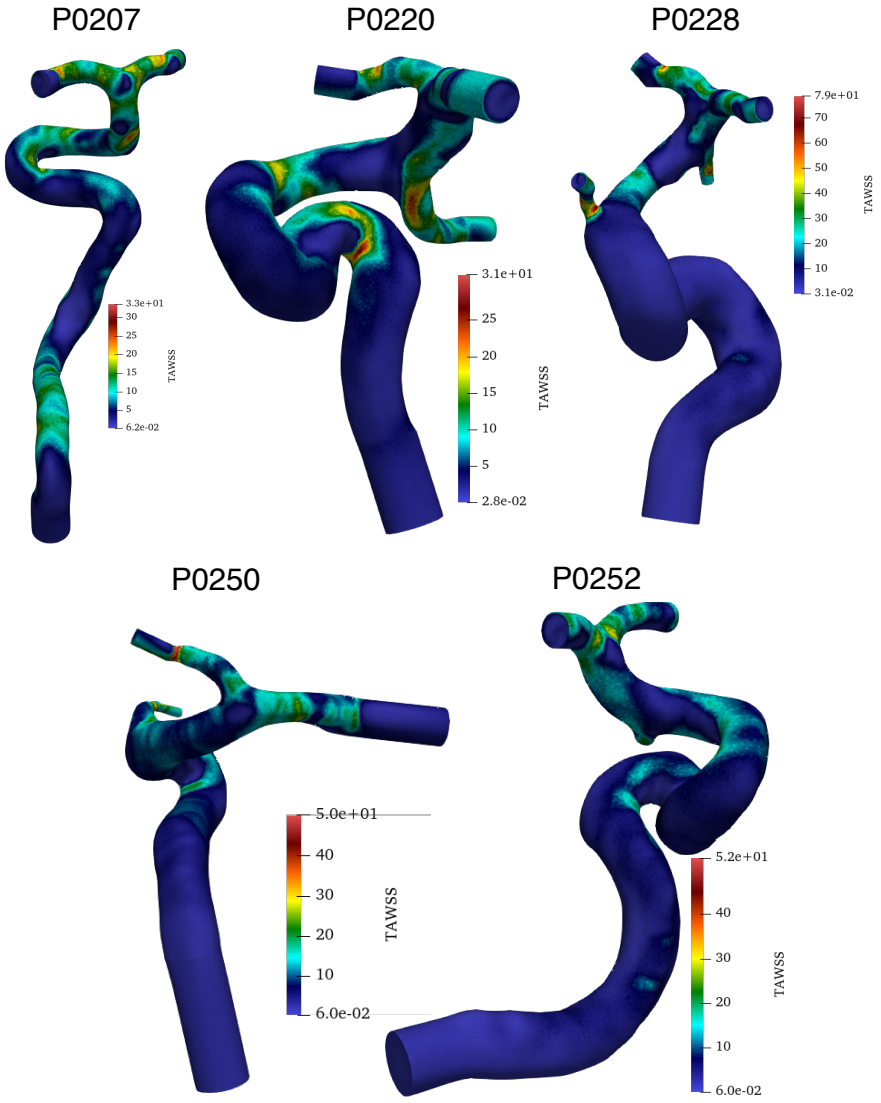

Figure C.1: Time-averaged WSS (TAWSS) having high values at several locations.

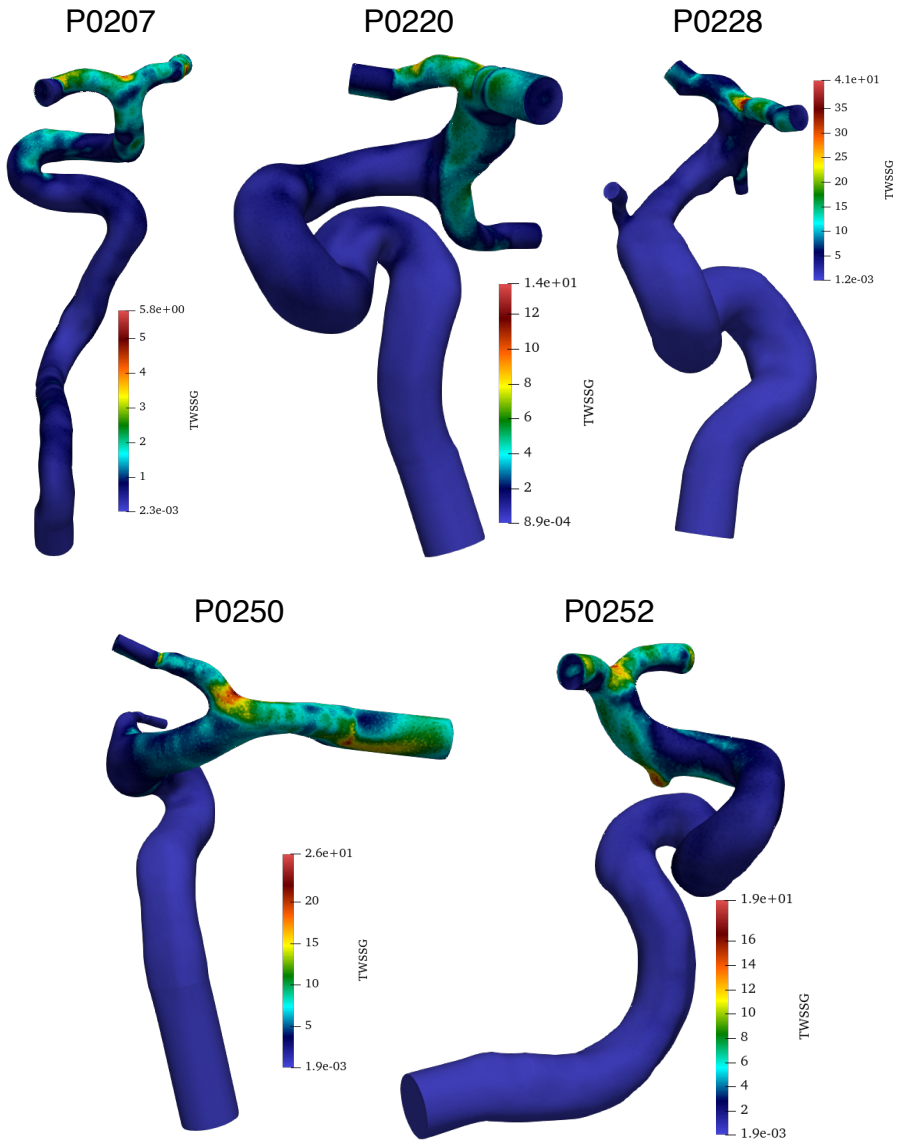

Figure C.2: Temporal WSS gradient (TWSSG) having high values exclusively near the bifurcation.

Bibliography

[1] Ahrens, J. P., Geveci, B. and Law, C. C. 'ParaView: An End-User Tool for Large-Data Visualization'. In: *The Visualization Handbook*. 2005.

[2] Ali, S. 'Pressure drop correlations for flow through regular helical coil tubes'. In: *Fluid Dynamics Research* vol. 28, no. 4 (2001), pp. 295–310.

[3] ANKETELL, J. and LEARNER, R. C. M. 'Motion of a fluid in a curved tube'. In: *Proceedings of the Royal Society of London. Series A. Mathematical and Physical Sciences* vol. 307, no. 1488 (Oct. 1968), pp. 37–53.

[4] *Ansys fluent | Fluid Simulation Software*. https://www.ansys.com/products/fluids/ansys-fluent. Accessed: 2022-04-28.

[5] Baek, S. et al. 'Theory of small on large: Potential utility in computations of fluid-solid interactions in arteries'. In: *Computer Methods in Applied Mechanics and Engineering* vol. 196, no. 31-32 (2007), pp. 3070–3078.

[6] Bertoglio, C. et al. 'Benchmark problems for numerical treatment of backflow at open boundaries'. In: *International Journal for Numerical Methods in Biomedical Engineering* vol. 34, no. 2 (2018), pp. 1–34.

[7] C. M. White. 'Streamline flow through curved pipes'. In: *Proceedings of the Royal Society of London. Series A, Containing Papers of a Mathematical and Physical Character* vol. 123, no. 792 (Apr. 1929), pp. 645–663.

[8] Cabral, B. and Leedom, L. 'Imaging vector fields using line integral convolution'. In: *Proceedings of the 20th Annual Conference on Computer Graphics and Interactive Techniques, SIGGRAPH 1993* (1993), pp. 263–270.

[9] Carlsson, C., Alenius, E. and Fuchs, L. 'Swirl switching in turbulent flow through 90° pipe bends'. In: *Physics of Fluids* vol. 27, no. 8 (2015).

[10] Chin, C. et al. 'The influence of pipe length on turbulence statistics computed from direct numerical simulation data'. In: *Physics of Fluids* vol. 22, no. 11 (2010).

[11] Cioncolini, A. and Santini, L. 'An experimental investigation regarding the laminar to turbulent flow transition in helically coiled pipes'. In: *Experimental Thermal and Fluid Science* vol. 30, no. 4 (2006), pp. 367–380.

[12] Datta, A. K. et al. 'Existence of dual solutions and three-dimensional instability in helical pipe flow'. In: *Chinese Journal of Physics* vol. 73, no. July 2020 (2021), pp. 154–166.

[13] Datta, A. K. et al. 'Numerical Study of Turbulent Helical Pipe Flow with Comparison to the Experimental Results'. In: *Journal of Fluids Engineering, Transactions of the ASME* vol. 139, no. 9 (2017).

[14] Dean, W. 'XVI. Note on the motion of fluid in a curved pipe'. In: *The London, Edinburgh, and Dublin Philosophical Magazine and Journal of Science* vol. 4, no. 20 (July 1927), pp. 208–223.

[15] Drazin, P. G. *Hydrodynamic stability*. 2nd ed. Cambridge monographs on mechanics and applied mathematics. Cambridge: Cambridge University Press, 2004.

[16] Dyke, M. van and White, F. M. *An Album of Fluid Motion*. 1982.

[17] Eggels, J. G. M. et al. 'Fully developed turbulent pipe flow: a comparison between direct numerical simulation and experiment'. In: *Journal of Fluid Mechanics* vol. 268 (June 1994), pp. 175–210.

[18] El Khoury, G. K. et al. 'Direct numerical simulation of turbulent pipe flow at moderately high reynolds numbers'. In: *Flow, Turbulence and Combustion* vol. 91, no. 3 (2013), pp. 475–495.

[19] Eustice, J. 'Experiments on stream-line motion in curved pipes'. In: *Proceedings of the Royal Society of London. Series A, Containing Papers of a Mathematical and Physical Character* vol. 85, no. 576 (1911), pp. 119–131.

[20] Eustice, J. 'Flow of water in curved pipes'. In: *Proceedings of the Royal Society of London. Series A, Containing Papers of a Mathematical and Physical Character* vol. 84, no. 568 (July 1910), pp. 107–118.

[21] Fukagata, K. and Kasagi, N. 'Highly energy-conservative finite difference method for the cylindrical coordinate system'. In: *Journal of Computational Physics* vol. 181, no. 2 (2002), pp. 478–498.

[22] Germano, M. 'On the effect of torsion on a helical pipe flow'. In: *Journal of Fluid Mechanics* vol. 125, no. 7 (1982), pp. 1–8.

[23] Geuzaine, C. and Remacle, J.-F. 'Gmsh: A 3-D Finite Element Mesh Generator with built-in Pre- and Post-Processing Facilities'. In: *International Journal for Numerical Methods in Engineering* vol. 79, no. 11 (Sept. 2009), pp. 1309–1331.

[24] Gin, R., Straatman, A. G. and Steinman, D. A. 'A dual-pressure boundary condition for use in simulations of bifurcating conduits'. In: *Journal of Biomechanical Engineering* vol. 124, no. 5 (2002), pp. 617–619.

[25] Guala, M., Hommema, S. E. and Adrian, R. J. 'Large-scale and very-large-scale motions in turbulent pipe flow'. In: *Journal of Fluid Mechanics* vol. 554 (2006), pp. 521–542.

[26] Guermond, J. L., Minev, P. and Shen, J. 'An overview of projection methods for incompressible flows'. In: *Computer Methods in Applied Mechanics and Engineering* vol. 195, no. 44-47 (2006), pp. 6011–6045.

[27] Guiza, G. et al. 'Anisotropic boundary layer mesh generation for reliable 3D unsteady RANS simulations'. In: *Finite Elements in Analysis and Design* vol. 170 (2020).

[28] Hayamizu, Y. et al. 'Experimental study of the flow in helical circular pipes: Torsion effect on the flow velocity and turbulence'. In: *Journal of Thermal Science* vol. 17, no. 3 (2008), pp. 193–198.

[29] Hof, B., Juel, A. and Mullin, T. 'Scaling of the Turbulence Transition Threshold in a Pipe'. In: *Phys. Rev. Lett.* vol. 91 (24 Dec. 2003), p. 244502.

[30] Hoi, Y. et al. 'Characterization of volumetric flow rate waveforms at the carotid bifurcations of older adults'. In: *Physiological Measurement* vol. 31, no. 3 (Mar. 2010), pp. 291–302.

[31] Hufnagel, L. et al. 'The three-dimensional structure of swirl-switching in bent pipe flow'. In: *Journal of Fluid Mechanics* vol. 835 (2018), pp. 86–101. arXiv: 1710.08357.

[32] Hüttl, T. J. and Friedrich, R. 'Influence of curvature and torsion on turbulent flow in helically coiled pipes'. In: *International Journal of Heat and Fluid Flow* vol. 21, no. 3 (2000), pp. 345–353.

[33] Itō, H. 'Friction Factors for Turbulent Flow in Curved Pipes'. In: *Journal of Basic Engineering* vol. 81, no. 2 (1959), pp. 123–132.

[34] Jeong, J. and Hussain, F. 'On the identification of a vortex'. In: *Journal of Fluid Mechanics* vol. 285, no. 3 (Feb. 1995), pp. 69–94.

[35] Kalpakli, A. et al. 'Pulsatile turbulent flow through pipe bends at high Dean and Womersley numbers'. In: *Journal of Physics: Conference Series* vol. 318, no. SECTION 9 (2011), pp. 0–10.

[36] Kamiya, A. and Togawa, T. 'Adaptive regulation of wall shear stress to flow change in the canine carotid artery'. In: *American Journal of Physiology - Heart and Circulatory Physiology* vol. 8, no. 1 (1980), pp. 14–21.

[37] Khan, M. O., Steinman, D. A. and Valen-Sendstad, K. 'Non-Newtonian versus numerical rheology: Practical impact of shear-thinning on the prediction of stable and unstable flows in intracranial aneurysms'. In: *International Journal for Numerical Methods in Biomedical Engineering* vol. 33, no. 7 (2017), pp. 1–10.

[38] Khan, M. O., Valen-Sendstad, K. and Steinman, D. A. 'Narrowing the expertise gap for predicting intracranial aneurysm hemodynamics: Impact of solver numerics versus mesh and time-step resolution'. In: *American Journal of Neuroradiology* vol. 36, no. 7 (2015), pp. 1310–1316.

[39] Khan, M. O. et al. 'On the prevalence of flow instabilities from high-fidelity computational fluid dynamics of intracranial bifurcation aneurysms'. In: *Journal of Biomechanics* vol. 127 (2021), p. 110683.

[40] Kim, J., Moin, P. and Moser, R. 'Turbulence statistics in fully developed channel flow at low reynolds number'. In: *Journal of Fluid Mechanics* vol. 177, no. 1987 (1987), pp. 133–166.

[41] Kliś, K. M. et al. 'Tortuosity of the internal carotid artery and its clinical significance in the development of aneurysms'. In: *Journal of Clinical Medicine* vol. 8, no. 2 (2019).

[42] Kováts, P. et al. 'Tomographic PIV measurements and RANS simulations of secondary flows inside a horizontally positioned helically coiled tube'. In: *Experiments in Fluids* vol. 61, no. 5 (2020), pp. 1–15.

[43] Krejza, J. et al. 'Carotid artery diameter in men and women and the relation to body and neck size'. In: *Stroke* vol. 37, no. 4 (2006), pp. 1103–1105.

[44] Kühnen, J. et al. 'Destabilizing turbulence in pipe flow'. In: *Nature Physics* vol. 14, no. 4 (2018), pp. 386–390.

[45] Lauric, A. et al. 'Curvature effect on hemodynamic conditions at the inner bend of the carotid siphon and its relation to aneurysm formation'. In: *Journal of Biomechanics* vol. 47, no. 12 (2014), pp. 3018–3027.

[46] Ligrani, P. M. 'NASA Contractor Report 4607 Army Research Laboratory A Study of Dean Vortex Development and Structure in a Curved Rectangular Channel With Aspect Ratio of 40 at Dean Numbers up to 430 Space Administration'. In: no. C (1994).

[47] Liu, S. and Masliyah, J. H. 'Axially invariant laminar flow in helical pipes with a finite pitch'. In: *Journal of Fluid Mechanics* vol. 251, no. sl (1993), pp. 315–353.

[48] Logg, A., Mardal, K.-A. and Wells, G., eds. *Automated Solution of Differential Equations by the Finite Element Method*. Vol. 84. Lecture Notes in Computational Science and Engineering. Berlin, Heidelberg: Springer Berlin Heidelberg, 2012.

[49] Luca Antiga, O. S. *Aneuriskwebthe Aneurisk Dataset Repository*. http://ecm2.mathcs.emory.edu/aneuriskweb/index. Accessed: 2022-04-07.

[50] Meng, H. et al. 'High WSS or Low WSS? Complex interactions of hemodynamics with intracranial aneurysm initiation, growth, and rupture: Toward a unifying hypothesis'. In: *American Journal of Neuroradiology* vol. 35, no. 7 (2014), pp. 1254–1262.

[51] Meng, H. et al. 'Complex hemodynamics at the apex of an arterial bifurcation induces vascular remodeling resembling cerebral aneurysm initiation'. In: *Stroke* vol. 38, no. 6 (2007), pp. 1924–1931.

[52] Mortensen, M. and Valen-Sendstad, K. 'Oasis: A high-level/high-performance open source Navier-Stokes solver'. In: *Computer Physics Communications* vol. 188 (2015), pp. 177–188. eprint: 1602.03643.

[53] Moser, R. D., Kim, J. and Mansour, N. N. 'Direct numerical simulation of turbulent channel flow up to Reτ=590'. In: *Physics of Fluids* vol. 11, no. 4 (Apr. 1999), pp. 943–945.

[54] Natarajan, T. et al. 'On the spectrographic representation of cardiovascular flow instabilities'. In: *Journal of Biomechanics* vol. 110 (2020), p. 109977.

[55] Noorani, A., El Khoury, G. K. and Schlatter, P. 'Evolution of turbulence characteristics from straight to curved pipes'. In: *International Journal of Heat and Fluid Flow* vol. 41 (2013), pp. 16–26.

[56] Ojha, M. 'Wall shear stress temporal gradient and anastomotic intimal hyperplasia'. In: *Circulation Research* vol. 74, no. 6 (1994), pp. 1227–1231.

[57] Orszag, S. A. 'Analytical theories of turbulence'. In: *Journal of Fluid Mechanics* vol. 41, no. 2 (1970), pp. 363–386.

[58] Piccinelli, M. et al. 'A framework for geometric analysis of vascular structures: Application to cerebral aneurysms'. In: *IEEE Transactions on Medical Imaging* vol. 28, no. 8 (2009), pp. 1141–1155.

[59] Reynolds, O. 'IV. On the dynamical theory of incompressible viscous fluids and the determination of the criterion'. In: *Philosophical Transactions of the Royal Society of London. (A.)* vol. 186 (Dec. 1895), pp. 123–164.

[60] Roache, P. J. 'Code verification by the method of manufactured solutions'. In: *Journal of Fluids Engineering, Transactions of the ASME* vol. 124, no. 1 (2002), pp. 4–10.

[61] Sanders-Taylor, C. et al. 'The carotid siphon: A historic radiographic sign, not an anatomic classification'. In: *World Neurosurgery* vol. 82, no. 3 (2014), pp. 423–427.

[62] Sforza, D. M., Putman, C. M. and Cebral, J. R. 'Hemodynamics of cerebral aneurysms'. In: *Annual Review of Fluid Mechanics* vol. 41 (2009), pp. 91–107.

[63] Shojima, M. 'Magnitude and Role of Wall Shear Stress on Cerebral Aneurysm. Computational Fluid Dynamic Study of 20 Middle Cerebral Artery Aneurysms'. In: *Stroke* (2004).

[64] Si, H. 'TetGen, a Delaunay-Based Quality Tetrahedral Mesh Generator'. In: *ACM Trans. Math. Softw.* vol. 41, no. 2 (Feb. 2015).

[65] Simo, J. C. and Armero, F. 'Unconditional stability and long-term behavior of transient algorithms for the incompressible Navier-Stokes and Euler equations'. In: *Computer Methods in Applied Mechanics and Engineering* vol. 111, no. 1-2 (1994), pp. 111–154.

[66] SMAGORINSKY, J. 'GENERAL CIRCULATION EXPERIMENTS WITH THE PRIMITIVE EQUATIONS'. In: *Monthly Weather Review* vol. 91, no. 3 (Mar. 1963), pp. 99–164.

[67] Sreenivasan, K. R. and Strykowski, P. J. 'Stabilization effects in flow through helically coiled pipes'. In: *Experiments in Fluids* vol. 1, no. 1 (1983), pp. 31–36.

[68] Steinman, D. A. et al. 'Image-based computational simulation of flow dynamics in a giant intracranial aneurysm'. In: *American Journal of Neuroradiology* vol. 24, no. 4 (2003), pp. 559–566.

[69] SUGIYAMA, S., HAYASHI, T. and YAMAZAKI, K. 'Flow Characteristics in the Curved Rectangular Channels : Flow Visualization of Seondary Flow'. In: *TRANSACTIONS OF THE JAPAN SOCIETY OF MECHANICAL ENGINEERS Series B* vol. 48, no. 434 (1982), pp. 1870–1876.

[70] Takeuchi, S. and Karino, T. 'Flow patterns and distributions of fluid velocity and wall shear stress in the human internal carotid and middle cerebral arteries'. In: *World Neurosurgery* vol. 73, no. 3 (2010), pp. 174–185.

[71] Torii, R. et al. 'Fluid-structure interaction modeling of a patient-specific cerebral aneurysm: Influence of structural modeling'. In: *Computational Mechanics* vol. 43, no. 1 (2008), pp. 151–159.

[72] Valen-Sendstad, K. and Steinman, D. A. 'Mind the gap: Impact of computational fluid dynamics solution strategy on prediction of intracranial aneurysm hemodynamics and rupture status indicators'. In: *American Journal of Neuroradiology* vol. 35, no. 3 (2014), pp. 536–543.

[73] Valen-Sendstad, K., Mardal, K. A. and Steinman, D. A. 'High-resolution CFD detects high-frequency velocity fluctuations in bifurcation, but not sidewall, aneurysms'. In: *Journal of Biomechanics* vol. 46, no. 2 (2013), pp. 402–407.

[74] Valen-Sendstad, K., Piccinelli, M. and Steinman, D. A. 'High-resolution computational fluid dynamics detects flow instabilities in the carotid siphon: Implications for aneurysm initiation and rupture?' In: *Journal of Biomechanics* vol. 47, no. 12 (2014), pp. 3210–3216.

[75] Valen-Sendstad, K. et al. 'Estimation of Inlet Flow Rates for Image-Based Aneurysm CFD Models: Where and How to Begin?' In: *Annals of Biomedical Engineering* vol. 43, no. 6 (2015), pp. 1422–1431.

[76] Vlak, M. H. et al. 'Prevalence of unruptured intracranial aneurysms, with emphasis on sex, age, comorbidity, country, and time period: A systematic review and meta-analysis'. In: *The Lancet Neurology* vol. 10, no. 7 (2011), pp. 626–636.

[77] Wan, H. et al. 'Sidewall aneurysm geometry as a predictor of rupture risk due to associated abnormal hemodynamics'. In: *Frontiers in Neurology* vol. 10, no. JUL (2019), pp. 1–7.

[78] Wang, Z. et al. 'Direct numerical simulation of a turbulent 90° bend pipe flow'. In: *International Journal of Heat and Fluid Flow* vol. 73, no. July (2018), pp. 199–208.

[79] White, F. M. *Viscous fluid flow*. McGraw-Hill Higher Education, 2006.

[80] Wiebers, D. O. 'Unruptured intracranial aneurysms: natural history, clinical outcome, and risks of surgical and endovascular treatment'. In: *The Lancet* vol. 362, no. 9378 (July 2003), pp. 103–110.

[81] Womersley, J. R. 'Method for the calculation of velocity, rate of flow and viscous drag in arteries when the pressure gradient is known'. In: *The Journal of Physiology* vol. 127, no. 3 (Mar. 1955), pp. 553–563.

[82] Wu, X. and Moin, P. *A direct numerical simulation study on the mean velocity characteristics in turbulent pipe flow*. Vol. 608. 2008, pp. 81–112.

[83] Xiang, J. et al. 'Hemodynamic-morphologic discriminants for intracranial aneurysm rupture'. In: *Stroke* vol. 42, no. 1 (2011), pp. 144–152.

[84] Xie, D. G. 'Torsion effect on secondary flow in a helical pipe'. In: *International Journal of Heat and Fluid Flow* vol. 11, no. 2 (1990), pp. 114–119.

[85] Yamamoto, K., Yanase, S. and Jiang, R. 'Stability of the flow in a helical tube'. In: *Fluid Dynamics Research* vol. 22, no. 3 (1998), pp. 153–170.

[86] Yamamoto, K., Yanase, S. and Yoshida, T. 'Torsion effect on the flow in a helical pipe'. In: *Fluid Dynamics Research* vol. 14, no. 5 (1994), pp. 259–273.